UR-1162
ER-13065-622

Experimental Studies of Electron-Positron Annihilation into Four-Lepton Final States at Center-of-Mass Energies from 50 to 61.4 GeV **

by

Yiu-Hung M. Ho

THE UNIVERSITY OF ROCHESTER

DEPARTMENT OF PHYSICS AND ASTRONOMY

ROCHESTER , NEW YORK

5/7/90

Abstract

We report results of a study of $e^+e^- \to e^+e^-e^+e^-$ and $e^+e^-\mu^+\mu^-$ events observed in the Amy Detector at the Tristan e^+e^- collider, at center-of-mass energies from 50 to 61.4 GeV. We study events where three or four of the final-state leptons are produced at wide angles and observed in the detector. We compare our measured event yield with expectations based on order α^4 QED calculations. In the sample of events with three observed tracks, we find good agreement with theory, but in the 4-track sample we observe a significant excess in events for the $e^+e^- \to e^+e^-\mu^+\mu^-$ reaction with with dimuon masses less than 1.0 GeV. These events also have a strong asymmetry in the polar angular distribution of $\mu^+\mu^-$ pairs.

Experimental Studies of Electron-Positron Annihilation into Four-Lepton Final States at Center-of-Mass Energies from 50 to 61.4 GeV **

by

Yiu-Hung M. Ho

Submitted in Partial Fulfillment
of the
Requirements for the Degree

DOCTOR OF PHILOSOPHY

Supervised by Professor S.L. Olsen

University of Rochester
Rochester, New York

April 30, 1990

** Research supported by U.S. Dept. of Energy contract DE-AC02-76ER13065.

VITA

The author was born on May 10, 1960, in Canton, China, but was carried to Hong Kong while still in infancy. He immigrated U.S.A. in January 1979 and spent his freshmen and sophomore year at Central State University. He transferred to University of Oklahoma in 1981, where he majored in Physics and minored in Geophysics. While attending college, he worked as research assistant for Prof. George Kalbfleish, OU High Energy Physics group. He also worked with Prof. Pat Skubic for the developmental research on streamer tube, and subsequently involved in the vertex detector project (nickname bread box) for the experiment E653 at Fermilab. After received his B.S. degree in the May of 1983, he continued to work for the same experiment and stayed in Fermilab until August, 1984. He then began graduate study in the Department of Physics and Astronomy of the University of Rochester, where he worked on the AMY experiment at the TRISTAN accelerator at KEK. His thesis adviser has been Prof. Stephen L. Olsen.

Acknowledgements

My thesis could not have been finished without the help of the CDC gang, all the AMY members, and the dedicated staff at KEK, especially Y. Kurihara, T. Omori, and John Smith who have given me tremendous help in starting the QED calculations and double-checked my analysis from time to time. I also wish to express my deepest thank to Patrice Perez who gives me numerous friendly advice and help; to Carl Rosenfeld, under whom I acquire a lot of knowledge not readily provided in the textbooks, and whose dedication and thoroughness are inspiring in my training as serious scientific investigator; and to Prof. S.L. OLsen, who gives me encouragement and constructive criticism. I particularly admire Prof. Olsen's uncommon physics insight which is the guiding force behind this work.

Lastly, I would like to thank my mother Yeung-Dip Au, a gentle woman of high virtue who endured serious hardship to raise me and support our family; my sister Hoi-Yee Nancy James who sacrificed herself to provide material comfort to our family; and her husband Jerry James for his endless help. Both Yeung-Dip and Hoi-Yee are ordinary women but acting extraordinarily under adverse conditions in the tragic chapter of Chinese history.

Contents

List of Tables

List of Figures

Chapter 1

Introduction

1.1 Development of Electromagnetic Theory

Until the end of the last century, all observed electromagnetic phenomena could be successfully described by Maxwell's unified theory of electricity and magnetism. In Maxwell's model, charged particles are sources of continuous fields that move with them and the forces between charged particles arise from the interactions of these fields with the charges of other particles. Disturbances in these fields result in electromagnetic waves that propagate at the speed of light, the value of which was a prediction of the theory. While this picture seemed to explain all the known phenomena at that time, it also gave rise to other questions relating to the nature of the fields. Do they have a physical reality or are they just a convenient working concept? What is the medium through which the electromagnetic wave propagates?

A feature of Maxwell's theory is the prediction of the existence of electromagnetic waves that propagate through free space. In 1887, Hertz showed that a spark between two gaps at the ends of an induction coil caused a spark between a similar gap placed at a distance. This was well explained as being caused by the electromagnetic waves of Maxwell's theory propagating from one gap, initiating the spark at the other. But this still left the question about the nature of ether, the medium for the electromagnetic wave propagation, unanswered. Such a medium will cause the light going perpendicular and parallel to the direction of the earth's motion through the ether to be different, something that can be measured by interference technique. The negative observation of such a difference in the Michelson-Morley experiment in the same year contradicted the existence of such a medium.

The energy density distribution for blackbody radiation presented another problem for the classical electrodynamic theory. While experimental observations show that the energy density decreases rapidly at small wavelengths, the continuous electromagnetic waves theory suggests that it should increase indefinitely. In 1900, Planck found that by introducing the concept of quanta he was able to find good agreement between theoretical calculations and the experimental data. This implied that radiation was not emitted and absorbed by atoms continuously, but only in discrete amounts, the size of which is proportional to the wave's frequency. Einstein expanded the idea even further, proposing that electromagnetic radiation was composed of particles called photons. The photoelectric effect, in which the maximum energy of the electron emitted from the surface of metal is determined by the frequency of the incident light but not by its intensity, can be well explained by this concept. This theory finally become widely accepted in 1923, when Compton showed that the frequency shift of photon scattered from electrons can be interpreted by the mechanical scattering of two particles, which required that the photon behave like a particle.

In 1927, Dirac established the foundation for the modern quantum field theory with his famous paper *The Quantum Theory of the Emission and Absorption of Radiation* [1]. According to Dirac's theory, classical particles and fields are closely interrelated. A particle could be regarded as the quanta of a field. Quantum Electro-Dynamics (QED) is the best example of such a concept. The quanta of the electromagnetic field is the photon and the interactions between charged particles is mediated by the exchange of photons. On the other hand, electrons and positrons can be thought of as the quanta of an electron-positron field. The number of such particles can decrease due to the annihilation of electron-positron pairs into photons and increase via photons converting into electron-positron pairs. An important characteristic of QED is that the interactions are between charged particles only, photons do not interact among themselves. This, plus the smallness of the 'interaction strength', allows the use of perturbation methods for calculations.

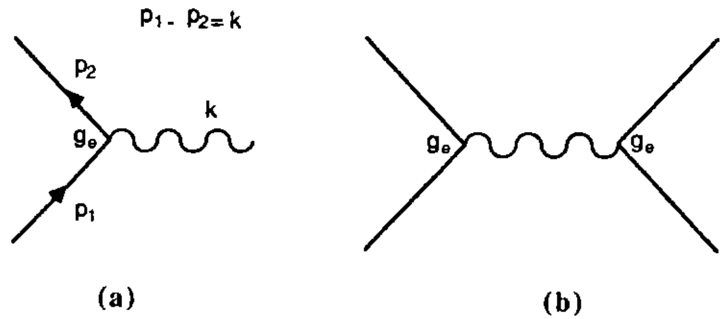

Figure 1.1: Feynman diagram representations for the QED interactions between charged particles and photons.

These calculations were hopelessly complicated until Feynman devised a simple set of rules and showed how to represent the complicated interactions by 'pictures' now called Feynman Diagrams.

Figure 1.1 illustrates the interactions between charged particles and photon represented by Feynman Diagrams. The lines represent the interacting particles in momentum space, and the vertices where the lines meet represent the interaction of the particles. Each vertex thus associates with the 'interaction strength' of QED, which is formally called the coupling constant (g_e). It is usually expressed in terms of dimensionless constant α, the fine structure constant, as $g_e = \sqrt{4\pi\alpha}$ ($\alpha \equiv e^2/\hbar c \simeq 1/137$). Following a simple set of rules, the 'picture' can be converted into an equation representing the amplitude of the whole process. Upon squaring the amplitude, the differential cross section, the measurable quantity by experiment, is obtained. Therefore in the cross section relation for QED processes, the fine structure constant appears in power form, where the power reflects the number of photons and e^+e^- pair involved in the process. For example, the 'single photon annihilation' interactions $e^+e^- \to e^+e^-, e^+e^- \to \mu^+\mu^-, e^+e^- \to \tau^+\tau^-$ or $e^+e^- \to q\bar{q}$ as represented by Fig. 1.1b are α^2 processes; whereas the two-photon interactions, which is the subject of this thesis and are represented by the diagrams

Experiment	Λ_+(GeV)	Λ_-(GeV)
AMY	130	330
CELLO	74	150
JADE	178	200
Mark J	165	235
PLUTO	184	162
TASSO	435	590
HRS	154	220

Table 1.1: Comparison of QED cut off parameter for $e^+e^- \rightarrow e^+e^-$ process.

in Fig. 1.2, are α^4 processes. This, in effect, scales their importance relative to the total reaction cross section of the e^+e^- interaction. In fact, a standard way of testing QED is to measure the cross sections of these α^2 processes in e^+e^- collider. One can fit the observed results with a QED cross section modified with form factor :

$$F(q^2) = 1 - \frac{q^2}{q^2 - (\Lambda_{\pm}^{QED})^2} \tag{1.1}$$

where q^2 is square of the four-momentum transfer to be detailed later, and $\Lambda_{\pm}$ are the cut off parameters which will be infinitely large if QED is correct. Table 1.1 [3] shows the lower bounds of $\Lambda_{\pm}$ for the $e^+e^- \rightarrow e^+e^-$ process from various experimental groups at SLAC, Petra and Tristan. These large limits of Λ indicate that QED remains valid down to distances of order 10^{-16} cm.

1.2 The QED Production of Four-lepton Final States

Another test of QED can be done through the study of the process at higher order of α. The QED interactions producing four-lepton final states is a common choice. These interactions involve the exchanges of two photons, thus making them α^4 processes, and the reactions $e^+e^- \rightarrow e^+e^-e^+e^-$ and $e^+e^- \rightarrow e^+e^-\mu^+\mu^-$ are typical examples. The α^4 processes are substantially more complicated than the α^2 processes. For $e^+(p_+)e^-(p_-) \rightarrow l^+(q_+)l^-(q_-)L^+(k_+)L^-(k_-)$, where l, L may be e or μ, the differential cross section at center-of-mass energy $\sqrt{s}$ can be

written as:

$$d\sigma = \frac{\alpha^4}{32\pi^4 s}|\sum_i M_i|^2\delta^4(p_+ + p_- - q_+ - q_- - k_+ - k_-)\frac{d^3\mathbf{q}_+ d^3\mathbf{q}_- d^3\mathbf{k}_+ d^3\mathbf{k}_-}{q_+^0 q_-^0 k_+^0 k_-^0}. \tag{1.2}$$

The p's, q's, k's represent the 4-momenta of the particles, and the quantities M_i is the amplitude of the contributing processes represented by Feynman diagrams. In Feynman diagrams, the l's and L's can be interchanged as long as the conservation rules (lepton number, charge, etc) are obeyed. Each distinct change leads to a new Feynman diagram. This results in 36 Feynman diagrams for the $e^+e^- \rightarrow e^+e^-e^+e^-$ process, and 12 for the $e^+e^- \rightarrow e^+e^-\mu^+\mu^-$ process. These diagrams are usually classified into 4 groups, multiperipheral (Fig. 1.2a), bremsstrahlung (Fig. 1.2b), annihilation (Fig. 1.2c) and conversion (Fig. 1.2d).

In general, the multiperipheral group provides the dominant contribution to the four-lepton total cross section. It is conventionally referred to as the two-photon diagram and plays an essential role in the study of two-photon physics. A unique feature of these diagrams is the existence of a pair of leptons that are coupled to two photons; the types of physics involved are intimately linked to the characteristics of the photons in this system. Referring to Fig. 1.2(a) where l is the electron, the photons 4-momenta are equal to the momentum transfer of the incoming and outgoing electron: $q_{1,2} = p_{\pm} - q_{\pm}$. One defines the quantity $Q_i^2 = -q_i^2$ as the negative mass square of the photon. Neglecting the electron mass,

$$Q_i^2 = 4p_{\pm}^0 q_{\pm}^0 sin^2(\frac{\theta_{\pm}}{2}),$$

where $\theta_{\pm}$ is angle between $p_{\pm}$ and $q_{\pm}$. The mass of a real photon is zero, therefore, for Q_i^2 different from zero, the photon is virtual and is regarded as "off-the-mass-shell". For a space-like photon, as the one under discussion, Q_i^2 is positive; it is negative for a time-like photon (e.g. the photon at the vertex of e^+e^- annihilation). Other important kinematic variables in the two-photon system are the two-photon invariant mass squared $W^2 = (q_1 + q_2)^2$, and the polarizations of the photons. The cross section for $e^+e^- \rightarrow e^+e^-X$ (X= anything) can then be written as the combinations of the photon flux factors (L) and photon cross section in the

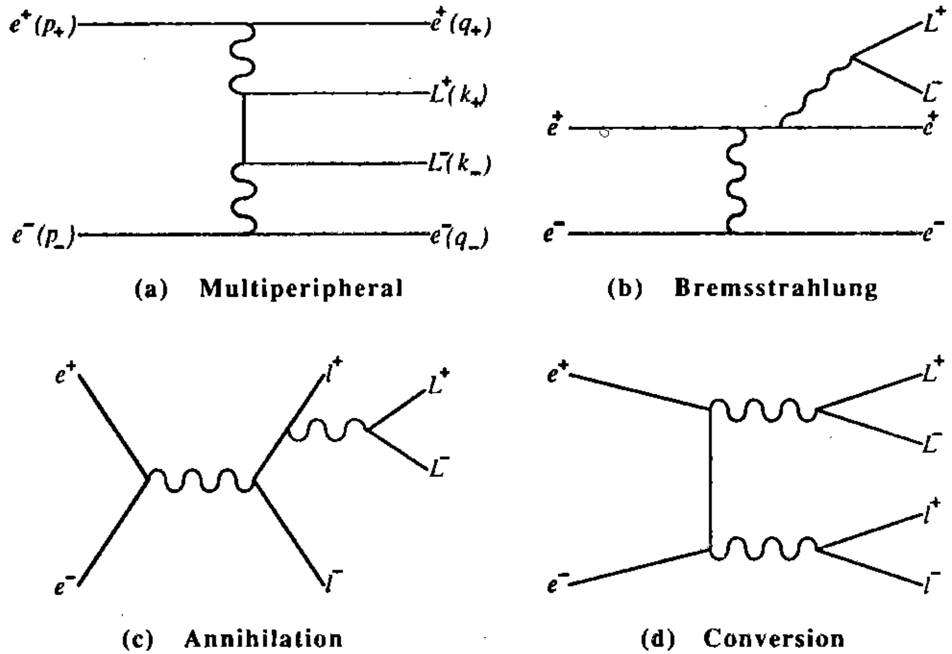

Figure 1.2: Feynman diagrams for the α^4 processes. Permutation of the lepton lines gives rise to 36 diagrams for $e^+e^-e^+e^-$ and 12 diagrams for $e^+e^-\mu^+\mu^-$.

transverse(t) and longitudinal(l) polarization [5]:

$$\sigma_{e^+e^-\to e^+e^-X} = L_{tt}\sigma_{tt} + L_{tl}\sigma_{tl} + L_{lt}\sigma_{lt} + L_{ll}\sigma_{ll} + \text{ interference terms between } l \text{ and } t. \quad (1.3)$$

1.2.1 Low Q^2 processes

In real experimental situations, both of the final e^+e^- are usually unobserved in the detector because they emerge at a small angle relative to the beam axis where the detector coverage is incomplete. In this case both photons are near the mass shell, i.e. q_1^2, $q_2^2 \to 0$, and only the transverse polarization term remains in equation 1.3. It can then be simplified using the equivalent-photon-approximation (EPA) [6]:

$$\sigma_{e^+e^-\to e^+e^-X} = \int L_{\gamma\gamma}(\omega)\sigma_{\gamma\gamma\to X}(\omega)d\omega, \quad (1.4)$$

where $\omega = W^2/s$ is the scaled center-of-mass energy squared. The factor $L_{\gamma\gamma}$ is the luminosity function and is expressed as [7] :

$$L_{\gamma\gamma} = (\frac{\alpha}{2\pi} ln\frac{s}{4m_e^2})^2 f(\omega) \quad (1.5)$$

$$\begin{aligned} f(\omega) &= \frac{1}{\omega}[(2+\omega)^2 ln\frac{1}{\omega} - 2(1-\omega)(3+\omega)] \\ &\simeq \frac{4}{\omega} ln\frac{1}{\omega}, \end{aligned} \quad (1.6)$$

as $\omega \to 0$. To complete the calculation, all one needs to know is the cross section for $\gamma\gamma \to X$ Using the approximation that $\sigma_{\gamma\gamma\to\mu^+\mu^-} = 4\pi\alpha^2/W^2$, the cross section for $e^+e^- \to e^+e^-\mu^+\mu^-$ is simply

$$\sigma_{e^+e^-\to e^+e^-\mu^+\mu^-} = \frac{\alpha^4}{\pi} ln(\frac{s}{4m_e^2}) ln(\frac{s}{4m_\mu^2}) \frac{1}{m_\mu^2}. \quad (1.7)$$

For resonance production of a particle of mass M_R and spin $J \neq 1$, one may use

$$\sigma_{\gamma\gamma\to R} = 8\pi^2(2J+1)\frac{\Gamma_{\gamma\gamma}}{M_R}\delta(W^2 - M_R^2), \quad (1.8)$$

and the two-photon cross section becomes

$$\sigma_{e^+e^-\to e^+e^-R} = 2\alpha^2 ln^2(\frac{s}{4m_e^2})(2J+1)\frac{\Gamma_{\gamma\gamma}}{sM_R} f(\frac{M_R^2}{s}). \quad (1.9)$$

	Multiperipheral	Bremsstrahlung	Annihilation	Conversion
2 tracks	$\sim$ 100%	$\sim$ 0%	$\sim$ 0%	$\sim$ 0%
3 tracks	$\sim$ 83%	$\sim$ 17%	$\sim$ 0%	$\sim$ 0%
4 tracks	$\sim$ 10%	$\sim$ 80%	$\sim$ 4%	$\sim$ 6%

Table 1.2: Relative contribution to the cross sections for the four-lepton processes under different experimental tagging condition(by requiring number of visible tracks above 20°). The interference among the different Feynman groups is not included.

The two-photon system creates a state with charge conjugation $C = +1$, a quantum number which is conserved in electromagnetic and strong interaction. Because the photons are almost real, by Yang's theorem [8] the resonance can only have spin 0 or 2. Such rules thus limit the production of the resonances to $J = 0$ or 2, $C = +1$ states; and the untagged two-photon processes has been used to study the properties of the 0^+ or 2^+ particles such as π^0, η, η', f(1270), η_c(2980), etc.

1.2.2 Three-track and Four-track Events

The situation becomes quite different when one or both of the outgoing e^+e^- are observed at large opening angle with respect to the beam axis [4]. In these cases, the observed electron (positron) from the incident electron (positron) line is called the tagged electron (positron), and the events are commonly referred to as 'single-tag' or 'double-tag' events depending on whether one or both of the beam particles are observed. As one or both of the values are significantly different from zero, the EPA formulation is no longer sufficiently accurate for cross section calculations. Moreover, the contributions from other Feynman-graph groups become significant. One has to resort to the full calculation using Monte Carlo methods, which will be described in detail in Chapter four. Table 1.2 show the relative contributions from the different Feynman-graph groups when one requires different numbers of tracks $> 20°$ from the beam axis. The results are based on the calculations used in this thesis and interference among the different Feynman-graph groups are not included.

While there is a relatively large cross section for the detection of untagged

events, which can provide for high-statistics measurements of order α^4 QED processes, they tend to populate an uninteresting region of phase space. On the other hand, with one or both scattered electrons at large opening angles, the three-track and four-track events produce highly virtual photons, which can provide sensitive tests of QED at very small distance in a relatively background free environment. This is especially true for the four-track events in which all final state particles are identified. Furthermore, Yang's theorem is not applicable to the highly virtual photons in the two-photon system. The creation of spin-1 even-C resonance state become possible. Therefore, these high Q^2 events may reveal interesting physics inaccessible in ordinary e^+e^- annihilation processes.

In the AMY experiment, a number of $e^+e^-e^+e^-$ and $e^+e^-\mu^+\mu^-$ events are observed to have with three or four final state particles visible at wide angles relative to the beam direction. In this thesis we describe a detailed study of such events and compare their rate and properties with the predictions of QED. The remainder of this thesis is organized as follows. Chapter two provides a general description of the equipment used for these measurements, namely the TRISTAN e^+e^- storage ring and the AMY detector. Chapter three describes the event selection and data analysis. Chapter four is devoted to the discussion of the results of QED calculations using computer programs provided by different authors. We compare the measurements with the theoretical predictions in Chapter five.

Chapter 2

The AMY Detector

2.1 The TRISTAN e^+e^- Collider

AMY is one of the three major experiments using the TRISTAN e^+e^- collider at KEK (Kou Energii Butsuri-gaku Kenkyuu-jyo, or National Laboratory for High Energy Physics) in Tsukuba City, Japan. TRISTAN (Transposable Ring Intersecting STorage Accelerator in Nippon) is made up of a 400 meter long linac, an accumulator ring (AR) 377 meters in circumference, and the 3 km circumference Main Ring (MR) (See Fig. 2.1.).

Positrons, generated by bombarding 200 MeV electrons onto a Tantalum target, are transferred into the linac, where they are accelerated to 2.5 GeV and injected into the AR. After the accumulation of a sufficient number of particles, (beam currents of ~20 mA) the AR accelerates the positron beam up to 8.0 GeV and injects them into the MR. This process is repeated four times, producing two diametrically opposed bunches each containing $\sim 2 \times 10^{11}$ positrons a few centimeters in length and circulating counter-clockwise in the MR. Subsequently, two similar bunches of clockwise circulating electrons are introduced in the MR using the same linac and AR. The beams are then accelerated to high energy and brought into collision. The electron and positron bunches are arranged to collide at four intersecting points, each of which are surrounded by detector systems for studying the products of the collisions. With a total RF power of 25 MW, the MR can accelerate and store beams up to energies of $\sim$ 32 GeV, providing e^+e^- collisions with a center-of-mass energy of 64 GeV.

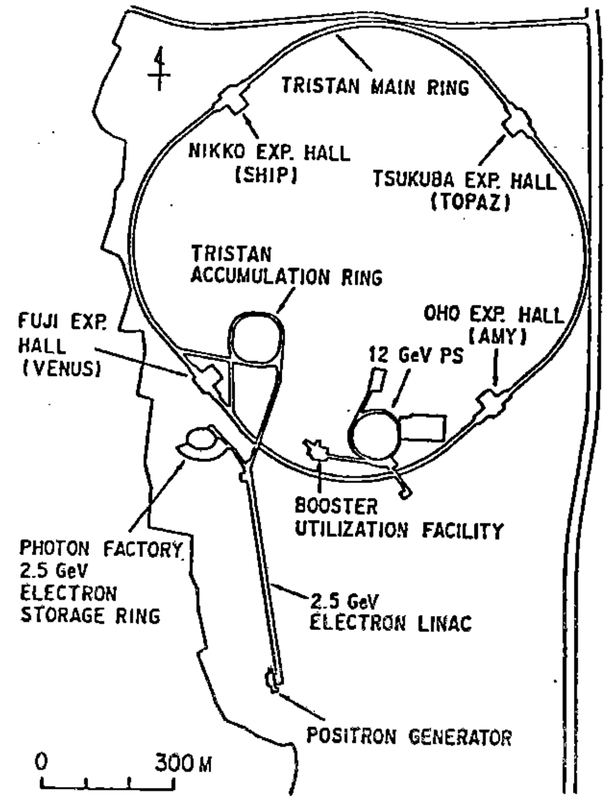

Figure 2.1: An overview of the TRISTAN accelerator complex. The AMY detector is located at the OHO experimental hall.

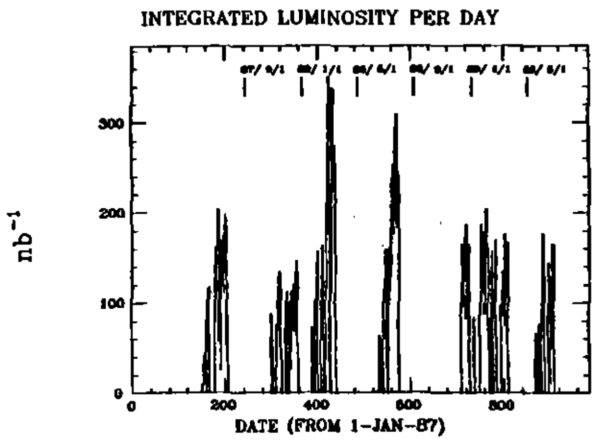

Figure 2.2: Average daily Integrated luminosities from January 1987 to summer of 1989.

Tristan first produced electron-positron collisions in the November 1986, with a center-of mass energy of 50 GeV. It has been operating successfully since that time, with the center-of mass energy increasing to as high as 61.4 GeV. The design luminosity of TRISTAN, $\sim 1 \times 10^{31}$ cm^{-2}sec^{-1}, has been achieved and the daily integrated luminosity has been improving continuously to the point where it has exceeded 300 nb^{-1}/collision point/day (Fig. 2.2).

2.2 The AMY Detector

The AMY detector (Fig. 2.3) [11], is a general-purpose detector with special emphasis on lepton identification. Cylindrical tracking chambers and an electromagnetic calorimeter are inside a superconducting solenoidal coil which generates a 3 tesla magnetic field. This high magnetic field provides for good charged particle momentum resolution in a rather compact system. There are also calorimeters at each end of the solenoid for providing electromagnetic energy measurements, resulting in a total detection coverage of 96% of the solid angle. These are all contained within the iron magnetic flux return yoke, which also serves as a hadron absorber. Outside of the iron yoke are large area drift chambers and scintillation counters that identify tracks that penetrate the iron, a signature for muons. These devices are also used to eliminate cosmic rays. The characteristics of each of the

major components of the detector are described in some detail in the following sections.

The AMY detector is coaxial with the e^+e^- beam line and is centered at the e^+e^- collision point. The electron beam direction is taken as the direction of positive z, and the y-axis points vertically upward and the x-axis points radially outward from the center of the Tristan ring. Other spatial coordinates such as ϕ, θ, etc., follow the standard (right-handed) conventions.

2.2.1 The Inner Tracking Chamber(ITC)

The innermost component of the AMY detector is the Inner Tracking Chamber, ITC. It is located radially outside of the beam pipe, is 55 cm in length, and extends in radius from 12.2 cm to 14.2 cm. The 1.5 mm thick Aluminium beam pipe corresponds to 1.7% radiation length. The small size and proximity to the interaction point enables the ITC to give a precise measurement of the vertex position of the charged tracks in an event. It is also used to provide a fast trigger.

The ITC (Fig. 2.4) consists of four staggered layers of aluminized plastic drift tubes, each approximately 6 mm in diameter. Inside each tube there is a 16 μm diameter anode wire stretched along the axis. The gas mixture (50% Ar, 50% C_2H_6) is pressurized to 1.48 kg/cm^2 and the operating voltage is 1.7 kV. The spatial resolution is $\sigma \sim 80$ μm. Signals from the anode wires are processed by a series of amplifiers and discriminators. The arrival time of the signal relative to the beam crossing is measured in a Time to Analog Converter (TAC) and Analog to Digital Converter (ADC) system. The charged track's position is inferred from the time it takes the ionization electrons to drift to the anode wire. In order to optimize the spatial resolution, the threshold for the discriminator used to trigger the TAC-ADC system is set very low. A separate ADC system is used to measure the pulse height of the anode signal for use in the rejection of noise pulses.

2.2.2 The Central Drift Chamber(CDC)

Immediately outside of the ITC is the central drift chamber CDC (Fig. 2.5). It has six disks varying in length from 93 cm at the innermost disk to 180 cm for

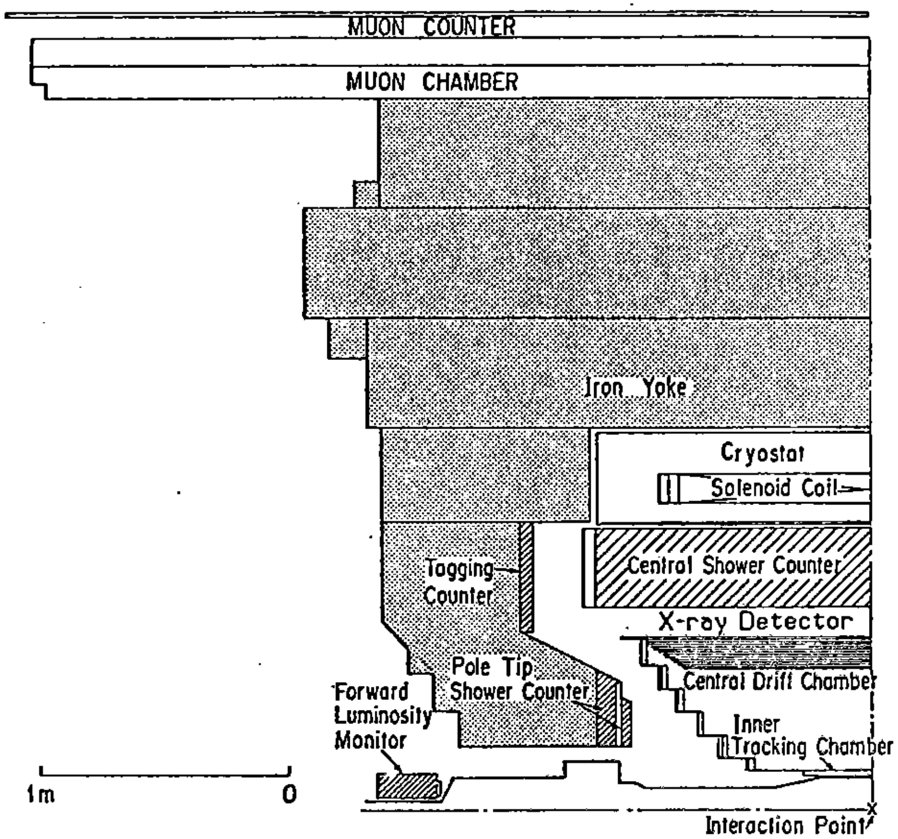

Figure 2.3: An overview of the AMY detector. For the 50 and 52 GeV runs, trigger scintillation counters were located where the X-ray detector is currently situated.

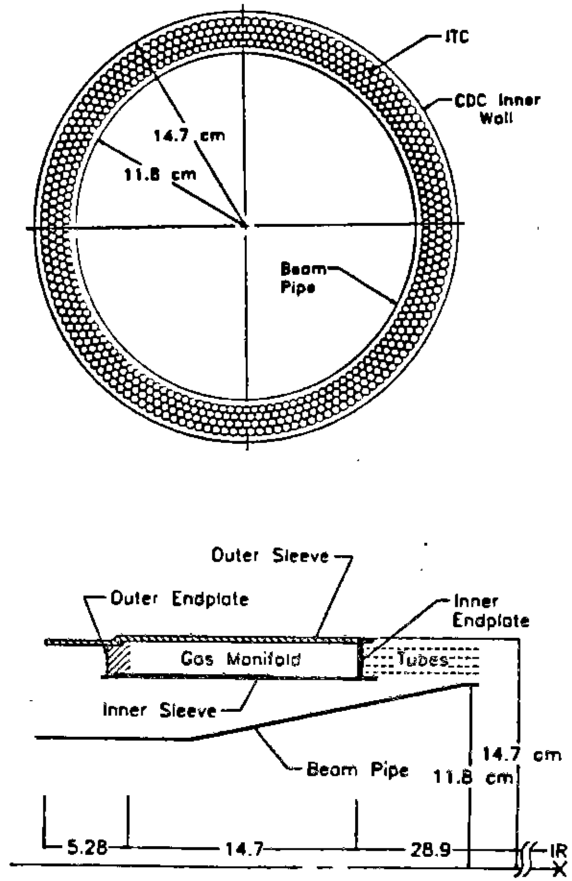

Figure 2.4: A cross-sectional view of the Inner Tracking Chamber

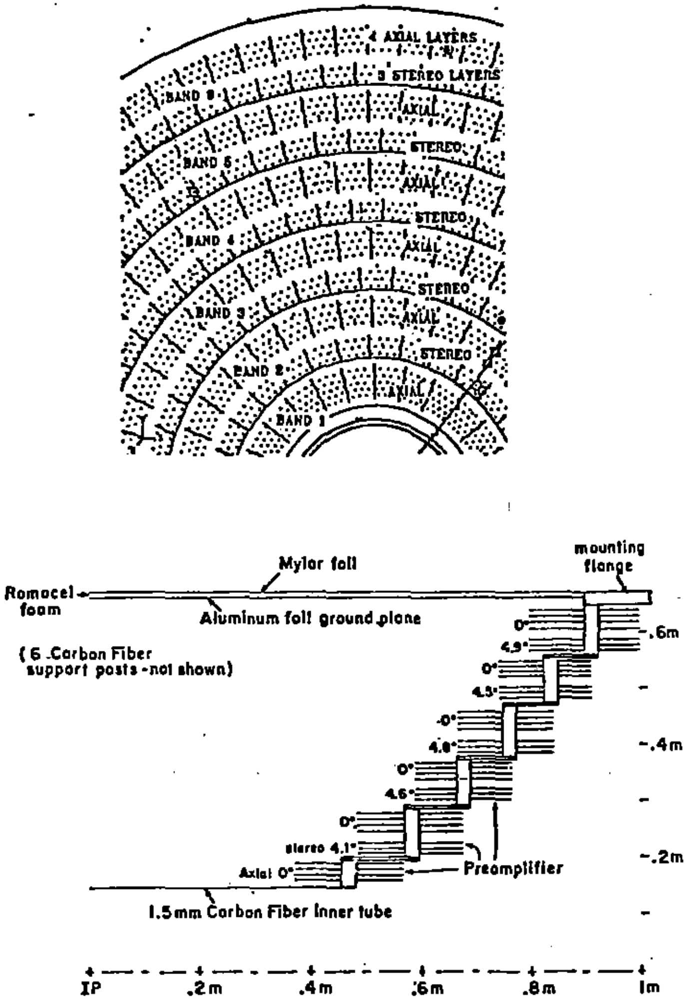

Figure 2.5: Over view of the Central Drift Chamber(CDC)

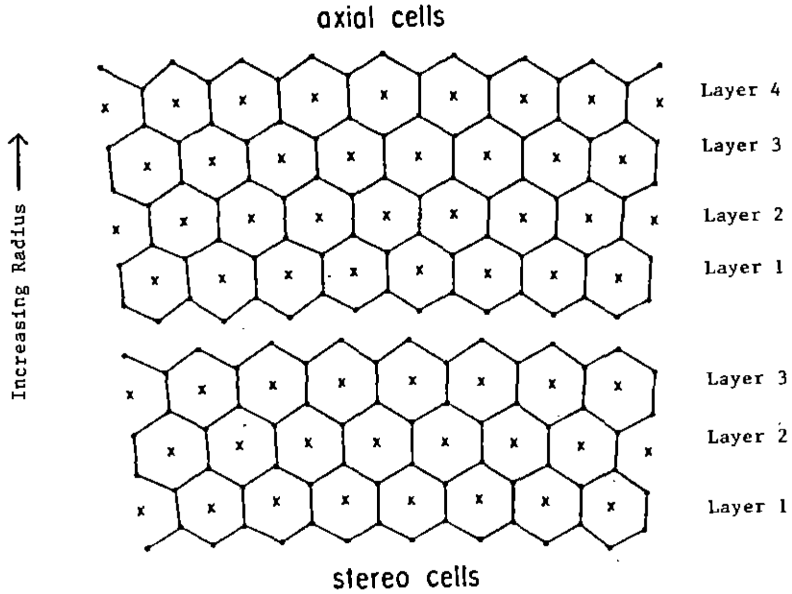

Figure 2.6: The cell structure of CDC

the outermost disk, and extends to a radius of 65 cm. The angular coverage is $|\cos\theta| < 0.87$.

Each of the outer five disks consists of three cylindrical layers of stereo sense wires and four of axial sense wires; the first (innermost) disk has five layers of axial wires. The axial wires run parallel to the beam axis and determine the position of the trajectory points in the $r-\phi$ plane; the stereo wires are at a small angle (typically $5°$) relative to the beam direction and to provide small angle stereo measurements that are used to infer z-coordinates. Each sense wire (20 μm diameter gold-plated tungsten) is surrounded by six field wires (160 μm diameter gold-plated aluminum) arranged in a hexagonal cell unit approximately 6 mm in radius (Fig. 2.6). The CDC was originally filled with HRS gas (Ar 89%, CO_2 10%, CH_4 1%) at atmospheric pressure and is currently filled with a Neon-Ethane mixture (Ne 50%, C_2H_6 50%), which has improved X-ray transmission characteristics. For optimized performance, each CDC cylinder is operated at slightly different voltages with the average being 1.8 kV for HRS gas and 2.1 kV for Neon-Ethane. Signals from the sense wires are processed by preamplifiers mounted directly on the CDC end plates. The preamplifier output signals are amplified again, and discriminated in electronic units located just outside of the iron yoke of the detector. The discriminated signals are transmitted via 30 m long ribbon cable to a TAC-ADC system that is located in an electronics hut that is adjacent to the detector. This system measures the arrival time of the signals which, in turn, is used to infer the drift distance. The calibration constants for each TAC-ADC channel is determined by a pulsing system and are automatically updated in the data taking software. A detail description of the CDC electronics and calibration can be found in Ref. [12]

The disk structure of the CDC is designed to provide local determinations of track vectors (position and direction), which can be used to make estimates of the multiplicity and momenta of the charged particles for purposes of triggering. These vectors also facilitate fast track finding in complicated high multiplicity events. The hexagonal shape of the cells, in addition to realizing the high granularity needed for resolving closely spaced tracks and providing for the fast resolution of the left/right ambiguities, is essential for achieving a good spatial resolution in the 3 tesla magnetic field, which severely distorts the drift trajectories of the ionization electrons. The Lorentz angle, the angle between an electron's drift trajectory and the local electric field direction, can be as large as 80°.

The spatial resolution of the CDC in HRS gas, as estimated from Bhabha scattering events ($e^+e^- \rightarrow e^+e^-$), is $\sigma \sim 170$ μm (Fig. 2.7). This translates into a charged particle transverse momentum resolution of $\Delta p_t/p_t \simeq 0.7\%$ p_t(GeV/c). The measured angular resolution in ϕ and θ are 2.1 and 7.1 mrads respectively. The track reconstruction efficiency for particles in multi-hadronic events with $p_t \geq$ 500 MeV/c that originate within 5 cm of the interaction point is 97%. In the

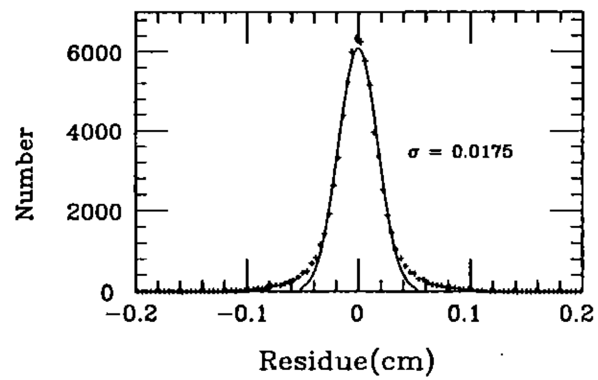

Figure 2.7: The average CDC spatial resolution in HRS gas based on Bhabha events

Neon-Ethane gas mixtures, the average spatial resolution is about 230 μm for the axial layers and 250 μm for the stereo layers. The calibration is described in detail in Appendix B.

2.2.3 The Shower Counter(SHC)

The purpose of the Shower Counter (SHC), [13] is to detect and determine the directions and energies of electromagnetically showering particles ($e^\pm$ and γ's). The SHC is located radially outside of the CDC and covers the angular region $|\cos\theta| < 0.73$. The SHC consists of cylindrical shells (220 cm in length, 79 cm to 110 cm in radii) divided into six individual sextants each covering 60° in ϕ. Each sextant is made up of twenty layers of lead sheets and resistive plastic tube gas proportional counters (Fig. 2.8). The total radial thickness corresponds to 15 radiation lengths. The tubes are filled with gas (HRS gas for the 55 GeV data run and a Ar 49.3% + C_2H_5 49.3% + C_2H_5OH 1.5% mixture for the other energies) at atmospheric pressure. At its operating voltage of 2.15 kV, the SHC operates in the gas proportional mode. The plastic cathode tubes have sufficient electrical conductivity to provide the DC bias voltage but are of sufficiently high resistivity

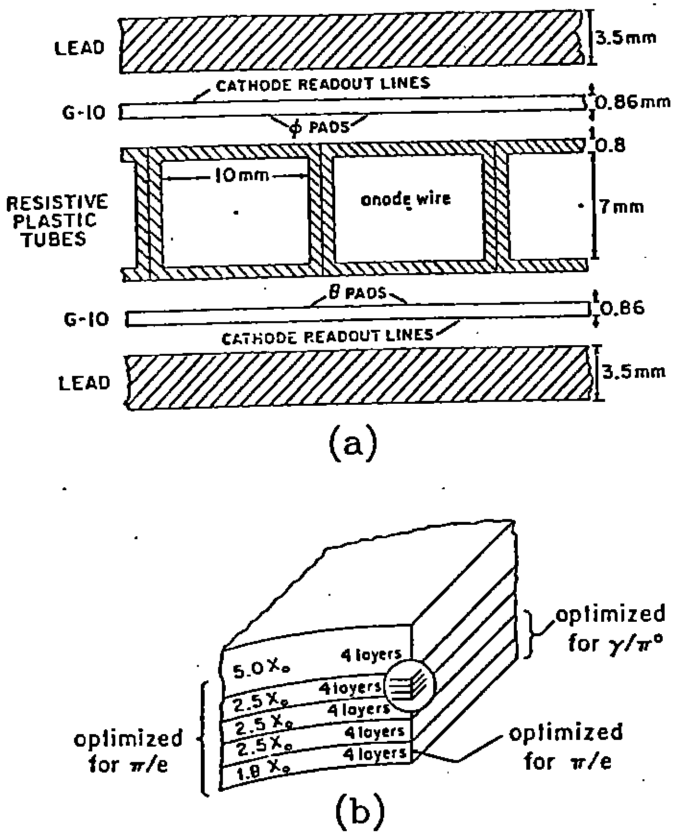

Figure 2.8: The AMY Shower Counter; (a) the layer structure and (b) the longitudinal segmentation.

$\rho \simeq 42 - 81$ kΩcm^2 to permit the fast (decay-time $\simeq$ 100 ns) proportional signals to be registered on the cathode planes of G-10 etched with copper strips that are located outside of the plastic tubes. The induced charges measured on the cathode strips provide precise measurements of the shower location (σ = 3 mm,$\sim$ 4 mrad in angle).

The integrated charge of the signals from the anode wires and the cathode strips are measured directly by an ADC system. The anode signals from the last four layers are preamplified and discriminated. These discriminated signals are used to provide trigger information for minimum ionizing tracks. During data taking, the ADC system is frequently calibrated and the individual pedestals for each channel are automatically subtracted electronically. In each sextant there are four monitor tubes with radioactive ^{55}Fe sources embedded in them. Pulse height data from these tubes are constantly monitored and used to correct for variations of the gas gain caused by fluctuations in atmospheric pressure, temperature, and gas composition.

The cathode signals are ganged together radially every four layers. The results from different [illegible]ial gangs provide information about the longitudinal development of the shower which is useful for e/π discrimination. The anode signals in each cylinder are ganged together in groups of 10 to form towers that subtend a width in ϕ of $\Delta\phi$ = 7.5° and provide twenty depth samplings of the shower. The anode signals are mainly used for triggering and for noise elimination during data analysis, while the cathode signals are mainly for shower energy and position analysis. The energy resolution of SHC is determined from studies of the reactions, $e^+e^- \to e^+e^-$, $e^+e^- \to \gamma\gamma$, $e^+e^- \to e^+e^-\gamma$, and $e^+e^- \to e^+e^-e^+e^-$, to be $\sigma_E/E \sim 23\%/\sqrt{E(\mathrm{GeV})} + 6\%$. For electrons with energy greater than 2.5 GeV, the identification efficiency ranges from 87% for isolated tracks to 70% for tracks inside jets of other particles. The pion rejection factor is approximately 100 for pions with momentum between 1 to 5 GeV [14].

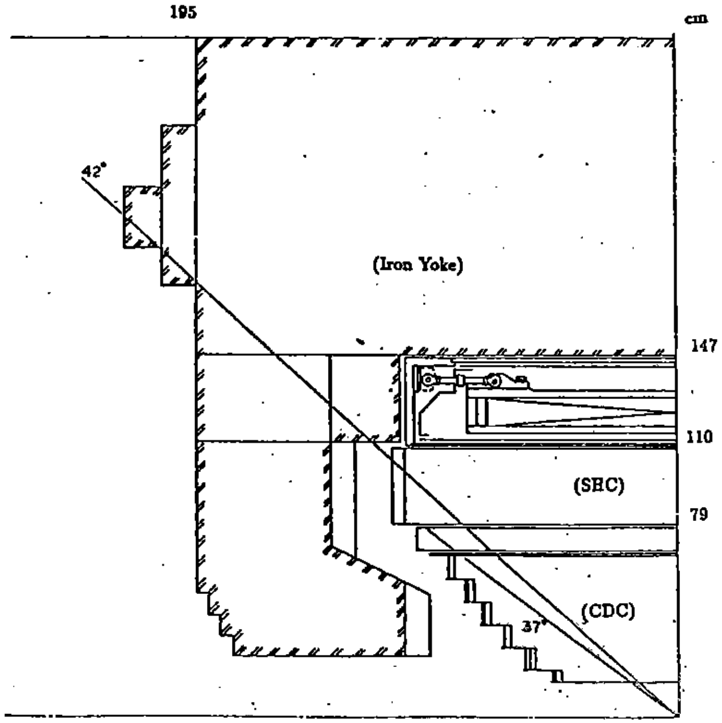

Figure 2.9: The AMY Magnet

2.2.4 The Superconducting Magnet

The AMY magnet(Fig. 2.9) produces a 3 Tesla magnetic field at the center of the detector. This strong magnetic field makes possible the precise measurement of the charged particle momentum while maintaining a small size. It also enables the identification of electrons by the sychrotron X-rays that they emit while bending in the strong magnetic field.

The magnet is an eight layers solenoidal coil with a radial thickness of 10 cm, a length of 154 cm and an inner radius of 119 cm. The coil is made of Nb/Ti

superconducting cable embedded in a copper channel. Included in the copper channel is a strip of high purity aluminum to provide extra stablization. It is cooled by immersion in a bath of boiling liquid helium at 4.2°K, which is maintained by a 300W refrigeration system. The 3 tesla field is generated by a 5000 ampere current and the energy stored in the B field is 40 MJ. To contain the magnetic field, the whole magnet is placed inside a 650 ton hexagonal iron return yoke [15].

Fig. 2.10 show the variation of the Z-component of the magnetic field inside of the detector. This variation affects the performance of CDC both for the position measurements and the inference of the momentum of charged tracks. A complex calibration procedure, which takes into account the effects of variations in the field strength, was employed in order to achieve the resolutions described in the previous section.

2.2.5 The Muon Detector(MUO)

The Muon Detector (MUO) is mounted radially outside of the hexagonal iron return yoke. It consists of four layers of large area drift chambers used for the location of charged particle tracks and a plane of scintillation counters used for time measurements. The angular coverage is $|\cos\theta| < 0.74$. The Muon drift chambers (Fig. 2.11) have four staggered layers of aluminum cells each of which is 5 cm × 10 cm in cross-section with lengths ranging from 2.9 to 6.5 m. The cells are filled with P-10 gas (90%Ar + 10%CH_4) and has an anode wire (100 μm diameter Au-plated tungsten) which is biased to 3.1 kV. The spatial resolution is about 1 mm and the track segment reconstruction efficiency is more than 98%. The Muon scintillation counters have a timing resolution of 2.7~3.5 ns. The primary purpose for these counters is to distinguish cosmic rays, which have a random time distribution and a transit time across the detector of about 25 ns, from muons from the reaction $e^+e^- \rightarrow \mu^+\mu^-$, which pass through the scintillators about 13 ns after the beam crossing and have an apparent transit time of zero.

The materials of SHC, AMY Magnet and the iron return yoke amount to ~9 nuclear absorption lengths. Thus most hadrons are absorbed in the iron; charged particles that penetrate this amount of material are most likely muons. Trajectories

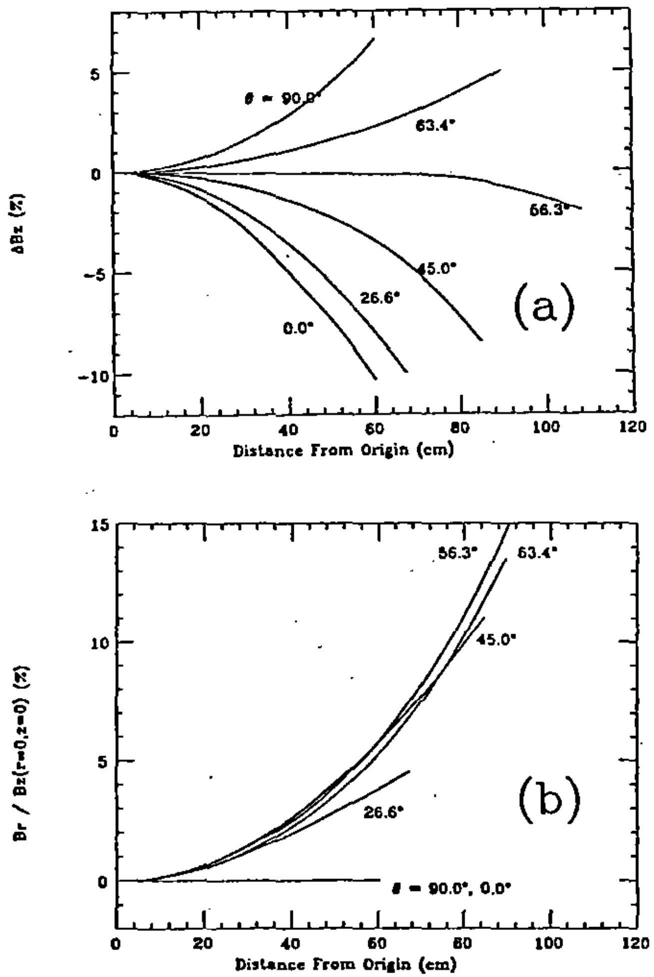

Figure 2.10: The variation of the field strength. (a) The variation in the z-component (the beam direction) of the field. (b) The variation in the radial component.

of charged particles, determined from the measurements of the ITC and CDC, are extrapolated through the iron assuming the particle to be a muon. If the distance between the extrapolated track position and the track segment measured by Muon drift chambers is less than 1 m, and the timing of the track with respect to beam crossing, as measured by the the Muon scintillation counters, is between 0 and 35 ns, the track is identified as a muon. The hadron filter penetration probability of a 5 GeV/c (10 GeV/c) π-meson is estimated to be 0.2% (0.5%). Due to AMY detector's compact size, the probability of misidentification due to the decays-in-flight of $\pi^{\pm}$ and $K^{\pm}$ mesons is minimized; it is $\simeq 1.3\%/p(\mathrm{GeV/c})$ for π mesons and $\simeq 6\%/p(\mathrm{GeV/c})$ for K mesons. The efficiency of the muon identification criteria is about 96% for $p > 3.0$ GeV/c (82% for $p > 2.0$ GeV/c).

2.2.6 The Endcap Detectors

The detectors described previously cover the region of large opening angle with respect to the beam axis. The small angular region is covered by the Ring Shower Counters (RSC) ($0.74 < |\cos\theta| < 0.90$) and the Pole Tip Counter (PTC) ($0.90 < |\cos\theta| < 0.96$)(Fig. 2.12).

The RSC consists of two alternating layers of lead and scintillator with a total thickness of 3.6 radiation lengths. The shower energy resolution is about 30% for 28 GeV/c electrons. When combined track information from the ITC and CDC, it can be used to distinguish between electrons and minimum ionizing particles.

The PTC [17] is made up of two layers of lead/scintillator calorimeters for energy measurement, and a plane of proportional tubes sandwiched between them for position measurement. The calorimeters have a total thickness of 14 radiation lengths and an energy resolution of 11% for 28 GeV/c electrons. The proportional tube is made of resistive plastic. On both sides of the tubes there are G-10 cathode boards etched with copper strips that serve a similar function as the cathodes of the SHC. The proportional tubes are operated at 2.28 kV (just below the streamer mode) for efficient detection of minimum ionizing particles, and provide a position resolution $\sim 0.2°$ (0.8°) in θ (ϕ) direction. The primary function of the PTC is to determine the luminosity by detecting Bhabha scattering events in the angular

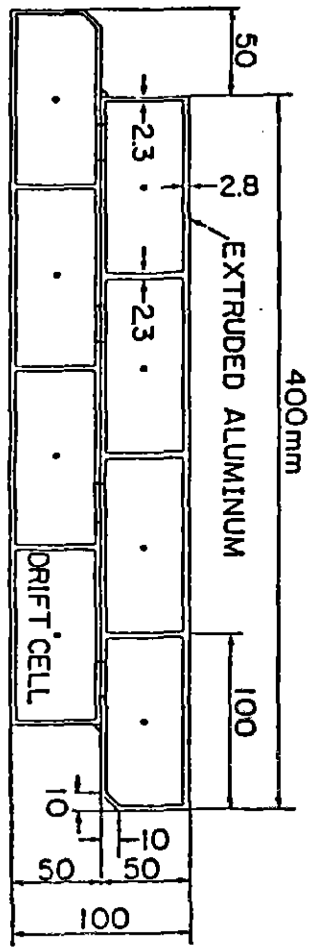

Figure 2.11: The Muon Chamber.

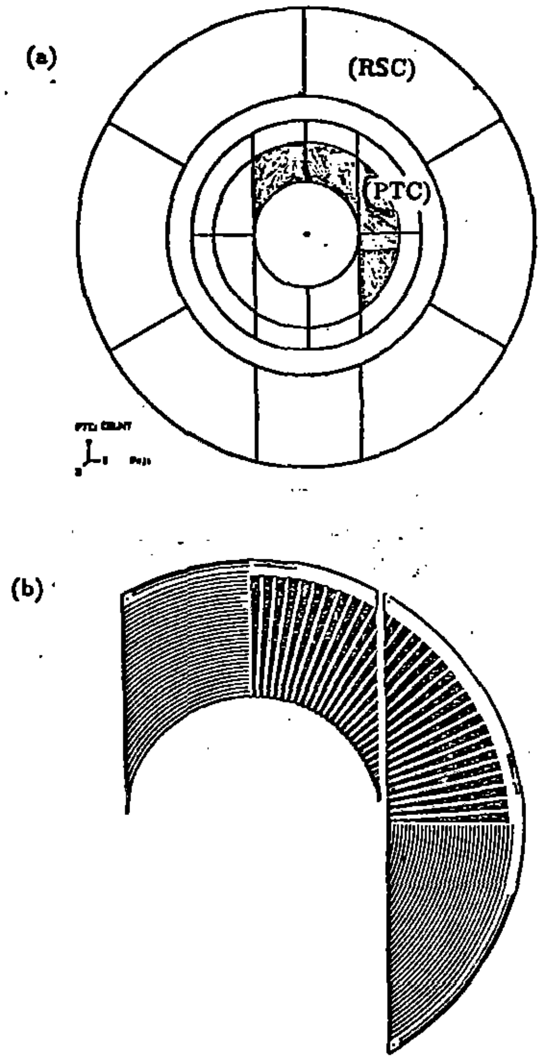

Figure 2.12: (a)The configuration of RSC and PTC. (b)The etching pattern of the PTC cathode strips. Shadowed region in figure(a) corresponds to figure(b).

region $15° \leq \theta \leq 24°$. The overall systematic error on the luminosity measurement is 4.2%.

In addition, there is calorimeter made of BaF_2 crystals in the angular region $4.0° < \theta < 6.0°$. These are detect Bhabha scattering and serve as an online instantaneous luminosity monitor.

2.2.7 The X-Ray Detector and the Trigger Counters

Originally, there were twelve scintillation counters in the space between CDC and SHC to provide event trigger and background discrimination. In the summer of 1987, these counters were replaced by the X-Ray Detector (XRD). The XRD is a radial drift chamber filled with a Xenon-Propane gas (95% Xe, 5% propane). Its purpose is to detect synchrotron X-rays emitted by electrons bending in the 3 Tesla magnetic field. This information will be combined with the SHC data give a better electron identification. The data from XRD was not yet available for the analysis reported here.

2.2.8 Trigger and Data Acquisition System

At TRISTAN, the beam crossings occur at a rate of 200 kHz. The trigger system is designed to accept events with potential physics interest at a manageable rate(< 3 Hz) for the data acquisition system. The trigger decision is made by using various signals from the detector to address memory lookup units that have preprogrammed patterns which decide whether or not to accept the event. There are two major types of triggers: track triggers which based on the information from ITC, CDC and MUO; and energy triggers based on SHC, PTC, RSC. Since there are many redundancies in the various triggers, the efficiencies for most physics processes of interest are close to 100%.

Signals from each of the detector components are processed and digitized in a computer controlled FASTBUS system. A CAMAC system is used to monitor and to control the operational hardware (e.g. voltage supplies, calibration system, environmental monitors, etc.) of the detector and to do the triggering logic. All the digitized data are sent via an interface (VAX FASTBUS Processor Interface) to the

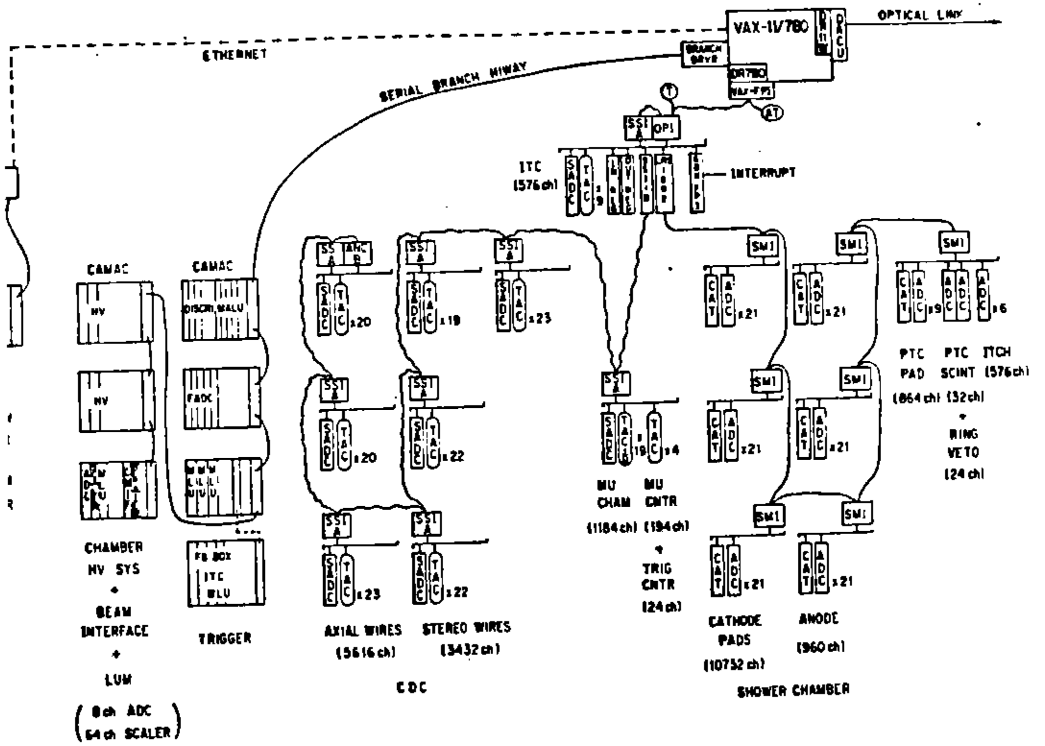

Figure 2.13: The AMY data acquisition system.

VAX 11/780 computer where the data are temporarily stored. The online program in the VAX controls the data taking and monitors the operational status of the entire system. The data are sent from the VAX to a FACOM M382 computer, situated in the KEK computing center, via a fast optical link (DACU). In the FACOM, the original data are rewritten into TRISTAN Bank System format and stored in a Cassette Tape Library for later analysis. Figure 2.13 illustrates the data acquisition system of the AMY detector.

Chapter 3

Data Selection

The data used in this analysis were taken between the fall of 1986 and the summer of 1989. The center of mass energy ranges from 50 GeV to 61.4 GeV. The accumulated luminosities at different energies are shown in Fig. 3.1. The events used for the analysis reported here are selected in a sequence of stages in order to eliminate background events while retaining events of interest with high efficiency.

3.1 First Stage Selection

The triggering requirements for the AMY detector are kept as loose as possible, consistent with the maximum data acquisition rate of about 3 Hz, in order to ensure a high triggering efficiency for a broad range of processes. As a result, most of the triggers are caused by uninteresting background processes such as interactions of stray beam particles with material in the vicinity of the storage ring (beam-wall events), beam particle interactions with the residual gas of the vacuum system (beam-gas events), cosmic rays, electronic noise etc. To select interesting events and eliminate these backgrounds, an elaborate offline event-filtering procedure was developed.

For the purpose of economizing on computing time and handling procedures in the subsequent analysis, the raw data is first passed though a fast reconstruction and filtering program that eliminates about 70% of the triggered events. This procedures involves estimating energy in SHC with a rough calibration, and the determination of charged track momenta and multiplicity using the reconstructed

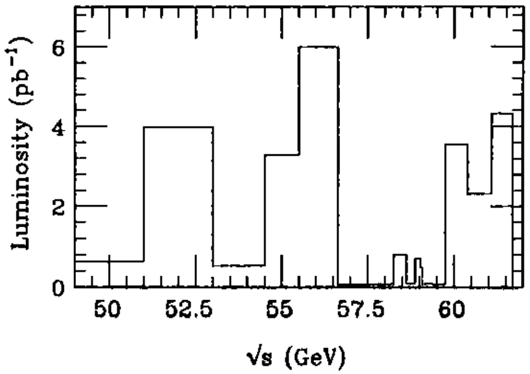

Figure 3.1: accumulated luminosity at different center of mass energies.

track segments in CDC. The event is accepted if it has more than 2.8 GeV of energy in SHC, or at least one track with transverse momentum greater than 1.5 GeV/c^2. Events with two or more charged tracks and more than 1.5 GeV in SHC are also accepted.

The events that survive this first filter are subjected to a more elaborate analysis. The information in the SHC, RSC and PTC are processed using their more accurate calibrations to obtain the positions as well as energies of showering particles. In addition, the timing information in ITC, CDC, MUO are converted to positional information to reconstruct the trajectories of charged particles. The track momenta are determined from the CDC information using a fast tracking routine (ACE) [18] for finding and reconstructing charged tracks. Afterward, the data are divided into several categories for further physics analysis. Figure 3.2 illustrates the filtering procedures.

The data in this analysis come primarily from the Low Multiplicity sample, which are all the events with at least two good reconstructed charged tracks in CDC. A good reconstructed track are those with measured momentum greater than 0.75 GeV/c^2, and a vertex position within 10 cm in $|z|$ and 2 cm in $|R|$ of the origin.

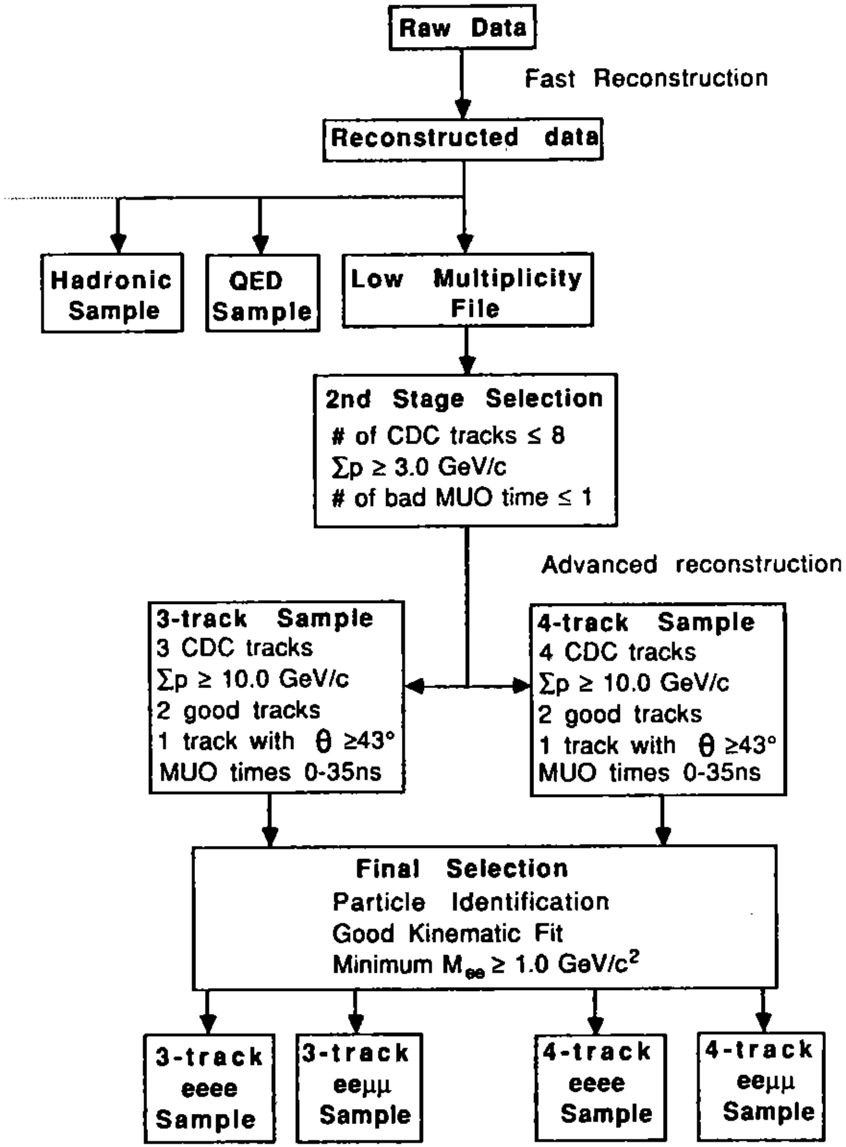

Figure 3.2: Data filtering procedures

3.2 Second Stage Selection

To further reduce the data sample, events from the Low Multiplicity sample are selected according to the following criteria:

- CDC track
  - no more than 8 CDC charged tracks;
  - total momentum of the tracks $\sum_i |\mathbf{p}_i| \geq 3.0$ GeV/c;
- Cosmic Ray cut
  - no more than one MUO tracks outside the timing limit defined for muon track(c.f. The Muon Detector section in Chapter 2);

These criteria are established in order to cut away most of the beam-wall, beam-gas, cosmic ray and high multiplicity hadronic events. However, they are loose enough to retain all events with the characteristics of those we want to study. The criteria are set so that no events of interest are lost due to inaccuracies resulting from the still crude level of the reconstruction algorithms used at this stage. Roughly 37% of the Low Multiplicity sample are selected by this stage. To test the efficiency of this selection, we subjected all of the $e^+e^- \to \tau^+\tau^-$, $e^+e^- \to \mu^+\mu^-$ and almost all $e^+e^- \to e^+e^-$ candidates from the $50 \leq E_{cm} \leq 55$ GeV data samples to these selection criteria. These data samples are obtained from other physics groups specializing in the study of those particular processes. In general, the data are selected *either* by requiring significant energy deposited in SHC *or* high momentum charged tracks in CDC. The few events from these samples that failed to pass this selection stage were examined individually and are found to be due to cosmic rays Fig. 3.3.

The events that survive to this stage are then processed by a more sophisticated CDC tracking algorithm, called DUET [18] [19].

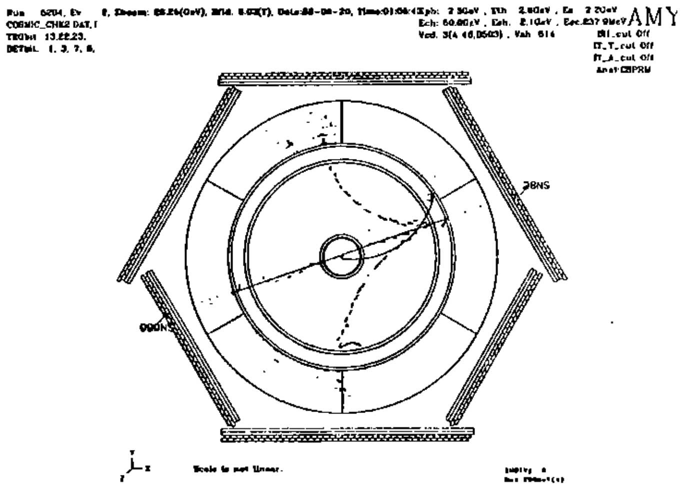

Figure 3.3: Example of event induced by cosmic ray that was rejected at the second stage of data selection. The iron return yoke is not shown in the picture.

3.3 Third Stage Selection

At this stage, the remaining data are divided into different samples according to whether they had three or four charged tracks. For the three track sample, the events are selected according to:

- CDC track
  - only 3 CDC charged tracks present;
  - total momentum of the tracks $\sum_i |\mathbf{p}_i| \geq 10.0$ GeV/c (if the track is reconstructed using less than 5 axial or 3 stereo hit wires, their momentum information is not used for selection because of the potential for large error);
  - at least 2 tracks must originate from within 5 cm in $|z|$ and 1 cm in $|R|$ of the interaction point;
  - at least 1 track with opening angle $\theta \geq 43°$;
- Cosmic Ray cut

  - all MUO times are between 0 and 35 ns.

The four-track sample is similarly selected with the exception of requiring four charged tracks.

These samples are further divided into four groups. The three and four-track $e^+e^-\mu^+\mu^-$ groups are selected by requiring at least one MUO hit in the event. The remaining events form the three and four-track $e^+e^-e^+e^-$ groups. These groupings are used for the final selection and analysis of the $e^+e^-e^+e^-$ and $e^+e^-\mu^+\mu^-$ events.

3.4 Final Selection

A visual inspection of computer generated displays of events from the four selected groups revealed that they are mostly $e^+e^- \rightarrow$ multi-hadron annihilation events, $e^+e^- \rightarrow \tau^+\tau^-$ events, radiative Bhabha events ($e^+e^- \rightarrow e^+e^-\gamma$) where the photon converted into an e^+e^- pair in the material of the beam pipe or the inner part of the detector, or events where the reconstruction software had produced two tracks from the hits left by a single particle.

Particle identification

To eliminate these backgrounds, we first apply a set of particle identification selection criteria to the events. These consist of comparisons of the energy deposited by the charged track in the SHC, RSC or PTC electromagnetic calorimeters (E) with its momentum measured in the charged particle tracking system (p). In addition, the MUO system is used to provide positive identification of muons as described in Chapter 2. Specifically, we assign particle identifications as follows:

- electron : $E/p \geq 0.5 + p \geq 1.0$ GeV/c, *or* $E \geq 5.0$ GeV
- non-electron : $E/p < 0.5 + p \geq 1.0$ GeV/c;
- muon : $E/p < 0.5$ + MUO hit + $p \geq 2.5$ GeV/c.

Because the average energy deposited by a minimum ionizing particle in SHC, RSC and PTC is between ~100 to 300 MeV, the greater than 1 GeV/c momentum requirement is needed to ensure a definite identification. An $e^+e^-\mu^+\mu^-$ event is required to have at least three identified tracks, with at least one identified as an electron and at least one as a muon. At least three identified electrons are required for an $e^+e^-e^+e^-$ event. Furthermore, at least one of the identified muons or electrons has to be within the angular region of $|\cos\theta| \leq 0.707$. Detector-simulated two-photon untagged events are used to study the efficiency of electron identification using the above criteria. Between $135° \geq \theta \geq 45°$, the electron identification efficiency is about 98%, while roughly 13% of minimum ionizing particles are misidentified as electrons.

Kinematic fitting

The angles of the charged tracks in the CDC are generally well measured. We can improve the determination of the track momenta further by adjusting the kinematic information of the tracks to satisfy the conservation of 4-momentum with minimal deviation from the original measurements. This method is generally referred to as constrained kinematic fitting. Obviously, events with all the final particles well measured will have small errors while events with missing particles will have large errors under the fit. Because events like $e^+e^- \to \tau^+\tau^-$, $e^+e^- \to e^+e^-\tau^+\tau^-$ have at least two unobserved neutrinos in the final state (decay products of the τ), they are usually eliminated by the kinematic fitting procedure. A version of SQUAW [22], adapted for the AMY detector environment, is used for the kinematic fitting.

For the four-track events, we use all of the charged tracks and require the quality of the fit to be good. Since there is one track missing in the three-track events, we use the missing momentum together with the three charged tracks (1-C fit). In addition to a good fit quality, we require the fitted value for the missing momentum vector points outside of the efficient detecting region ($|\cos\theta| \geq 0.906$). To determine the cuts, we compare the fitted results between the detector-simulated Monte Carlo events for the $e^+e^- \to \tau^+\tau^-$ and $e^+e^- \to e^+e^-\mu^+\mu^-$ processes. These events are generated with three or four charged tracks within the acceptance region of the detector and are selected by the same criteria as the real data. A more extensive discussion of these Monte Carlo events is presented in

chapter 4. For the four-tracks events, the background are effectively reduced while remaining sensitvie to the signal by requring the χ^2 of the fit to be ≤ 100 (Fig. 3.5). The same is true for the three-tracks events if we place the cut at $\chi^2 \leq 50$ and $\theta_{miss} \geq 0.906$ (Fig. 3.6).

Invariant mass of e^+e^- pair

A potential background for the four-lepton processes are the radiative events $e^+e^- \to e^+e^-\gamma$, $e^+e^- \to \mu^+\mu^-\gamma$ with the γ converted to an e^+e^- pair in the materials surrounding the interacting region. In real photon conversion, the invariant mass of the e^+e^- pair tends to be very nearly zero. Therefore, we require the minimum invariant mass of any e^+e^- pair in any of the events to be greater than 1 GeV/c^2. With the current CDC spatial resolution, the error in the invariant mass measurement for a pair of oppositely charged tracks is typically 20% for e^+e^- masses below 1 GeV/c^2. Therefore, the e^+e^- invariant mass requirement effectively cuts away background from real photon conversion. As a result of this cut, 18 events are lost in the 4-tracks sample where the expected number of events from the $e^+e^- \to e^+e^-\gamma$, $e^+e^- \to \mu^+\mu^-\gamma$ processes is about 15. We don't apply a similar cut to the $\mu^+\mu^-$ pair because the probability for a real photon converting to a $\mu^+\mu^-$ pair is more than four orders of magnitude smaller than that for conversion to e^+e^- pairs. Since the probability for photon conversion to e^+e^- is measured to be 3% [3], it is safe to neglect the probability of real photon conversion to $\mu^+\mu^-$ pairs in this analysis.

Examples of events that fail the constrained kinematic fitting procedure and the e^+e^- invariant mass cut are shown in Fig. 3.4.

3.5 Summary of Selected Events

The event selection cuts are summarized in Table 3.1. Computer generated displays of all of the events that passed these cuts were carefully inspected to ensure that there was no error in any of the selection procedures. In total, there are seven four-track $e^+e^-\mu^+\mu^-$, sixteen three-track $e^+e^-\mu^+\mu^-$, one four-track $e^+e^-e^+e^-$, and sixteen three-track $e^+e^-e^+e^-$ events selected. Table 3.2 summarizes these results.

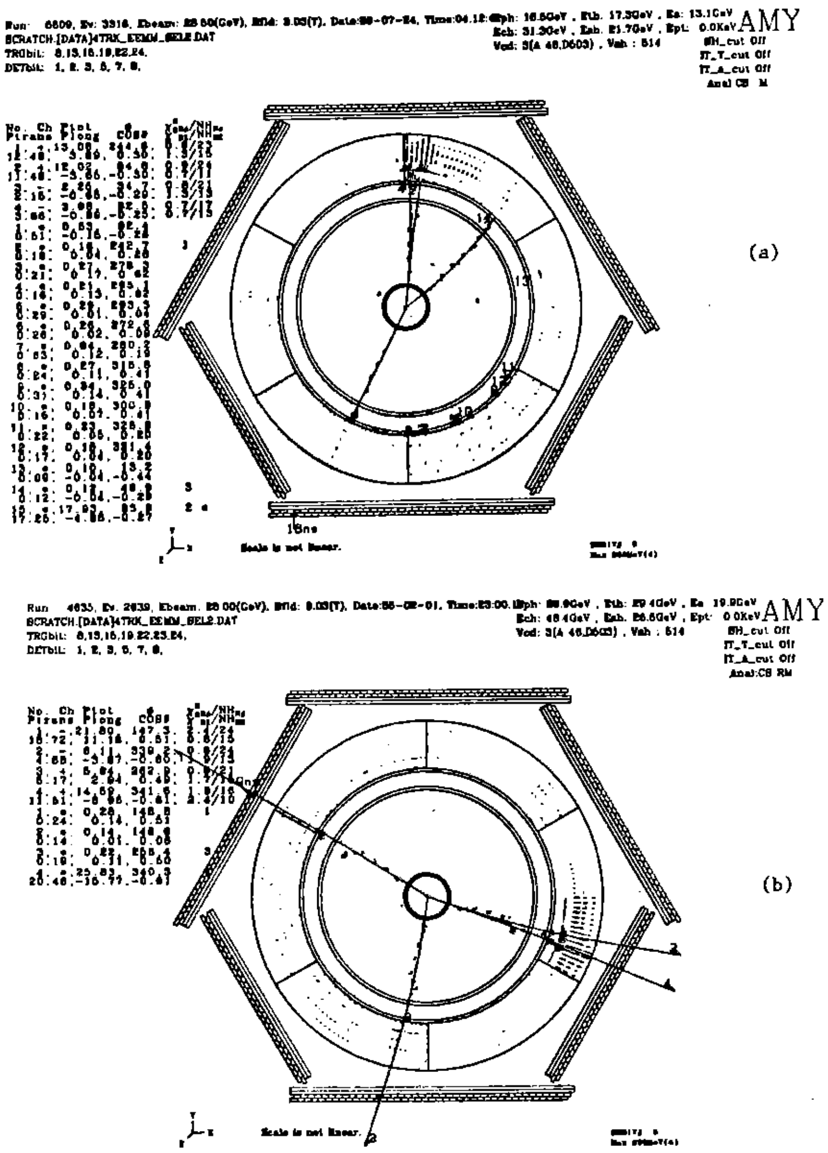

Figure 3.4: Examples of failed events. (a) χ^2 of kinematic fitting too big; (b) invariant mass of e^+e^- pair too small.

Event type:	Selection Cuts
four-track $e^+e^-\mu^+\mu^-$	4 charge tracks $\lvert\cos\theta\rvert \leq 0.906$; ≥ 3 identifiable tracks; at least 1 μ : $135° \geq \theta_\mu \geq 45°$; at least 1 e : $135° \geq \theta_\mu \geq 45°$; minimum $M_{ee} \geq 1$ GeV/c^2.
three-track $e^+e^-\mu^+\mu^-$	3 charge tracks $\lvert\cos\theta\rvert \leq 0.906$; 3 identifiable tracks; at least 1 μ : $135° \geq \theta_\mu \geq 45°$; minimum $M_{ee} \geq 1$ GeV/c^2.
four-track $e^+e^-e^+e^-$	4 charge tracks $\lvert\cos\theta\rvert \leq 0.906$; ≥ 3 identifiable tracks; at least 2 e : $135° \geq \theta_e \geq 45°$; minimum $M_{ee} \geq 1$ GeV/c^2.
three-track $e^+e^-e^+e^-$	3 charge tracks $\lvert\cos\theta\rvert \leq 0.906$; 3 identifiable tracks; at least 1 e : $135° \geq \theta_e \geq 45°$; minimum $M_{ee} \geq 1$ GeV/c^2.

Table 3.1: Summary of the selection cuts for the four-lepton events.

of the events will be discussed in detail and compared with theoretical expectations in Chapter 5.

3.6 Backgrounds

To check the effectiveness of the selection criteria for eliminating the background processes such as $e^+e^- \to q\bar{q} \to$ hadrons, $e^+e^- \to e^+e^-q\bar{q}$, $e^+e^- \to \tau^+\tau^-$ and $e^+e^- \to e^+e^-\tau^+\tau^-$, similar criteria are applied to the detector-simulated events. For the $e^+e^- \to q\bar{q} \to$ hadrons and $e^+e^- \to \tau^+\tau^-$ events, we used the samples prepared for different measurements [20] [21]. The $e^+e^- \to e^+e^-\tau^+\tau^-$ events are generated by the Vermaseren program with a $p \geq 0.3$ GeV/c^2 cut. Although Vermaseren program only includes the multiperipheral and bremsstrahlung diagrams, it is sufficient for the $e^+e^-\tau^+\tau^-$ study because the contribution from the conversion and annihilation are at least 4 orders of magnitude smaller than the multiperipheral for the same kinematic regions. The number of background events generated are equivalent to an integrated luminosity of 244pb^{-1} for the hadronic

$\sqrt{s}$(GeV)	50,52	54	55-57	57.25-59.5	60-61.4	Total
Integrated luminosity(pb^{-1})	4.62 $\pm$0.04	0.54 $\pm$0.02	14.65 $\pm$0.08	2.57 $\pm$0.03	11.36 $\pm$0.06	33.74 $\pm$0.11
Event type: $e^+e^-\mu^+\mu^-$	2		3		2	7
$e^+\mu^+\mu^-$			2	1	2	5
$e^-\mu^+\mu^-$	2		6		2	10
$e^+e^-\mu^+$			1			1
$e^+e^-\mu^-$						
$e^+e^-e^+$		1	3		2	6
$e^+e^-e^-$			7		3	10
$e^+e^-e^+e^-$					1	1

Table 3.2: Number of events vs center-of-mass energy

generated are equivalent to an integrated luminosity of 244pb^{-1} for the hadronic events, 500pb^{-1} for the $\tau^+\tau^-$ events, and 383pb^{-1} for the $e^+e^-\tau^+\tau^-$ events.

The effects of the cuts on the background event sample are summarized in Table 3.3. Most of the background events are cut away by the data filter used in the 3 stages of selection for the real data. Those remaining are effectively removed by the kinematic fitting requirement. Because of the missing momentum and energy in the $\tau^+\tau^-$ and $e^+e^-\tau^+\tau^-$ events, they tend to result in poor quality kinematic fits. Figure 3.5 shows that the χ^2 distribution for the four-track $e^+e^-\mu^+\mu^-$ events peaks at much smaller values than that for $\tau^+\tau^-$ events. By applying a cut at $\chi^2 = 100$, the event number is reduced to the same as that for the QED four-track $e^+e^-\mu^+\mu^-$ event. None of these remaining events pass the electron/muon requirements (see Table 3.1 for the real data). For the $e^+e^-\tau^+\tau^-$ background, the χ^2 cut alone is enough to keep it to essentially zero.

On the other hand, cuts on χ^2 alone are not enough to reduce the background for the three-track event to negligible level while maintaining the sensitivity for the real events. Here, we further require that the polar angle of the missing momentum(θ_{miss}) returned from the fitting procedure point outside of the effective detection region, i.e. $\theta_{miss} < 25°$. With this requirement, background from these processes is at the 10% level. This is demonstrated by Fig 3.6, which shows a scatter-plot of χ^2 vs θ_{miss} for signal and background events.

	Original # events	Data filter	Kinematic Fitting	e, μ requirement*	# Expected at 33.8pb^{-1}
four-track					
$q\bar{q}$	36653(244pb^{-1})	93	0	0	0
$\tau^+\tau^-$	20000(500pb^{-1})	2331	33	0	0
$e^+e^-\tau^+\tau^-$	70000(383pb^{-1})	97	0	0	0
three-track					
$q\bar{q}$	36653(244pb^{-1})	28	2	0	0
$\tau^+\tau^-$	20000(500pb^{-1})	774	11	2[1]	0.1[0.1]
$e^+e^-\tau^+\tau^-$	70000(383pb^{-1})	114	34	9[4]	0.8[0.4]

Table 3.3: Effect of data selection cuts on backgrounds event. Numbers in parentheses are the integrated luminosity of the amount of background events generated and the numbers in square brackets refer to the background events passing the $e^+e^-\mu^+\mu^-$ selection. * Similar momentum and angular requirements for e and μ as listed in table 3.1.

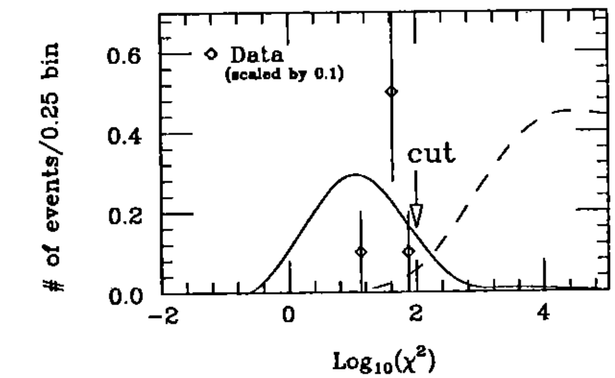

Figure 3.5: Comparison of the χ^2 distribution from kinematic fits to simulated four-track $e^+e^-\mu^+\mu^-$(solid line) and $\tau^+\tau^-$(dashed line) events . The cut value of $\chi^2 \leq 100$ is indicated by an arrow.

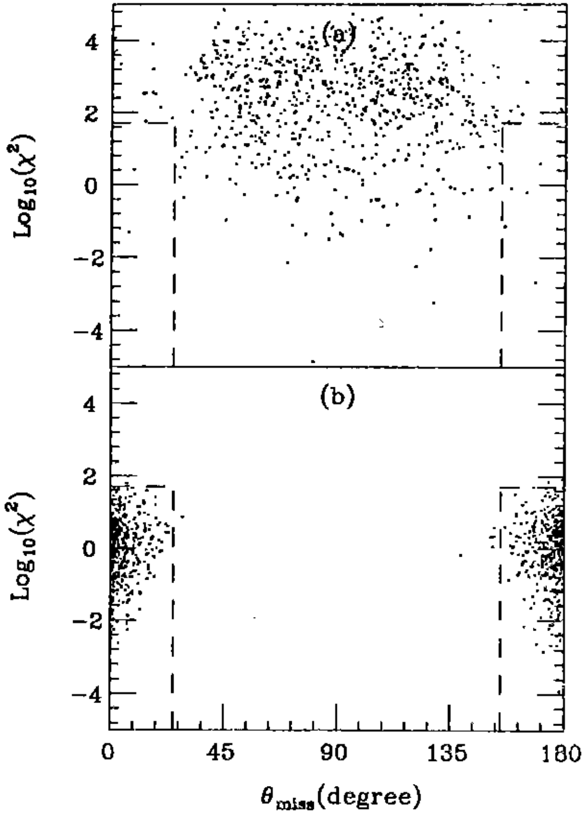

Figure 3.6: Scatterplot of kinematic fitting χ^2 vs θ_{miss} for the events with 3 CDC tracks. (a) Simulated $\tau^+\tau^-$ events; (b) simulated $e^+e^-\mu^+\mu^-$ events. The cut regions are indicated by the dashed lines.

real data. Events with 3 charged tracks are required to have at least one electron or one muon with $\theta \geq 45°$ from the beam axis and $p \geq 2.5\ GeV/c$. An additional electron track is required to be within the same angular range for the events with 4 tracks. The minimum e^+e^- invariant mass cut is also applied for the $e^+e^-e^+e^-$ background study. This is done by assuming that all the charged tracks are electron. The last set of requirements virtually eliminates the backgrounds from the four-track $e^+e^-e^+e^-$, $e^+e^-\mu^+\mu^-$ event samples. The background for the three-track $e^+e^-e^+e^-$, $e^+e^-\mu^+\mu^-$ are reduced to the few percent level.

We also investigated the probable contamination from $e^+e^- \rightarrow e^+e^-q\bar{q}$ events by looking at a smaller sample of events (luminosity $\sim$ 5.5pb^{-1}) generated by Vermaseren program with Lund 6.3 fragmentation algorithm [23]. None of the events passed the data filter. A similar study by Petradza [37] also shows that the contamination from the $e^+e^- \rightarrow e^+e^-q\bar{q}$ to the four-track events are negligible. Therefore, we are confident that the AMY data sample are quite clean and they should be good representation of the four-lepton events.

Chapter 4

Theoretical Calculation

4.1 Calculation of the Four-lepton Processes

4.1.1 The Monte Carlo programs

Three independent programs, written by Vermaseren [24], Berend, Daverveldt and Kleiss [27], and Kuroda [28], are used to calculate the cross sections for the four-lepton processes and generate events. The results from the different calculations are used as a cross check and to compare with the experimental data.

Vermaseren and Kuroda programs

Vermaseren's program is widely used. It was the first program to calculate the four-lepton cross section using Vegas [25], an adaptive Monte Carlo integration routine that automatically concentrates the evaluations in the regions where the integrand magnitude is large. In evaluating the cross section, it achieves numerical stability by changing the integration variables so as to avoid the numerous poles that occur in the integrand. The results are quite accurate under most experimental conditions. However, since the program only calculates the multiperipheral and bremsstrahlung groups and their mutual interference, it is adequate only when the contribution from the other processes can be safely ignored. Such a situation is true in the case of untagged events. In the case of tagged events, where three or all final state particles are observed at large opening angles(θ), it is not a-priori reasonable to neglect the effects of the annihilation and conversion groups. To evaluate the

contribution to the $e^+e^-\mu^+\mu^-$ process from these two groups, we used the Kuroda program. This program calculates the combined cross section of these latter two groups including the effects of their interference. It uses an approach that is similar to that of Vermaseren for achieving numerical stability. The integration and event generation are performed by means of the programs Bases&Spring [29].

The Berend, Daverveldt, and Kleiss programs

The results from the two above mentioned calculations are then compared with those derived from the BDK program, which includes a full evaluation of all four groups of diagrams, including their interference. BDK uses an approach for evaluating the cross sections and, thus, differs from the approach of Vermaseren and Kuroda. First of all, the events are generated in each of the groups according to approximate expressions for differential cross sections that can be integrated analytically. The interference terms among the diagrams within the groups are accounted for by assigning the generated event a weighting factor(W) that is equal to the ratio of the exact differential cross section($d\sigma$) to the approximate one ($d\sigma'$), i.e. $W = \frac{d\sigma}{d\sigma'}$. At a later stage, this W is multiplied by another factor X to form a final weight(FT). The factor X includes the interference among the four groups of Feynman graphs and is determined by

$$X = \frac{\sum_i |M_i^2|}{|\sum_i M_i|^2}, \tag{4.10}$$

where M_i's is the matrix element for each of the Feynman graph groups. The significance of the generated event is then determined. Events that fail the kinematic selection requirements simply have their weight W set to zero. In the end, the final weight(FT) is compared with a random number that is generated within the boundary of an estimated maximum weight value to determine whether the event will be accepted as an unweighted event. The exact cross section for each group is simply its average weight multiplied by its approximate cross section. Similarly, the total exact cross section is just the product of the average final weight(FT) and the total approximate cross section, which, in turn, is just the sum of the approximate cross sections of the four groups of Feynman graphs:

$$\sigma = < FT > (\sigma'_{multiperipheral} + \sigma'_{bremsstrahlung} + \sigma'_{conversion} + \sigma'_{annihilation}). \tag{4.11}$$

In the actual calculation, the approximate cross sections contain 2 sets of tuning parameters for maximizing the program efficiency. Such a method gives accurate results efficiently if the approximate equations have peaking structures that are similar to those of the actual integrands. There are in total three versions of the programs for the four-lepton studies, specialized for the untagged [30], single-tag [31], and double-tag experimental conditions. For the last case we use the latest version that was specially modified for the double-tag condition by R. Kleiss. It includes the effect of Z^0 exchange and is currently being used in CERN by J. Hilgart. Although the calculations are complete, the programs are not very efficient for generating unweighted events in the region of phase space being studied in this experiment. In addition, in the evaluation of the bremsstrahlung group of diagrams, the BDK program for single-tag (three-track) events generates muon pairs from the positron line only. The authors instruct the users to symmetrize the final results 'by hand'. Such a built-in symmetry is not appropriate for studying possible experimental asymmetries arising from the interference between the different groups of diagrams. Therefore, we can only use the program to evaluate the individual and total cross sections from which we can deduce the significant of interference, but not for detailed comparison of particle asymmetries. The situation is worse for the $e^+e^-e^+e^-$ events where no program exists for the single-tag case and the calculation for double-tag events is extremely slow. Therefore, we settle for less accurate results from BDK as a check on the Vermaseren program, which we use to compare to our results.

4.1.2 Result of the calculation

The calculation and event generation are first performed using looser selection criteria than those that are applied to the experimental data. This allows room for smearing effects due to detector resolution. Because the Monte Carlo programs were written by different authors and each uses different methods for applying kinematic constraints, making direct comparisons of their results is difficult. In order to make a meaningful comparison, tighter kinematic cuts are subsequently applied to the events generated by the three programs. Table 4.1 gives a summary

	three-track $e^+e^-\mu^+\mu^-$	four-track $e^+e^-\mu^+\mu^-$	three-track $e^+e^-e^+e^-$	four-track $e^+e^-e^+e^-$
BDK	only 3 tracks $\lvert\cos\theta\rvert \leq .94$; $p \geq .3$; $M_{ee} \geq .5$; at least 1 μ $\lvert\cos\theta\rvert \leq .73$;	all tracks $\lvert\cos\theta\rvert \leq .94$; $p \geq .3$; $M_{ee} \geq .5$; at least 1 μ $\lvert\cos\theta\rvert \leq .73$;		all tracks $\lvert\cos\theta\rvert \leq .94$; $p \geq .3$; $M_{ee} \geq .5$;
Vermaseren	only 3 tracks $\lvert\cos\theta\rvert \leq .94$; $p \geq .3$; at least 1 μ $\lvert\cos\theta\rvert \leq .73$;	all tracks $\lvert\cos\theta\rvert \leq .94$; $p \geq .3$; at least 1 μ $\lvert\cos\theta\rvert \leq .73$;	only 3 tracks $\lvert\cos\theta\rvert \leq .96$; $p \geq .3$; at least 1 e $\lvert\cos\theta\rvert \leq .73$; $M_{ee} \geq .1$;	all tracks $\lvert\cos\theta\rvert \leq .96$; $p \geq .3$; at least 1 e $\lvert\cos\theta\rvert \leq .73$; $M_{ee} \geq .1$;
Kuroda		$\lvert\cos\theta_e\rvert \leq .95$; $\lvert\cos\theta_\mu\rvert \leq .95$; $p \geq .3$;		
Uniform Cuts	only 3 tracks $\lvert\cos\theta\rvert < .91$; $p \geq 1$; at least 1 μ $\lvert\cos\theta_\mu\rvert < .71$ $+p_\mu \geq 2.5$; $M_{ee} \geq 1$;	all tracks $\lvert\cos\theta\rvert < .91$; $p_e \geq .5$; at least 1 μ,e $\lvert\cos\theta_{\mu,e}\rvert < .71$ $+p_\mu \geq 2.5$; $M_{ee} \geq 1$;	only 3 tracks $\lvert\cos\theta\rvert < .91$; $p \geq 1$; at least 1 e $\lvert\cos\theta_e\rvert < .71$; $+p_e \geq 2.5$; $M_{ee} \geq 1$;	all tracks $\lvert\cos\theta\rvert < .91$; $p \geq 1$; at least 2 e $\lvert\cos\theta_e\rvert < .71$; $M_{ee} \geq 1$;

Table 4.1: Kinematic constraints and cuts applied to the Monte Carlo calculations. $M_{ee} = e^+e^-$ invariant mass in GeV/c^2, $p =$ momentum (GeV/c) of the particle.

of the cuts.

Table 4.2 and Table 4.3 list the cross sections for the four-lepton processes calculated by BDK program and Vermaseren program respectively. It should be noted that the BDK single-tag program requires the angle of the electron to be less than the angle of the positron, calculated results have to be suitably symmetrized. Thus, the listed cross section for the single-tag $e^+e^-\mu^+\mu^-$ events has been multiplied by a factor of 2. Also, the situation where both e^+e^- are at large opening angles and the missing track is a μ has not been properly taken into account. But such case are estimated to occur less than 3% of the time and, therefore, do not significantly affect the result.

The results of all the calculations show reasonable agreement. A direct com-

Cross Section(pb)	Multi-peripheral	Brems-strahlung	Anni-hilation	Con-version	Total
four-track $e^+e^-\mu^+\mu^-$	0.0203 $\pm$0.0004 (1137)	0.1633 $\pm$0.0013 (7763)	0.0087 $\pm$0.0002 (419)	0.0120 $\pm$0.0003 (632)	0.1831 $\pm$0.0013 (9951)
three-track $e^+e^-\mu^+\mu^-$	1.4615 $\pm$0.0119 (4716)	0.2938 $\pm$0.0066 (989)	0.0011 $\pm$0.0003 (2)	0.0040 $\pm$0.0004 (10)	1.7521 $\pm$0.0147 (5717)
four-track $e^+e^-e^+e^-$	0.02585 $\pm$0.0012 (293)	0.1365 $\pm$0.0018 (1689)	0.0027 $\pm$0.0003 (35)	0.0052 $\pm$0.0005 (75)	0.1497 $\pm$0.0022 (2092)

Table 4.2: Cross sections for the four-lepton processes calculated by the programs of Berend et al. The total cross section includes the interferences among all groups. Figures in parentheses are the number of unweighted events generated.

Cross Section(pb)	Multiperipheral	Bremsstrahlung	Total
four-track $e^+e^-\mu^+\mu^-$	0.0200 $\pm$.0004	0.1631 $\pm$.0010	0.1808 $\pm$.0016(30000)
three-track $e^+e^-\mu^+\mu^-$	1.4848 $\pm$.0255	0.3023 $\pm$.0105	1.7691 $\pm$.0090(30000)
four-track $e^+e^-e^+e^-$	0.0444 $\pm$.0002	0.1836 $\pm$.0004	0.2286 $\pm$.0006(10000)
three-track $e^+e^-e^+e^-$	2.9510 $\pm$.1101	0.7392 $\pm$.0292	3.7953 $\pm$.0581(20000)

Table 4.3: Cross sections for the four-lepton processes calculated by Vermaseren program. Figures in parentheses are numbers of events generated. The Bremsstrahlung result are actually the difference of the matrix elements square of the 6 diagrams and the the multiperipheral diagrams.

parison can be made between the Vermaseren and BDK results for the $e^+e^-\mu^+\mu^-$ events, since they are calculated under similar kinematic conditions. The agreement between the bremsstrahlung and multiperipheral groups are very good. To check the calculations of the conversion and annihilation groups for the four-track $e^+e^-\mu^+\mu^-$ events, the same kinematic selection requirements used in the BDK program are applied to Kuroda calculation. The cross section for this condition is 0.0193 pb, in reasonable agreement with the combined cross section (0.0207 pb) for the same groups calculated by BDK program. However, the combined cross section of Vermaseren and Kuroda, as well as the sum of individual cross sections calculated by BDK, is greater than the total cross section listed in Table 4.2 by roughly 15%. This is due to destructive interference between the multiperipheral and bremsstrahlung groups with the conversion and annihilation groups, which is not handled properly for the Vermaseren/Kuroda case. The effect of destructive interference is also apparent in the calculation for the four-track $e^+e^-e^+e^-$ events.

The total cross sections from the different programs are summarized in Table 4.4. Since the programs are written independently, their results provide a good check against errors in the computer programs; their consistency substantiates the reliability of the calculations. In the following sections, we describe the properties of the different groups based on the results of these calculations.

4.2 Properties of the Four-lepton Processes

As mentioned in Chapter 1, the Feynman diagrams for the four-lepton processes can be divided into multiperipheral, bremsstrahlung, annihilation and conversion groups. Each group has different kinematic characteristics and their contributions depend on the region of phase space covered by an experiment. Of course, what is actually measured is the sum of all the contributing diagrams and their mutual interference, and we actually can not precisely link a particular event to a particular group. But each group has different general characteristics so observed events can indicate the dominance of a particular group or the effect of interference among certain groups. Therefore, it is instructive to have a good idea of how each group behaves as a guide toward the understanding of the events observed in the

Type of events	Monte Carlo Program	Original σ (pb)	σ After uniform cuts(pb)
four-track $e^+e^-\mu^+\mu^-$	Berends et al.	0.1831 $\pm$0.0013	0.0733 $\pm$0.0008
	Vermaseren	0.1808 $\pm$0.0016	0.0723 $\pm$0.0010
	Kuroda	0.0750 $\pm$0.0003	0.0106 $\pm$0.0001
three-track $e^+e^-\mu^+\mu^-$	Berends et al.	1.7521 $\pm$0.0147	0.6549 $\pm$0.0090
	Vermaseren	1.7691 $\pm$0.0090	0.6635 $\pm$0.0055
four-track $e^+e^-e^+e^-$	Berends et al.	0.1497 $\pm$0.0022	0.0467 $\pm$0.0012
	Vermaseren	0.2286 $\pm$0.0006	0.0482 $\pm$0.0003
three-track $e^+e^-e^+e^-$	Vermaseren	3.7953 $\pm$0.0581	0.6718 $\pm$0.0244

Table 4.4: Summary of the total cross sections obtained from different programs.

experiment.

4.2.1 Multiperipheral group

In general, the multiperipheral group dominates. Its total cross section is of order 100 nb at $\sqrt{s} = 30$ GeV, while that for the bremsstrahlung group is two orders of magnitude smaller [32]. The main characteristic of this group is that both of the photons are in the t-channel. This gives the group a large production cross section for small values of the momentum transfer(Q^2). Both photons tend to align with the incident colliding electrons. Furthermore, in the $\gamma\gamma$ center-of-mass system the differential annihilation cross section looks like

$$\frac{d\sigma(\gamma\gamma \to l\bar{l})}{d\cos\theta} \simeq \frac{1+\cos^2\theta}{1-\cos^2\theta}, \tag{4.12}$$

and, thus, the lepton pair (l^+l^-) is strongly peaked along the photon direction. As a result, only small fraction of the total cross section is within the acceptance of a typical experiment. The above equation also specifies that the angular distribution of the produced lepton pairs should be symmetric in the forward-backward direction with respect to the incoming electron. The small opening angles of the outgoing e^+e^- make it very difficult to detect all the final state particles and usually only the produced lepton pair are observed. In this case, the visible cross section roughly increases with ln s. However, if one of the outgoing electrons in $e^+e^-\mu^+\mu^-$ events is required to be seen at some relatively large angle, the cross section will vary as $\frac{\ln s}{s}$, actually decreasing with increasing beam energies [24].

Figure 4.1 show the θ-angle distributions of the final state leptons for the four-track $e^+e^-\mu^+\mu^-$ process. The muon forward-backward symmetry and the tendency for the particles coming out at small angles are quite clear. Because the mass of the virtual photon increases with Q^2, requiring one or two of the outgoing electron detected at large angle will generally result in a lepton pair of large invariant mass. Figure 4.2 show the invariant mass distribution of the produced lepton pair for the cases where one or both of the electrons are above 20 degrees.

4.2.2 Bremsstrahlung group

Although the bremsstrahlung group is the second-most important group for four-lepton processes, its contribution to the cross section is usually much smaller than that of the multiperipheral group. The contribution from this group is significant only in those regions of phase space where the contribution from the multiperipheral group is very small, as is the case for the three-track and four-track $e^+e^-e^+e^-$, $e^+e^-\mu^+\mu^-$ events. Both the BDK and Vermaseren programs indicate that the contribution to the $e^+e^-\mu^+\mu^-$ visible total cross section from this group is about 15% if one requires 3 charged tracks within the acceptance of AMY detector. It is the dominant contributor (80 to 90% of the total cross section) of the four-track events (Table 4.2). The calculations for the $e^+e^-e^+e^-$ processes also display a similar relationship between the multiperipheral and bremsstrahlung groups (Table 4.3). Similar to the multiperipheral group, the outgoing e^+e^- from the bremsstrahlung group have small opening angle (Fig. 4.4) due to the its single photon exchange nature. Here the two-lepton system has charge parity $C = -1$ as opposed to the $C = +1$ of lepton pairs from the multiperipheral process. Because the leptons are pair produced by the virtual photon radiated from one of the incident elec-

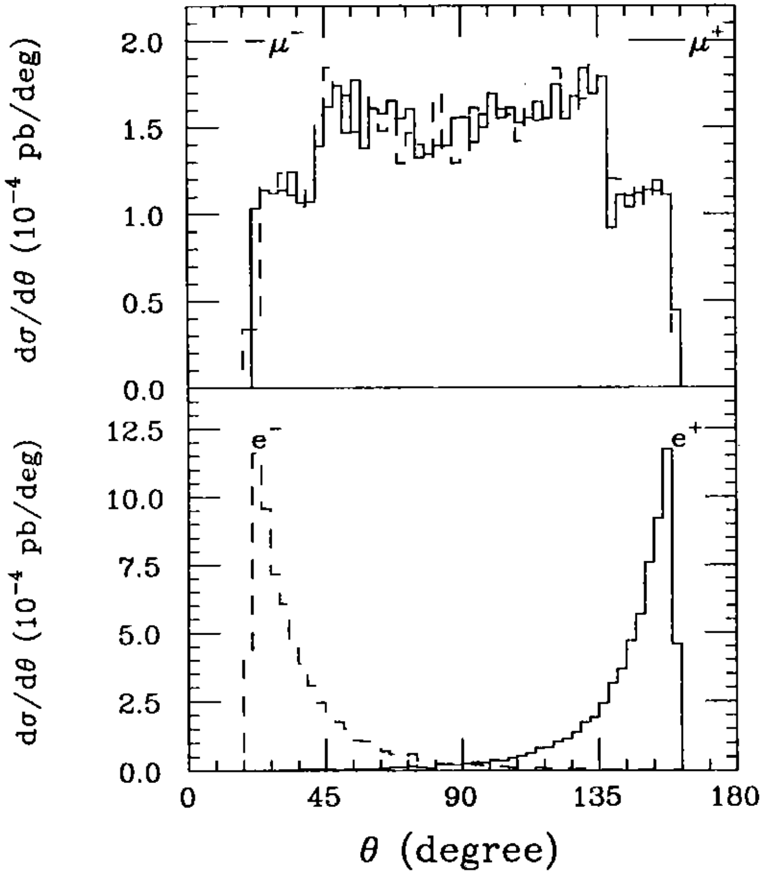

Figure 4.1: Distributions of the opening angles of the outgoing leptons from the multiperipheral group for the four-track $e^+e^-\mu^+\mu^-$ events. These results are determined using the Vermaseren program.

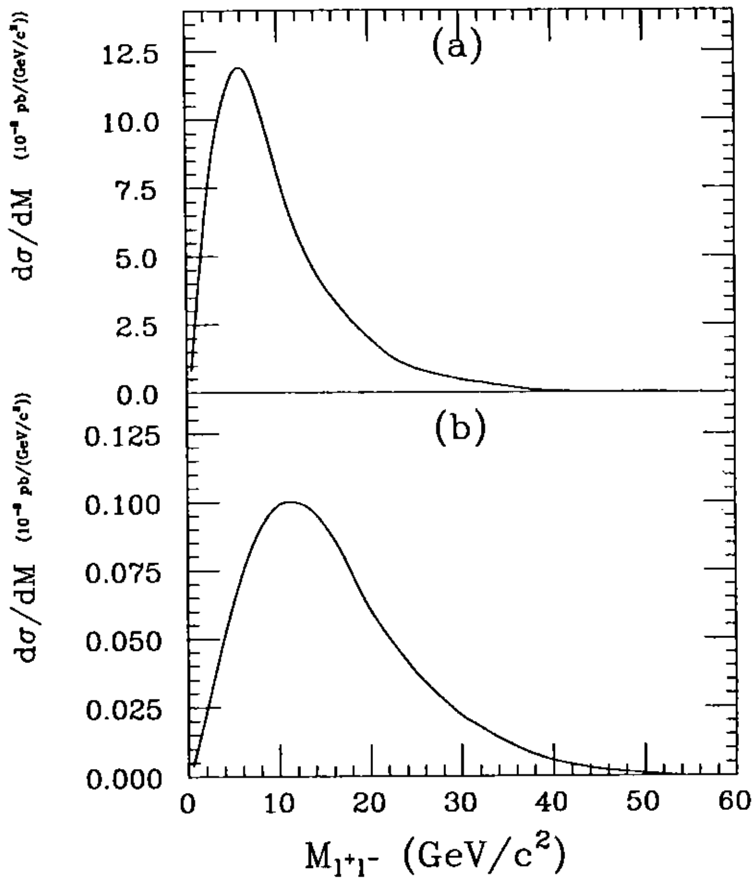

Figure 4.2: Invariant mass of the produced lepton pair for the three-track events where one electron is required to be $> 20°$ (a); and the four-track events where both electrons are $> 20°$ (b). These results are determined using the Vermaseren program.

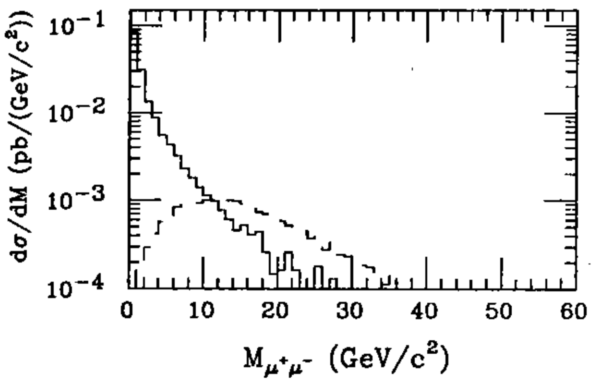

Figure 4.3: Comparison of $\mu^+\mu^-$ invariant mass distributions of the multiperipheral group (dashes line) and bremsstrahlung group (solid line) for the four-track $e^+e^-\mu^+\mu^-$ events. These results are determined using the Vermaseren program.

tron/positron lines, they tend to collimate with either the outgoing electron or positron and have a smaller invariant mass(M) distribution than those from the multiperipheral group. This is illustrated in Fig. 4.3 for the four-track $e^+e^-\mu^+\mu^-$ events.

Since the produced lepton pair should come from the electron or positron line with equal probability, the angular distribution of the leptons, though highly correlated, should be symmetric in the forward-backward direction Fig. 4.4.

4.2.3 Annihilation group

The annihilation group involves the exchange of a virtual photon in the s-channel between the incoming electron pair and the outgoing lepton pair, in contrast to the t-channel exchange of the bremsstrahlung group. For this reason, their θ-angle distributions are less peaked in the e^+e^- beam direction (Fig. 4.5), and the cross section varies as $\simeq 1/s$. However, because the produced leptons pair are created by the same mechanism, they have similar characteristics as those of the bremsstrahlung group.

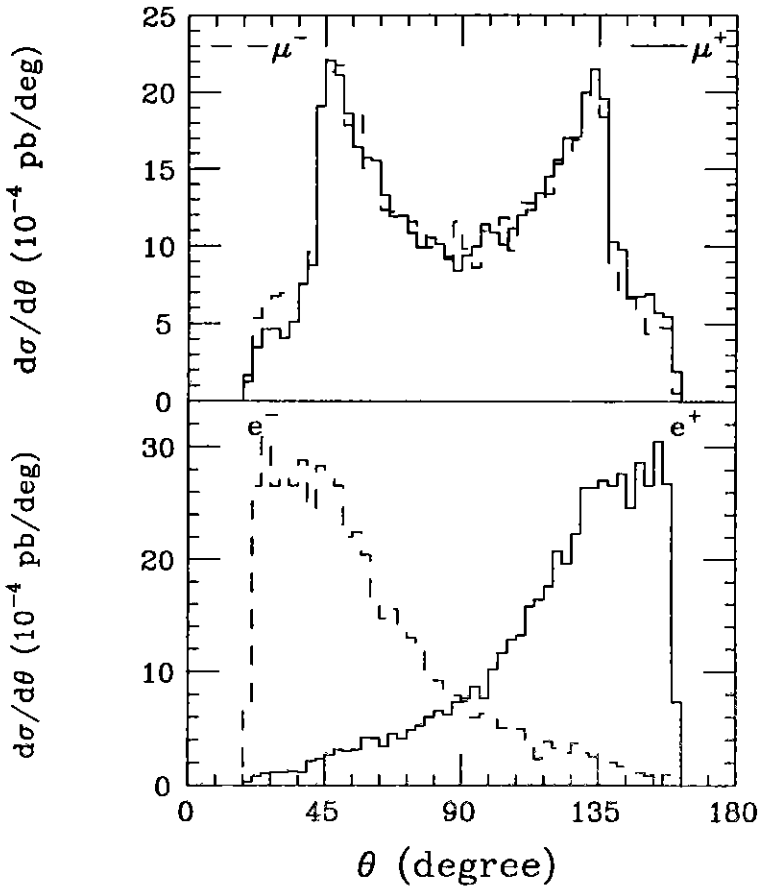

Figure 4.4: Distributions of the opening angles of the outgoing leptons from the bremsstrahlung group for the four-track $e^+e^-\mu^+\mu^-$ events. These results are determined using the Vermaseren program.

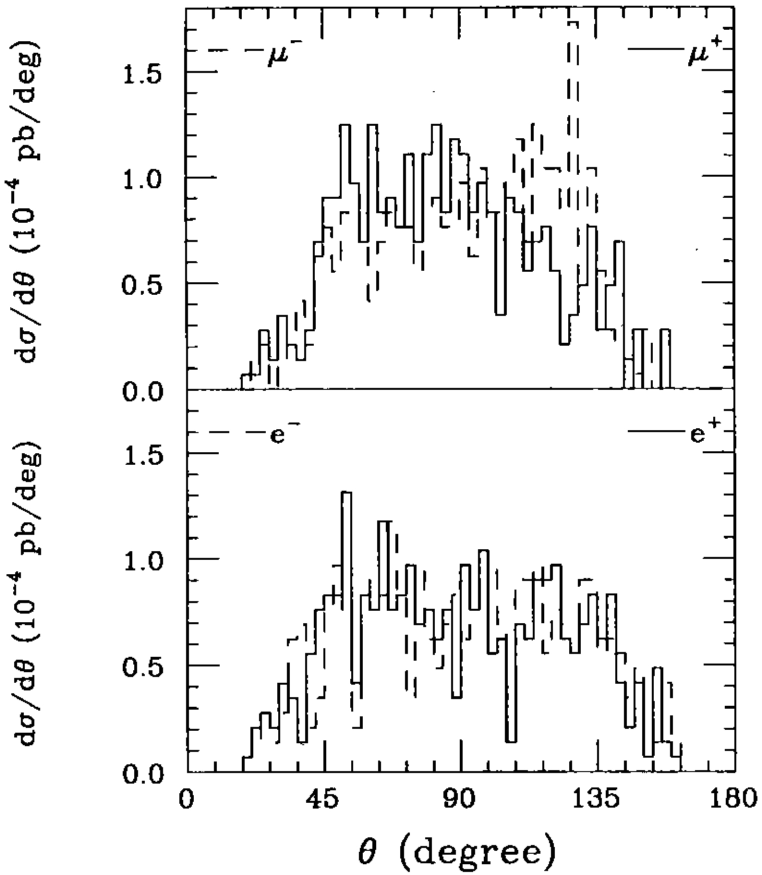

Figure 4.5: Distributions of the opening angles of the outgoing leptons from the annihilation group for the four-track $e^+e^-\mu^+\mu^-$ events. These results are determined using the double tagging program of Berend et al.

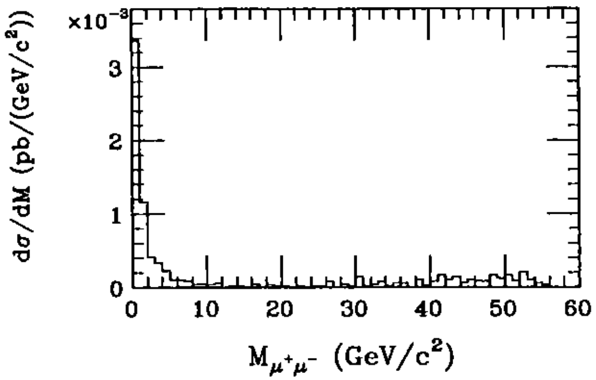

Figure 4.6: $\mu^+\mu^-$ invariant mass distribution of the annihilation group for the four-track $e^+e^-\mu^+\mu^-$ events. These results are determined using the double tagging program of Berend et al.

Putting all of these together, one can see that, even though the annihilation group contributes relatively little to the untagged events, it cannot be readily neglected in large-angle tagged events where the phase space is unfavorable for the multiperipheral and bremsstrahlung groups. The results in Table 4.2 indicate that, while its contribution to AMY's three-track events is still less than one percent, it is roughly one half that of the multiperipheral group for the four-track events. Another point worth noting is that since the outgoing leptons come from the same vertex, they can be either e^+e^-, $\mu^+\mu^-$, $\tau^+\tau^-$, or quark-antiquark pair. Thus, in addition to events of the type $e^+e^-e^+e^-$, $e^+e^-\mu^+\mu^-$, $e^+e^-\tau^+\tau^-$ and $e^+e^-q\bar{q}$, they can also produce events of the type $\mu^+\mu^-\mu^+\mu^-$, $\mu^+\mu^-\tau^+\tau^-$, etc. Because one of the vertices is associated with the photon originating from the annihilation of the incident e^+e^-, the invariant mass of the outgoing pair can be as large as $\sqrt{s}$. This results in a small bump around $M_{\mu^+\mu^-} = \sqrt{s}$ in the invariant mass distribution of the $\mu^+\mu^-$ pair(Fig. 4.6).

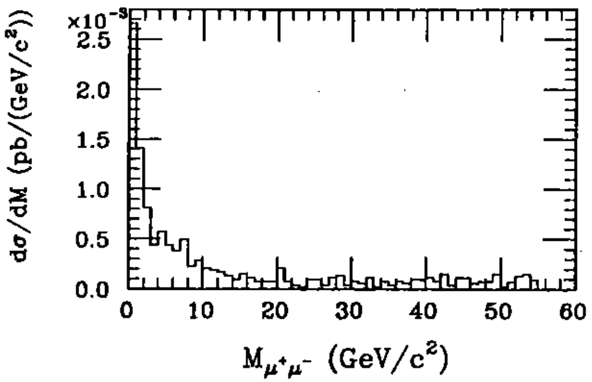

Figure 4.7: $\mu^+\mu^-$ invariant mass distribution of the conversion group for the four-track $e^+e^-\mu^+\mu^-$ events. These results are determined using the double tagging program of Berend et al.

4.2.4 Conversion group

The conversion group is characterized by the production of two time-like virtual photons, which can convert into any $e^+e^-, \mu^+\mu^-, \tau^+\tau^-$ and quarks pairs. This favors the production of low invariant mass leptons pair(Fig. 4.7). However, a peak also appears around $\sqrt{s}$ in the e^+e^- invariant mass distribution and, with a smaller magnitude, in the $\mu^+\mu^-$ distribution.

All the charged tracks are equally likely to go forward or backward relative to the e^- beam direction, and a sizable proportion have large opening angles (Fig. 4.8). Therefore, this group makes a nontrivial contribution to the large angular tagged events. Its contribution to the AMY three-track and four-track $e^+e^-\mu^+\mu^-$ event samples is roughly 1.5 to 3 times bigger than that of the annihilation group.

4.2.5 Summary

Referring to Fig. 4.9, the calculated differential cross sections for the three-track $e^+e^-\mu^+\mu^-$ events from the Vermaseren and BDK programs agree quite well over

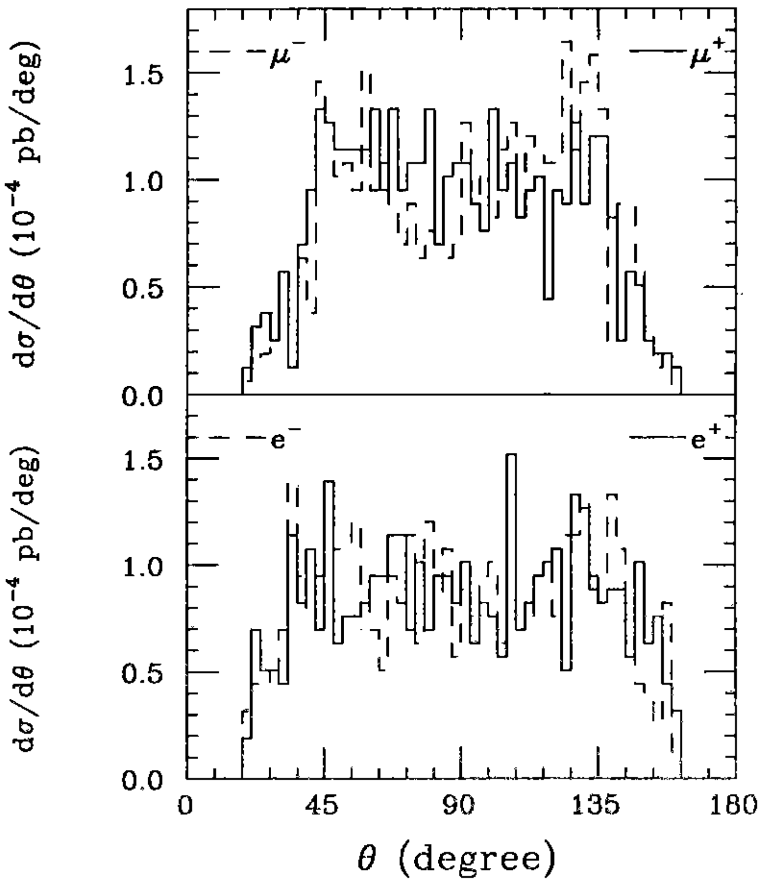

Figure 4.8: Distributions of the opening angles of the outgoing leptons from the conversion group for the four-track $e^+e^-\mu^+\mu^-$ events. These results are determined using the double tagging program of Berend et al.

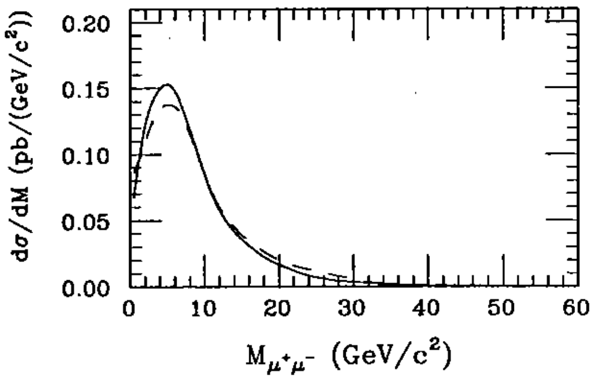

Figure 4.9: Comparison of $\mu^+\mu^-$ invariant mass distributions from Vermaseren (solid line) and BDK (dashed line) programs for three-track $e^+e^-\mu^+\mu^-$ events.

the entire range of $\mu^+\mu^-$ invariant mass. The differences between their resulting cross sections, listed in Table 4.4, is within the statistical error of the calculation.

Thus, it is reasonable to neglect the conversion and annihilation contributions in the study of three-track events. The multiperipheral group dominates, while the contribution from the bremsstrahlung group is small, but significant. In the case of the four-track events, bremsstrahlung becomes the dominant process and the multiperipheral's contribution reduces to the level of that from the conversion group.

Referring to Tables 4.2 and 4.3, one can see that the individual cross sections from the different contributing groups varies widely. For each set of kinematic requirements, the effect of the dominant group is almost an order of magnitude larger than that of the next most significant group. Thus, the interference between the different groups, which must be less than the geometric mean of their matrix elements, will be smaller than the cross section due to the dominant group alone. The total cross sections therefore are quite close to the algebraic sum of the individual contributions, as indicated in the tables. This also means that the kinematic distributions of the $e^+e^-e^+e^-$, $e^+e^-\mu^+\mu^-$ processes reflect mainly the characteristics of the dominant group of diagrams. Figure 4.10 shows the calculation of the differential cross section for the four-track $e^+e^-\mu^+\mu^-$ process with and without interference between groups included. The interference effects decrease the differential cross section, especially at region of low $\mu^+\mu^-$ invariant mass where the value is reduced by about 12%. However, the distribution still reflects the general characteristics of the bremsstrahlung group.

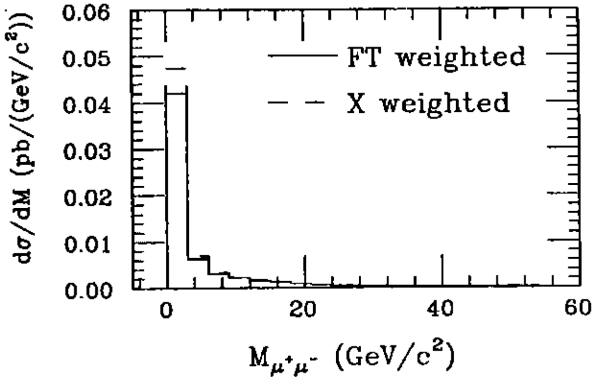

Figure 4.10: Comparison of the $\mu^+\mu^-$ invariant mass distributions with interference (FT weighted) and without interference (X weighted) for four-track $e^+e^-\mu^+\mu^-$ events. See text for the definitions of FT and X.

Due to opposite charge conjugation, the interference between the multiperipheral and the other groups may produce a charge asymmetry of the produced leptons [36] [27]. The charge asymmetry(A) for muon can be defined as:

$$A = \frac{N^{\mu^+}_{backward} + N^{\mu^-}_{forward} - N^{\mu^+}_{forward} - N^{\mu^-}_{backward}}{N^{\mu^+}_{backward} + N^{\mu^-}_{forward} + N^{\mu^+}_{forward} + N^{\mu^-}_{backward}}, \quad (4.13)$$

where N indicates the number of $\mu^\pm$ in the forward/backward hemisphere with respect to the electron beam. From the four-track $e^+e^-\mu^+\mu^-$ calculation, it is found to be statistically consistent with zero asymmetry($1.2 \pm 2.1\%$). For the three-track $e^+e^-\mu^+\mu^-$, the result from Vermaseren program gives an muon charge asymmetry of $4.5 \pm 1.0\%$. In the case of muon polar angle distribution regardless of charge, all the results show a symmetric distribution in the forward and backward direction.

Cross Section(pb)	Original	After selection cuts
four-track		
$e^+e^-\mu^+\mu^-$	0.1831±0.0013	0.0573±0.0007
$e^+e^-e^+e^-$	0.1497±0.0022	0.0402±0.0011*
three-track		
$e^+e^-\mu^+\mu^-$	1.7691±0.0090	0.4856±0.0047
$e^+e^-e^+e^-$	3.7953±0.0581	0.4638±0.0203

Table 4.5: List of the cross sections for the four-lepton processes. All the errors are statistical. * The four-track $e^+e^-e^+e^-$ cross section after the selection cuts is estimated assuming similar selection efficiency as the four-track $e^+e^-\mu^+\mu^-$ events.

4.3 Detector Simulation

To account for the finite resolution of the detector, a computer algorithm that simulates the various responses of the AMY detector is applied to events generated by the Vermaseren, BDK, and Kuroda programs. Because the analysis is primarily based on the reconstruction of charge tracks, a 'full simulation' is done only for the CDC and ITC components of the detector in order to economize the computing effort. Such 'simulated' events are then subjected to the same reconstruction and selection progress that are used for the actual data and discussed in Chapter 3, except in particle identification. To study the selection efficiency with the muon identification requirement, a sample of untagged $e^+e^-\mu^+\mu^-$ events observed in AMY detector are used [33]. The identification efficiency for muon tracks between 45° and 135° with $p > 3.0$ GeV/c is 85.6%. Since we typically have two muons in each event and require the positive identification of only one, the overall muon identification efficiency is 97%. The selection efficiency with electron identification on the shower counter is estimated to be very close to 100% and no correction is applied to the $e^+e^-e^+e^-$ cross sections.

The results of the selection cuts for the different processes are summarized in Table 4.5.

Chapter 5

Conclusion

5.1 Comparison of AMY data and theoretical calculation

The numbers of three-track and four-track $e^+e^- \rightarrow e^+e^-e^+e^-, e^+e^-\mu^+\mu^-$ events observed in AMY detector during the $\sqrt{s} = 50 - 61.4$ GeV runs are compared with the QED calculations, normalized to the same luminosity, in Table 5.1.

Except for the four-track $e^+e^-\mu^+\mu^-$, the observed number of events are in general agreement with the QED calculation.

Various kinematic distributions of the three-track events are shown in Figs. 5.1-5.2. The distributions are normalized to the number of events at the luminosity of 33.74 pb^{-1}. The observed events generally have large $\mu^+\mu^-$ or e^+e^- invariant masses and large particles transverse momenta in agreement with the QED calculation. The distributions of Q^2/s, which is defined as $p_e sin^2(\frac{\theta_e}{2})/E_{beam}$, also agree with the QED results. In the three-track $e^+e^-\mu^+\mu^-$ sample, while there is no clear

Event type	Observed by AMY	QED Calculation
three-track		
$e^+e^-\mu^+\mu^-$	16	16.4 ± 0.2
$e^+e^-e^+e^-$	16	15.6 ± 0.7
four-track		
$e^+e^-\mu^+\mu^-$	7	1.93 ± 0.02
$e^+e^-e^+e^-$	1	1.36 ± 0.04

Table 5.1: Number of events observed in AMY as compared with the QED calculation at integrated luminosity of 33.74 pb^{-1}.

muon charge asymmetry as defined in Chapter 4, there is some asymmetry on the polar angle distribution of muons, as opposed to the symmetric distribution expected from QED (Fig. 5.1.c). On the other hand, although the polar angle distributions of electron/positron display asymmetries similar to the QED distributions, there are more $e^-\mu^+\mu^-$ (10) events than $e^+\mu^+\mu^-$ (5) events. Nevertheless, all of these effects are within the limits of statistical uncertainty.

Fig. 5.3 shows the minimum e^+e^- invariant mass distribution for the 4-track $e^+e^-e^+e^-$ events, where we have included those events that failed the $M_{e^+e^-} \geq 1.0$ GeV/c^2 selection requirement; of the 16 events in the plot, 15 fail this requirement. Based on the photon conversion probability of 3% (c.f. Chapter 3) and the number of radiative Bhabha events observed in AMY [35], the expected background from the radiative Bhabha process is 12 events. The single remaining event with $M_{e^+e^-} \geq 1.0$ GeV/c^2 is consistent with the QED expectation of 1.36 events.

On the other hand, the disagreement between the QED calculations and the observed number four-track $e^+e^-\mu^+\mu^-$ events appears to be more than just a statistical fluctuation. Using Poisson statistics for the number of events involved, the probability that 7 events or more are observed when 1.9 are expected is 0.34%. The excess is concentrated at very low $\mu^+\mu^-$ invariant masses; 5 events have $M_{\mu\mu} \leq$ 1 GeV/c^2 (Fig. 5.4) where 0.73 events are expected. Other than the excess in rate, the general characteristics of the events are similar to that expected for ordinary QED four-lepton processes (Fig. 5.5.a-d); the scattered e^+, e^- display the polar angle asymmetry that is characteristic of the four-lepton processes (Fig. 5.6.a,b). However, the μ^+, μ^- exhibit a peculiar distribution in polar angles as shown in Fig. 5.7. Of the 14 observed $\mu^\pm$ tracks, only 1 is in the hemisphere of the incident e$^-$ beam direction, while 13 are in the opposite hemisphere. A better definition will be $A' = \frac{N_{forward}-N_{backward}}{N_{forward}+N_{backward}}$ which will give the asymmetry value $A' = -85.7 \pm 32.9\%$. Realizing that the muons come in low-mass pairs and thus are correlated in direction, one finds a probability that such an asymmetric distribution happens by statistical chance is at the 2% level.

The measured values of the kinematic variables of the particles for the four-

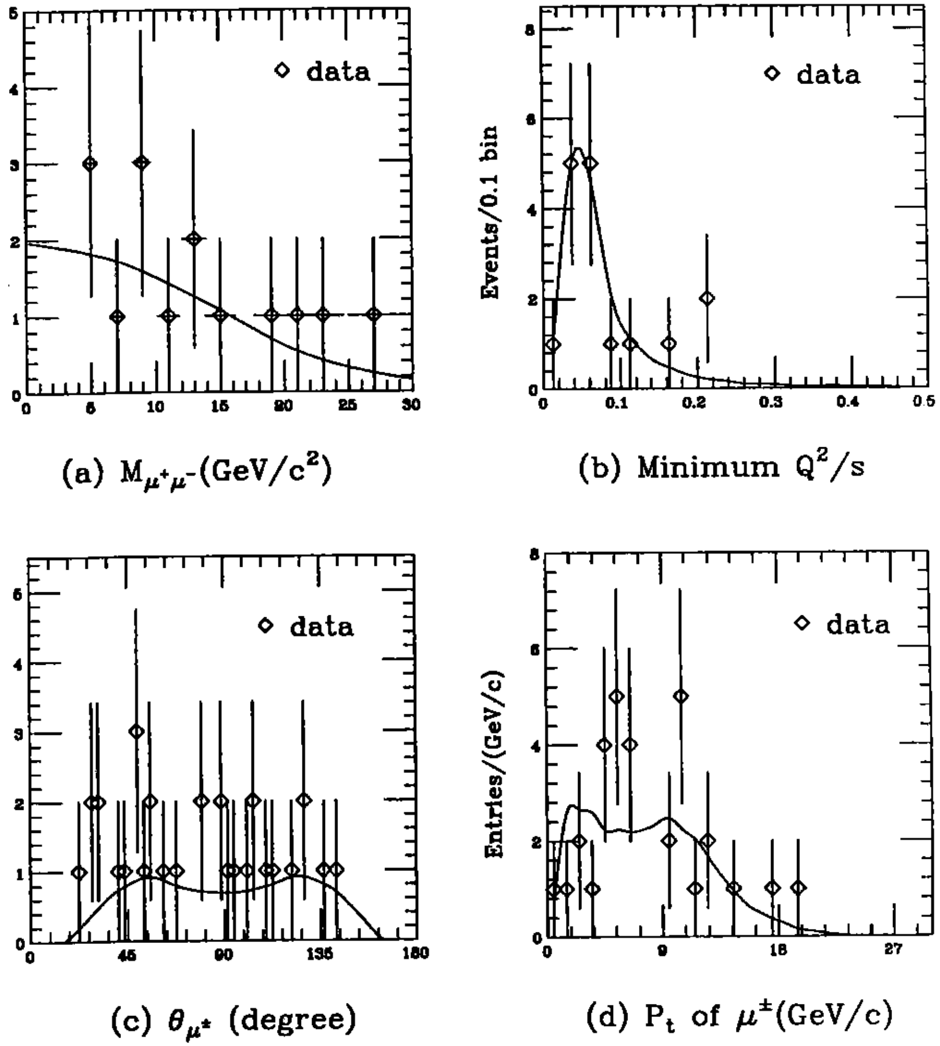

Figure 5.1: Kinematic Distributions of the three-track $e^+e^-\mu^+\mu^-$ events observed in AMY detector.

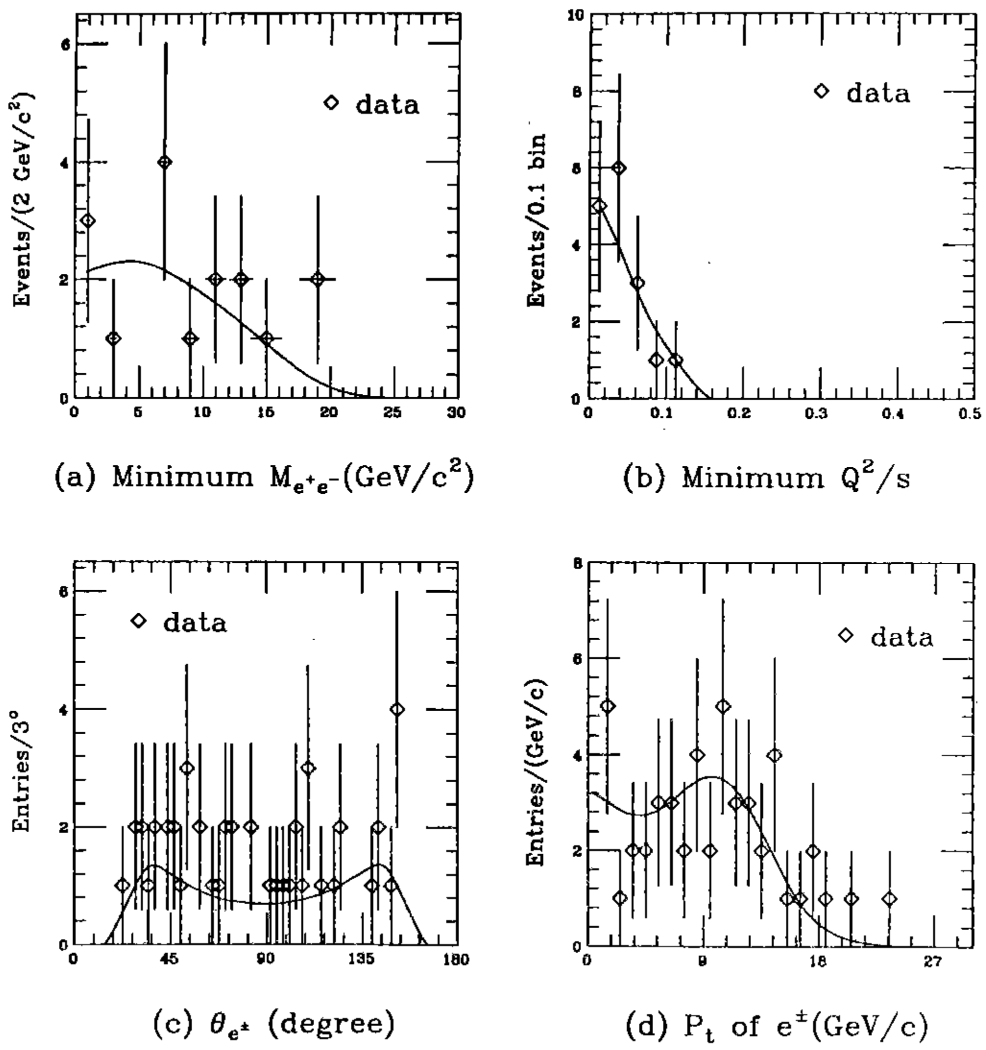

Figure 5.2: Kinematic Distributions of the three-track $e^+e^-e^+e^-$ events observed in AMY detector.

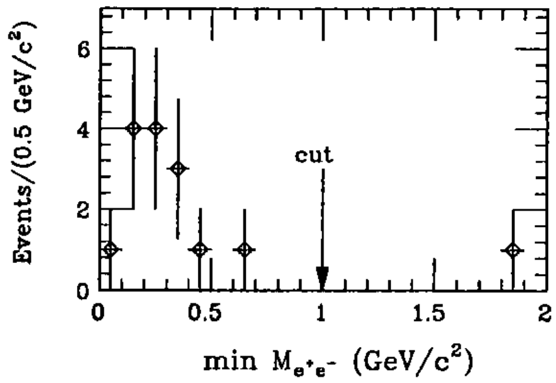

Figure 5.3: Minimum invariant mass of e^+e^- pair of the four-track $e^+e^-e^+e^-$ events observed in AMY detector.

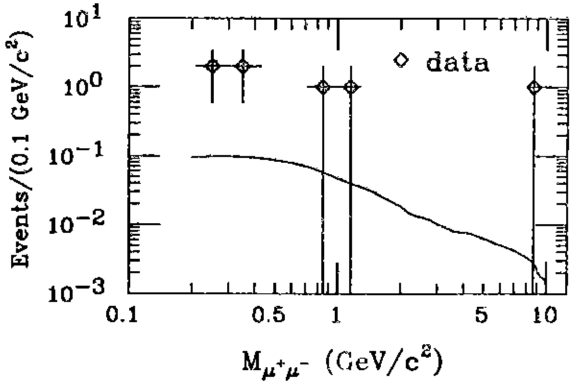

Figure 5.4: Invariant mass of $\mu^+\mu^-$ pair of the four-track $e^+e^-\mu^+\mu^-$ events observed in AMY detector. Both axes are in logarithm scale for better display at small invariant mass.

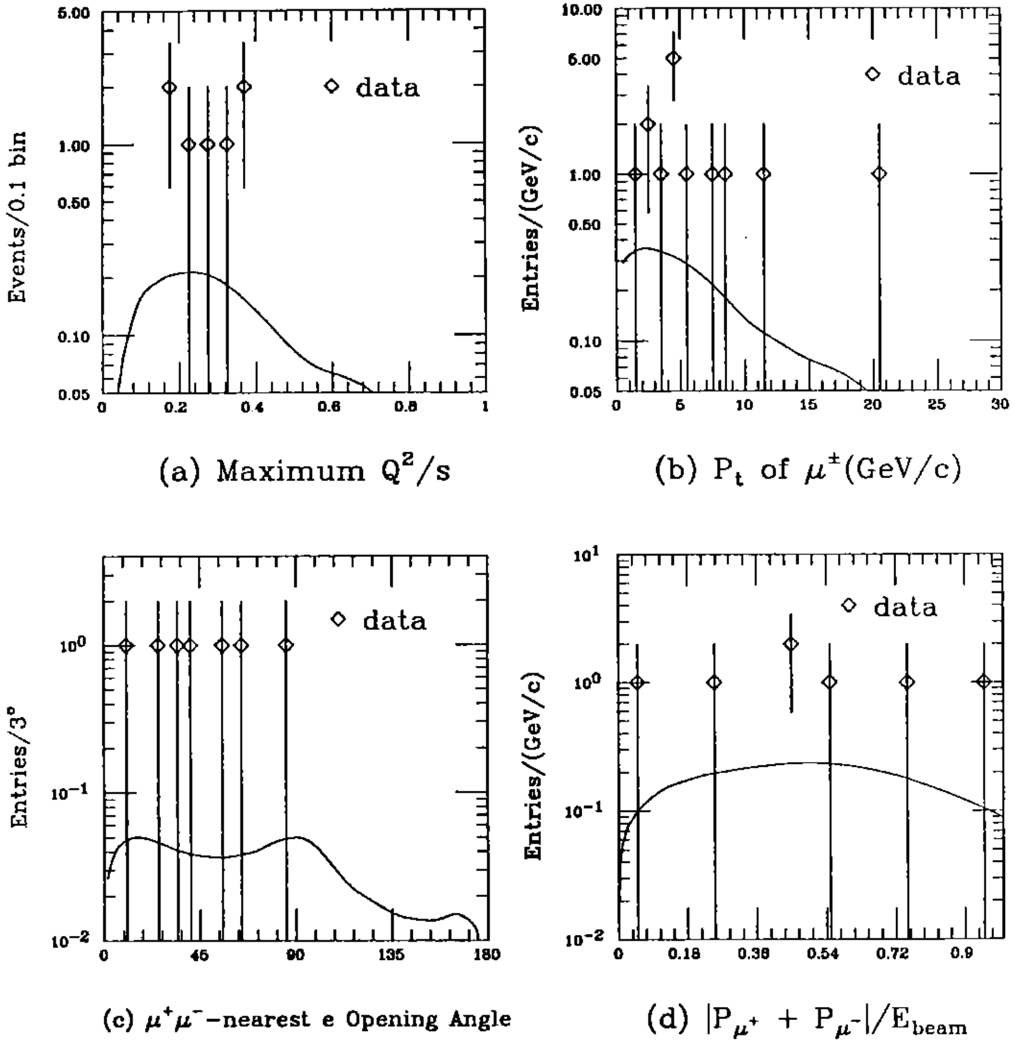

Figure 5.5: Kinematic Distributions of the four-track $e^+e^-\mu^+\mu^-$ events observed in AMY detector.The y-axis is in logarithm scale for better display of small values.

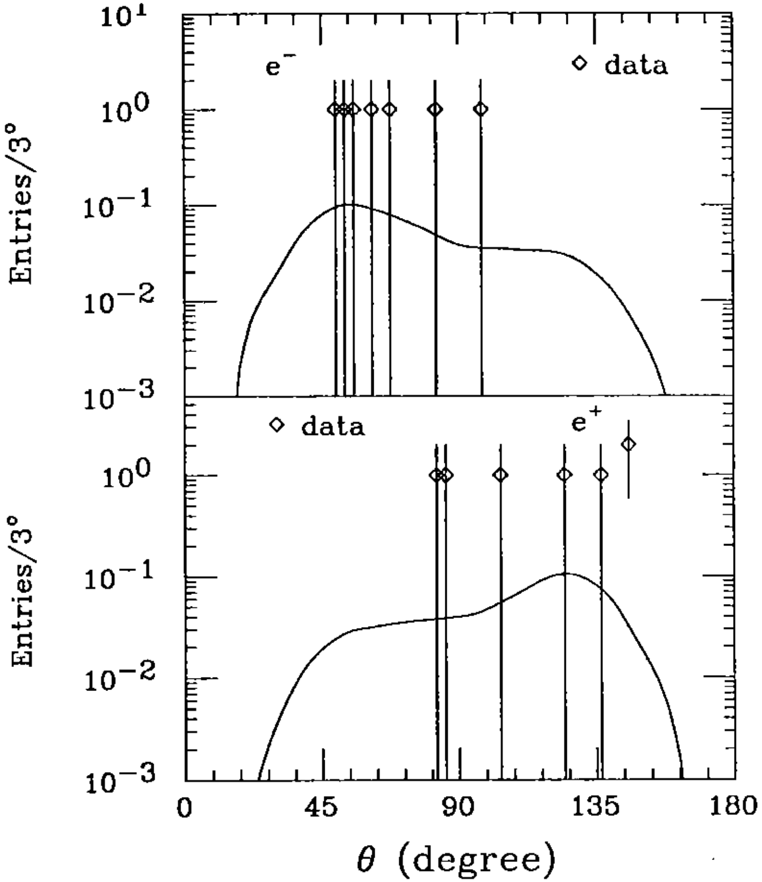

Figure 5.6: Electron polar angle distributions of the four-track $e^+e^-\mu^+\mu^-$ events.The y-axis is in logarithm scale for better display of small values.

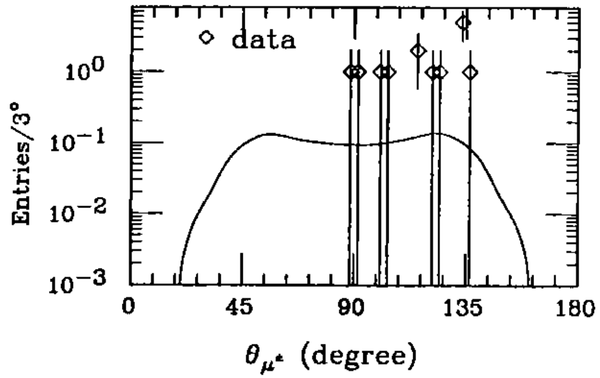

Figure 5.7: Polar angle of muon of the four-track $e^+e^-\mu^+\mu^-$ events. The y-axis is in logarithm scale for better display of small values.

track $e^+e^-\mu^+\mu^-$ events are listed in Table 5.2, and their kinematically fitted values are listed in Table 5.3. Computer generated graphic displays of these events are shown in Appendix A (Figs. A.4 to A.10).

5.2 Discussion

As pointed out in the previous chapter, the agreement among the results from the different programs, in addition to ruling out the probability of an error in the computing processes, strongly support the reliability of the QED calculation. The observed data for the three-track $e^+e^-e^+e^-$, $e^+e^-\mu^+\mu^-$ and four-track $e^+e^-e^+e^-$ samples show good agreement with QED. Only the four-track $e^+e^-\mu^+\mu^-$ data sample has a statistically significant deviation. As discussed in Chapter 3, the event selection criteria effectively reduced the total backgrounds for the three-track events to less than 5%, and to virtually zero for the four-track $e^+e^-\mu^+\mu^-$ events. One may dilute the statistical significance of the observed asymmetry by combining the four-track and three-track $e^+e^-\mu^+\mu^-$ data together. But the three-track and four-track events are each dominated by two distinct processes with opposite charge conjugation and this categorization is a natural one to use for this study.

Due to the AMY detector's compact size, the probability of misidentification due to the decays-in-flight of $\pi^\pm$ *and* $K^\pm$ mesons is only $\simeq 1.3\%/p(\mathrm{GeV/c})$ for π mesons and $\simeq 6\%/p(\mathrm{GeV/c})$ for K mesons. In light of the small number (~ 6) of tagged $e^+e^-h^+h^-$ events (h = hadron), *selected under less restrictive criteria*, the backgrounds due to meson misidentification cannot be significant. Moreover, 5 out of the 7 four-track $e^+e^-\mu^+\mu^-$ events have *both* muons positively identified. Thus, it is extremely unlikely that the observed excess is due to mesons decay-in-flight.

A possibility exists that the disagreement is due to the inaccurate evaluation of bremsstrahlung diagrams at small $\mu^+\mu^-$ invariant mass. One may check this by comparing to the observed number of $e^+e^- \to e^+e^-h^+h^-$ events, where we assume the hadrons to be pions. The bremsstrahlung cross sections for the $e^+e^-\mu^+\mu^-$ and $e^+e^- \to e^+e^-\pi^+\pi^-$ differ only in time-like photon exchange term, thus we can calculate the ratio(R) of $e^+e^-\mu^+\mu^-$ to $e^+e^-\pi^+\pi^-$ cross sections by comparing the $e^+e^- \to \mu^+\mu^-$ and $e^+e^- \to \pi^+\pi^-$ cross sections:

$$\begin{aligned} R &= \int \frac{w\sigma(e^+e^- \to \mu^+\mu^-)}{\sigma(e^+e^- \to \pi^+\pi^-)} ds \\ &= \int \frac{\beta^2}{6(1-\frac{\beta^2}{3})} |F_\pi(s)|^2 w ds \end{aligned} \tag{5.14}$$

EVENT	#	ID	p(GeV/c)	θ(deg)	ϕ(deg)	$M_{\mu^+\mu^-}$(GeV/c^2)
R2811 E1014	1	e^-	33.4	54.34	287.71	0.21
	2	μ^-	4.8	132.32	109.94	
$\sqrt{s} = 50$GeV	3	e^+	14.8	123.94	105.62	
	4	μ^+	7.0	132.25	109.96	
R3157 E630	1	e^+	6.6	136.98	10.79	0.87
	2	e^-	20.7	68.48	194.45	
$\sqrt{s} = 52$GeV	3	μ^+	7.7	98.86	15.98	
	4	μ^-	18.1	102.94	15.96	
R5024 E1996	1	e^-	33.7	48.12	208.39	0.32
	2	e^+	14.0	144.22	3.73	
$\sqrt{s} = 56$GeV	3	μ^-	8.9	116.78	43.39	
	4	μ^+	4.5	114.96	44.57	
R5042 E6832	1	e^-	25.8	55.11	120.93	1.22
	2	μ^-	3.0	125.64	293.18	
$\sqrt{s} = 56$GeV	3	μ^+	21.8	121.04	301.45	
	4	e^+	1.1	145.80	312.15	
R5675 E67	1	μ^+	8.7	137.29	241.99	0.37
	2	μ^-	3.1	134.16	242.85	
$\sqrt{s} = 56$GeV	3	e^+	19.8	104.89	186.57	
	4	e^-	18.4	61.04	23.18	
R6085 E2268	1	e^+	29.8	83.02	169.17	9.07
	2	e^-	34.6	98.36	346.89	
$\sqrt{s} = 60$GeV	3	μ^+	4.2	91.44	193.35	
	4	μ^-	5.0	87.90	31.10	
R7144 E4172	1	μ^+	5.7	134.07	355.44	0.28
	2	e^-	21.1	84.01	111.24	
$\sqrt{s} = 60.8$GeV	3	μ^-	1.9	133.71	358.99	
	4	e^+	26.5	87.36	278.71	

Table 5.2: Measured values of the kinematic variables for the four-track $e^+e^-\mu^+\mu^-$ events.

EVENT	#	ID	p(GeV/c)	θ(deg)	ϕ(deg)	Q^2(GeV^2)
R2811 E1014	1	e^-	25.0	52.78	287.49	493.1
$\sqrt{s} = 50$GeV	2	μ^-	4.7	132.20	109.96	
$\chi^2 = 41.1$	3	e^+	13.7	123.13	105.67	311.0
$M_{\mu^+\mu^-} = 0.21$GeV/c^2	4	μ^+	6.6	132.07	110.00	
R3157 E630	1	e^+	6.9	136.99	10.74	92.2
$\sqrt{s} = 52$GeV	2	e^-	25.5	68.99	194.79	851.0
$\chi^2 = 38.2$	3	μ^+	7.6	99.05	15.85	
$M_{\mu^+\mu^-} = 0.85$GeV/c^2	4	μ^-	12.0	103.98	15.74	
R5024 E1996	1	e^-	27.1	48.19	208.34	505.9
$\sqrt{s} = 56$GeV	2	e^+	14.3	144.26	3.76	151.1
$\chi^2 = 11.9$	3	μ^-	9.9	116.82	43.42	
$M_{\mu^+\mu^-} = 0.33$GeV/c^2	4	μ^+	4.6	115.01	44.59	
R5042 E6832	1	e^-	27.9	56.30	120.92	696.4
$\sqrt{s} = 56$GeV	2	μ^-	3.0	125.82	293.18	
$\chi^2 = 48.6$	3	μ^+	23.8	122.26	301.48	
$M_{\mu^+\mu^-} = 1.20$GeV/c^2	4	e^+	1.2	145.84	312.17	11.9
R5675 E67	1	μ^+	8.7	137.25	241.99	
$\sqrt{s} = 56$GeV	2	μ^-	3.1	134.14	242.85	
$\chi^2 = 38.2$	3	e^+	18.5	104.48	186.59	788.8
$M_{\mu^+\mu^-} = 0.37$GeV/c^2	4	e^-	26.8	60.74	23.15	781.6
R6085 E2268	1	e^+	25.3	82.60	169.35	1324.1
$\sqrt{s} = 60$GeV	2	e^-	25.9	97.41	346.61	1355.4
$\chi^2 = 38.6$	3	μ^+	4.3	91.27	193.37	
$M_{\mu^+\mu^-} = 8.62$GeV/c^2	4	μ^-	4.6	87.75	31.06	
R7144 E4172	1	μ^+	6.1	133.91	355.44	
$\sqrt{s} = 60.8$GeV	2	e^-	27.4	82.44	110.88	1446.5
$\chi^2 = 66.0$	3	μ^-	1.9	133.66	358.99	
$M_{\mu^+\mu^-} = 0.29$GeV/c^2	4	e^+	25.4	85.59	278.88	1424.2

Table 5.3: Fitted values of the kinematic variables for the four-track $e^+e^-\mu^+\mu^-$ events.

$$w = \int \frac{\frac{d\sigma(e^+e^-\to e^+e^-\mu^+\mu^-)}{dM_{\mu^+\mu^-}}}{\int \frac{d\sigma(e^+e^-\to e^+e^-\mu^+\mu^-)}{dM_{\mu^+\mu^-}} dM_{\mu^+\mu^-}} \delta(M_{\mu^+\mu^-} - \sqrt{s}) dM_{\mu^+\mu^-}; \quad (5.15)$$

where β = pion velocity $= \sqrt{1 - \frac{4m_\pi^2}{s}}$, and $F_\pi(s)$ is the pion form factor at center-of-mass energy(s). We restrict our comparison to the invariant mass ≤ 1 GeV/c^2, where the excess number of $\mu^+\mu^-$ events is found, and where the $\pi^+\pi^-$ system is dominated by the well known ρ(770 MeV) meson. Using the pion form factor as parameterized by Gounaris and Sakurai [36] in the integration, we evaluate R over the $s = 0 - 1$ GeV^2 region to be $R = 1.41$, which indicates that more $e^+e^-\pi^+\pi^-$ events are expected in the low mass region than $e^+e^-\mu^+\mu^-$ events. A similar comparison can be done in the case that the hadrons are kaons. Here, however, the ϕ(1020 MeV) meson resonance, which dominates kaon production, has a very narrow width (4.22 MeV), and does not make a significant contribution to the $e^+e^-h^+h^-$ cross section. Using the $e^+e^-\mu^+\mu^-$ selection requirements with the muon identification reversed, we find no four-track $e^+e^-h^+h^-$ event candidates, consistent with the QED prediction.

Similar analyses have been done by other e^+e^- collider experiments in Petra [4] and PEP. However, those studies had either a minimum $\mu^+\mu^-$-invariant mass requirement of $M_{\mu\mu} \geq 1$ GeV/c^2 [37],[38] or a minimum track-to-track angle requirement of 10 degrees [39]. Table 5.2 summarized the recent results from the Petra and PEP experiments and AMY data under similar cuts. In the Cello analysis [37], the four-track (double-tag) events are categorized according to where the tagging electrons were observed by the detector which has a angular coverage down to 150 mrad. The category closest to the cuts adopted for this AMY study are the CYCY events which required all charge tracks within $|\cos\theta| < 0.92$ and at least two of them satisfying $|\cos\theta| < 0.85$. This gives them 8 events between $\sqrt{s} = 35 - 46.8$GeV at integrated luminosity of 130 pb^{-1}, in agreement with QED expectation of 10 events. In the recent analysis on the PEP experiments [38], both Mark II and HRS data are shown to agree with QED calculation at the region where the minimum invariant mass of any opposite charge pairs is greater than 1.0 GeV/c^2. Although both the Mark II data and HRS data are shown before the invariant mass cut is applied, they are the combination of both $e^+e^-e^+e^-$

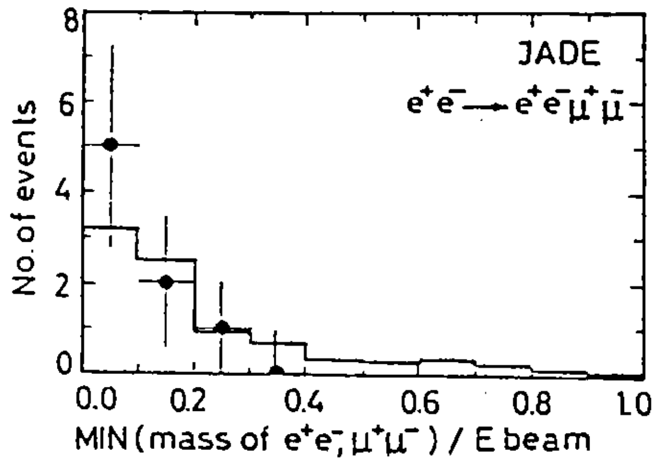

Figure 5.8: The smaller of the e^+e^- or $\mu^+\mu^-$ invariant mass for the reaction $e^+e^- \to e^+e^-\mu^+\mu^-$ from the publication of JADE experiment.

and $e^+e^-\mu^+\mu^-$ events and any excess in $\mu^+\mu^-$ invariant mass cannot be readily observed. Instead of the minimum invariant mass requirement, a 10 degrees track-to-track angle cuts is used in the JADE double-tag analysis [39] and the result is in general agreement with QED expectations. But within statistical uncertainty, there is an excess in the lowest bin of minimum e^+e^-, $\mu^+\mu^-$ invariant mass/E$_{beam}$ distribution (Fig. 5.8) for the $e^+e^-\mu^+\mu^-$ events. Furthermore, the muon angular distribution (Fig. 5.9) also suggests an asymmetry similar to the one observed in AMY. If a similar $M_{\mu^+\mu^-} \geq 1$ GeV/c^2 invariant mass cut is applied to the AMY data, only 2 events survive, consistent with the QED expectation of 1.17 ± 0.02 events. Also, if we use a minimum track-to-track opening angle requirement of 10°, 1 event survives compared with the QED expectation of 1.24 ± 0.02 events. However, there is no particular reason to apply such cuts; unlike the case for the $e^+e^-e^+e^-$, there is no special background and the detector has no particular problem detecting such low mass pairs. In addition, the QED calculations are unambiguous for low $\mu^+\mu^-$ mass values.

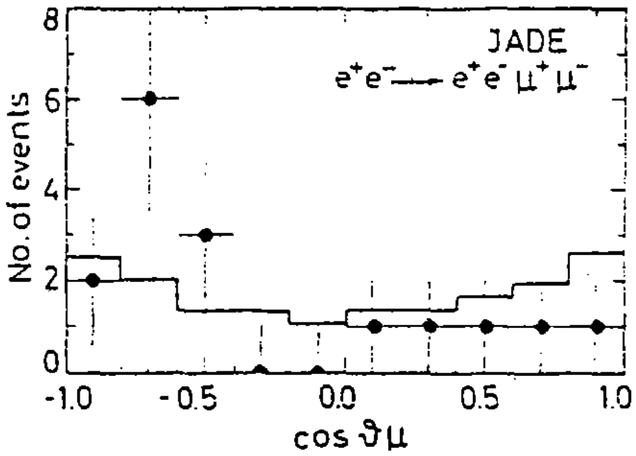

Figure 5.9: The polar angle distribution of the muons in $e^+e^-\mu^+\mu^-$ final state from the publication of JADE experiment.

Experiment	AMY	Cello	Mark II	HRS	JADE
$\sqrt{s}$ (GeV)	50-61.4	35-46.8	29	29	28.8-46.8
$\int Ldt$ (pb^{-1})	33.7	130	205	290.7	95
$\lvert\cos\theta\rvert$	all tracks $< .91$, at least 2 $< .71$	all tracks $< .92$, at least 2 $< .85$	all tracks $< .94$, at least 2 $< .71$	all tracks $< .91$	all tracks $< .97$
$M_{\mu^+\mu^-} \geq 1$ GeV/c^2	2	8	10	24	
$\geq 10°$ tracks sep.	1				8

Table 5.4: Number of four-track $e^+e^-\mu^+\mu^-$ events observed in AMY, Cello, Mark II, HRS and JADE experiments under similar cuts on $\mu^+\mu^-$ pair.

EVENT	#	ID	p(GeV/c)	θ(deg)	ϕ(deg)	Q^2(GeV^2)
R4625 E1192	1	e^+	14.3	103.32	270.06	615.3
$\sqrt{s}$ = 56GeV	2	μ^-	13.8	38.69	8.00	
$\chi^2 = 70.9$	3	μ^+	6.3	37.62	5.38	
$M_{\mu^+\mu^-}$ = 0.39GeV/c^2	4	e^-	21.5	125.6	135.26	503.9
R5644 E694	1	e^+	27.20	123.58	249.96	692.8
$\sqrt{s}$ = 57GeV	2	e^-	14.63	79.35	79.61	679.9
$\chi^2 = 4.1$	3	μ^-	4.86	35.17	52.76	
$M_{\mu^+\mu^-}$ = 0.27GeV/c^2	4	μ^+	10.31	35.73	54.71	

Table 5.5: Fitted values of the kinematic variables for the additional four-track $e^+e^-\mu^+\mu^-$ candidates.

5.2.1 The Possibility of a New Particle

In addition to the seven four-tracks events, there are two more events (Figs. A.11, A.12) that passed all the selection criteria except that both of the minimum ionizing particles are lying outside the MUO coverage and cannot be positively identified. However, the tracks clearly register as minimum ionizing in the endcap detector. There is no possibility that they could be electrons. Their kinematics are listed in Table 5.5. If we relax our angular acceptance for positively identified muon to $|\cos\theta| \leq 0.82$ to include these two events and assume the minimum ionizing particles to be muons, we have in total 9 events while the QED only expected 2.1 events. Their $M_{\mu^+\mu^-}$ distribution in figure 5.10 shows that 6 of the events are below 400MeV. A gaussian fit to these six events centers at 322MeV with an rms width of 60MeV.

A Monte Carlo study on the invariant mass resolution of two close tracks as reconstructed by the CDC tracking algorithm was performed. The invariant mass obtained from the original generator-level information is compared with the reconstructed mass value obtained from applying our reconstruction program on the simulated detector response. The results are plotted in Fig. 5.11 as mass resolution vs invariant mass. The mass resolution is roughly constant at about 50MeV for $\mu^+\mu^-$ masses below 1 GeV/c^2 and gradually increases to 230MeV for $\mu^+\mu^-$ masses of 9.5 GeV/c^2. Thus, it is within the capability of AMY detector to differentiate the mass on a reasonably fine scale in the low mass region.

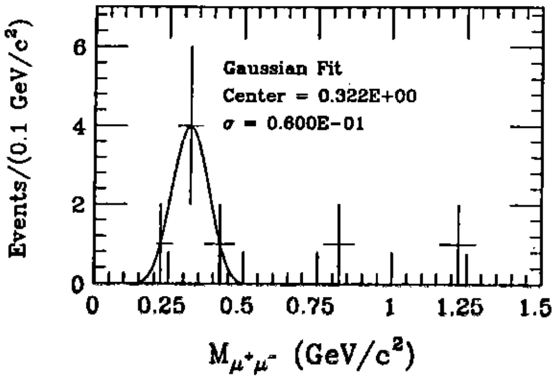

Figure 5.10: Detailed display of the invariant mass of $\mu^+\mu^-$ pair of the four-track $e^+e^-\mu^+\mu^-$ events with the addition of the two possible candidates. See text.

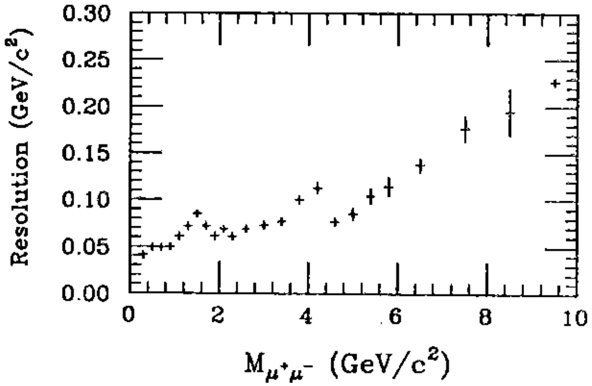

Figure 5.11: Plot of the $M_{\mu^+\mu^-}$ resolution vs $M_{\mu^+\mu^-}$ based on the study of the simulated four-track $e^+e^-\mu^+\mu^-$ events.

A plausible explanation of the excess events in the low mass region is the existence of a new particle with mass about 322 MeV/c^2, that has not yet been observed by other experiments. We have discussed previously that all previous experimental studies of high Q^2 4-lepton events required $M_{\mu^+\mu^-} \geq 1$ GeV/c^2 or track-to track separations of 10°. The existence of any resonance below 1 GeV/c^2 produced in these reactions would go undetected.

However, it would be remarkable for such a resonance to go undetected in other processes. One possibility would be if this particle had the quantum numbers $J^C = 1^+$. A $C = +1$ particle is not produced in single-photon annihilation processes and Yang's theorem prevents a spin 1 particle from coupling to two real photons. In two-photon studies are based on the untagged events, where both of the interacting photons tend to be almost real, the production of such states would be hidden by more prominent hadronic resonances.

On the other hand, the coupling of $J^C = 1^+$ particle to two-photons would increase as either or both of the photons become more virtual as is the case in the present analysis. All of the double-tag events are characterized by very high Q^2 values : the maximum Q^2 ranges from 493.1 to 1446.5, with an average at 827.2 GeV^2 (see tables 5.3 and 5.5). If all the excess events are indeed produced by the two-photon processes, both photons in the system will be highly virtual and the production of a $J^C = 1^+$ state may be possible. We hope to confirm such an effect in future Tristan runs and from detailed analyses of other e^+e^- collider experiments.

Appendix A

Displays of Four-lepton Events

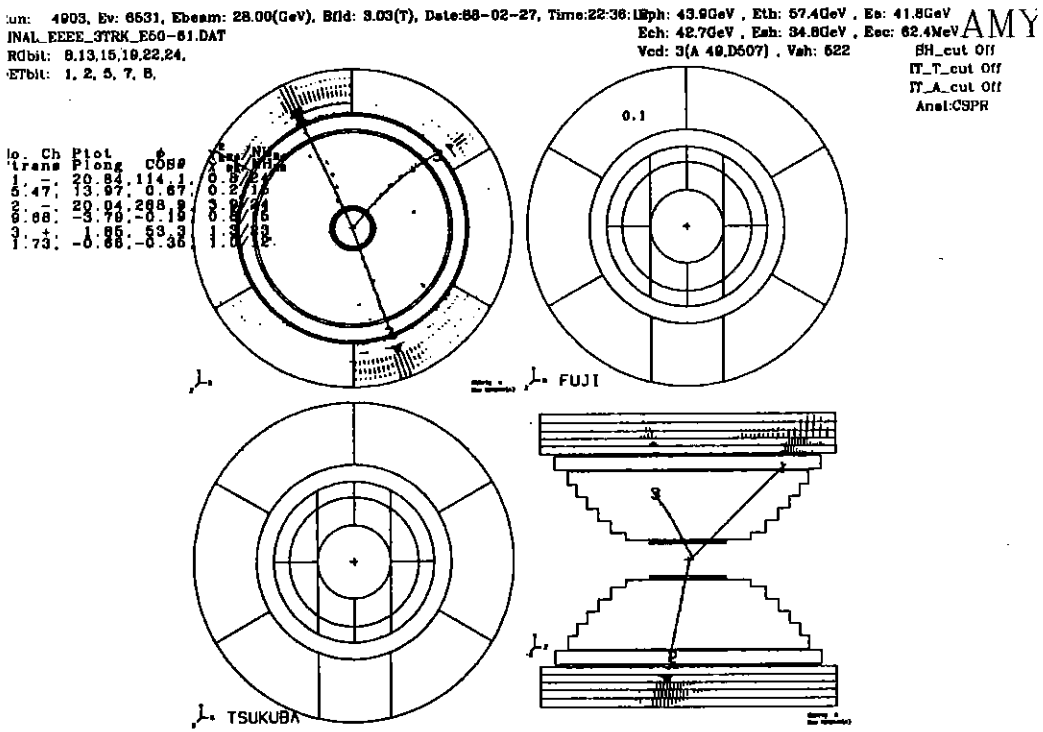

Figure A.1: Example of a three-track $e^+e^-e^+e^-$ event.

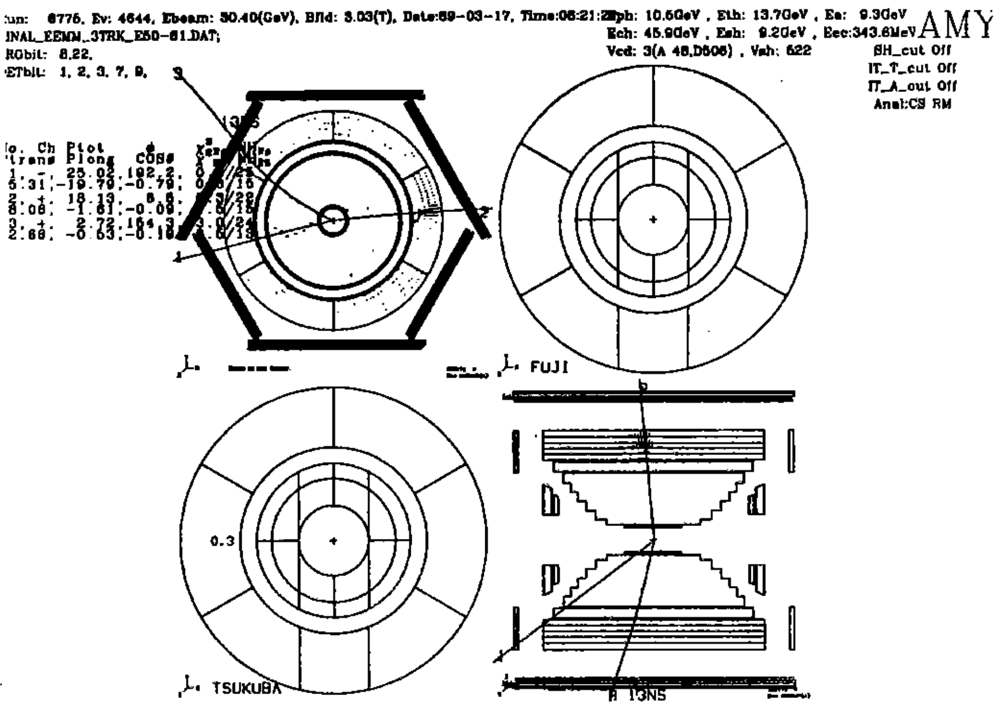

Figure A.2: Example of a three-track $e^+e^-\mu^+\mu^-$ event.

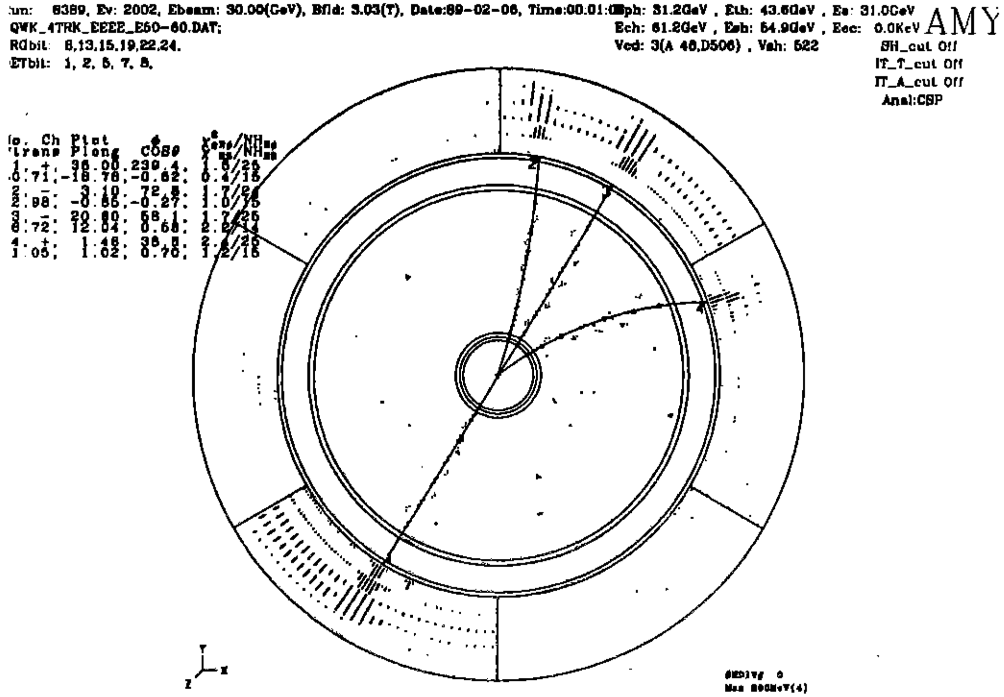

Figure A.3: Example of a four-track $e^+e^-e^+e^-$ event.

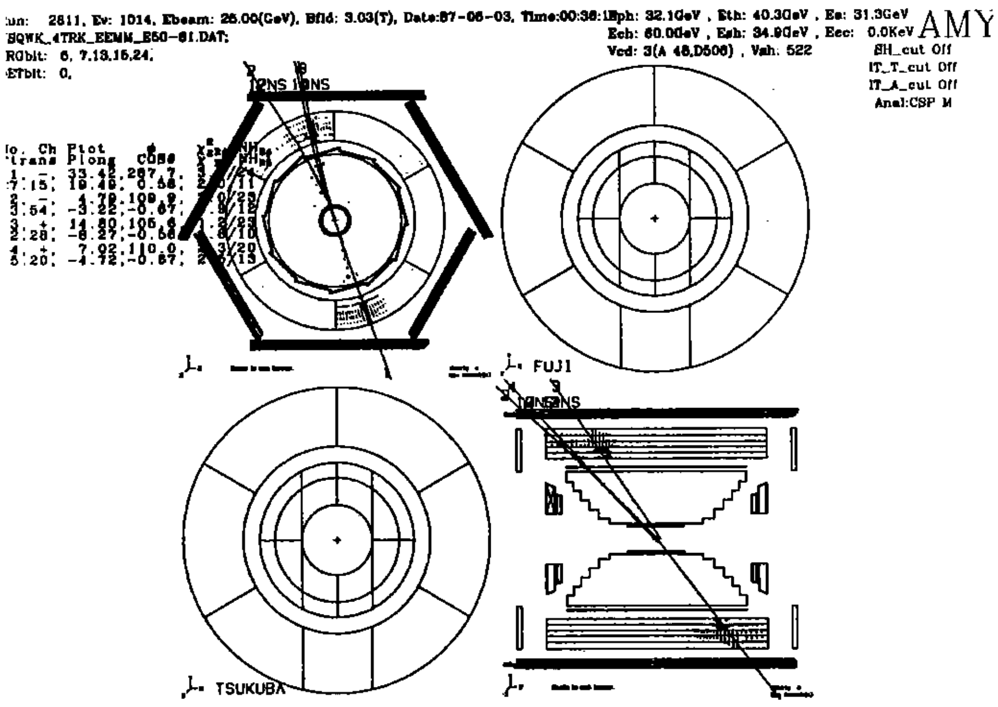

Figure A.4: Four-track $e^+e^-\mu^+\mu^-$ event.

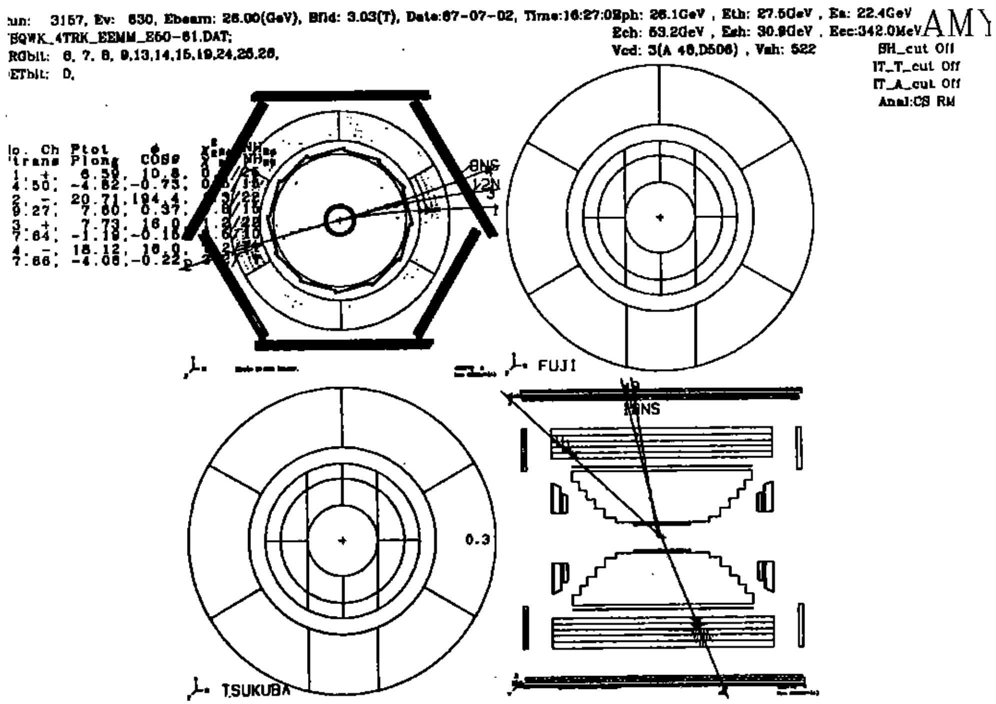

Figure A.5: Four-track $e^+e^-\mu^+\mu^-$ event.

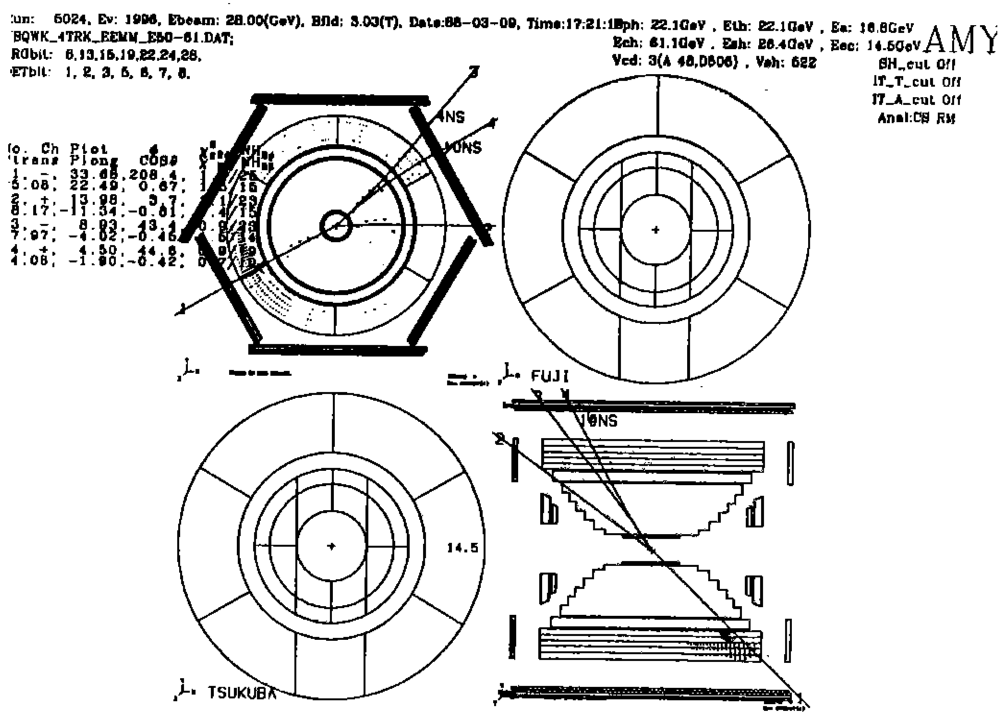

Figure A.6: Four-track $e^+e^-\mu^+\mu^-$ event.

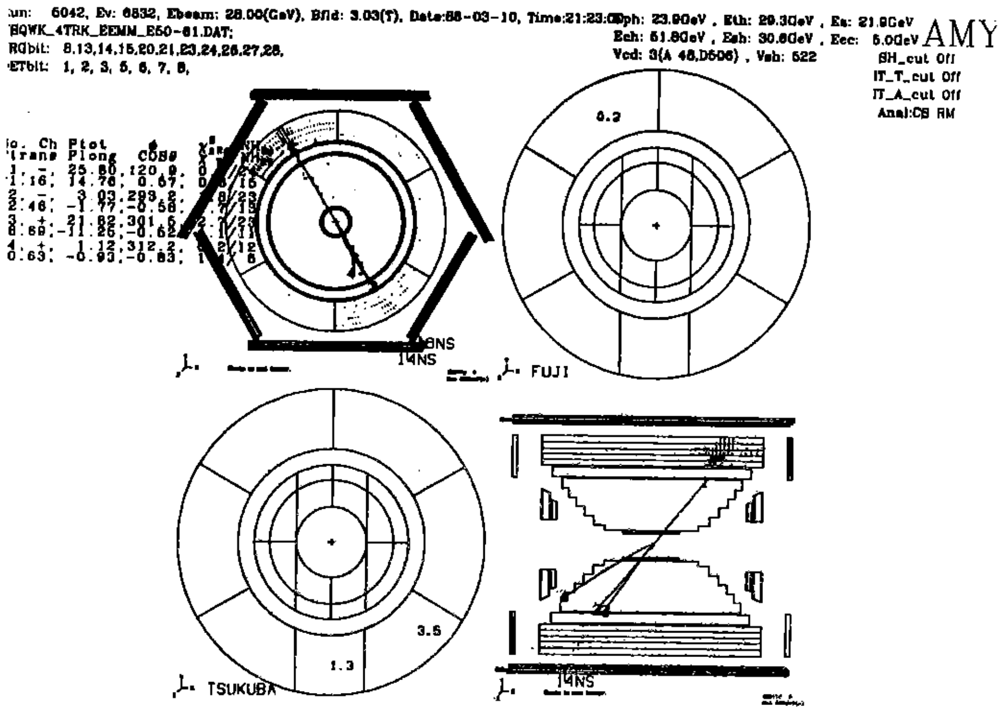

Figure A.7: Four-track $e^+e^-\mu^+\mu^-$ event.

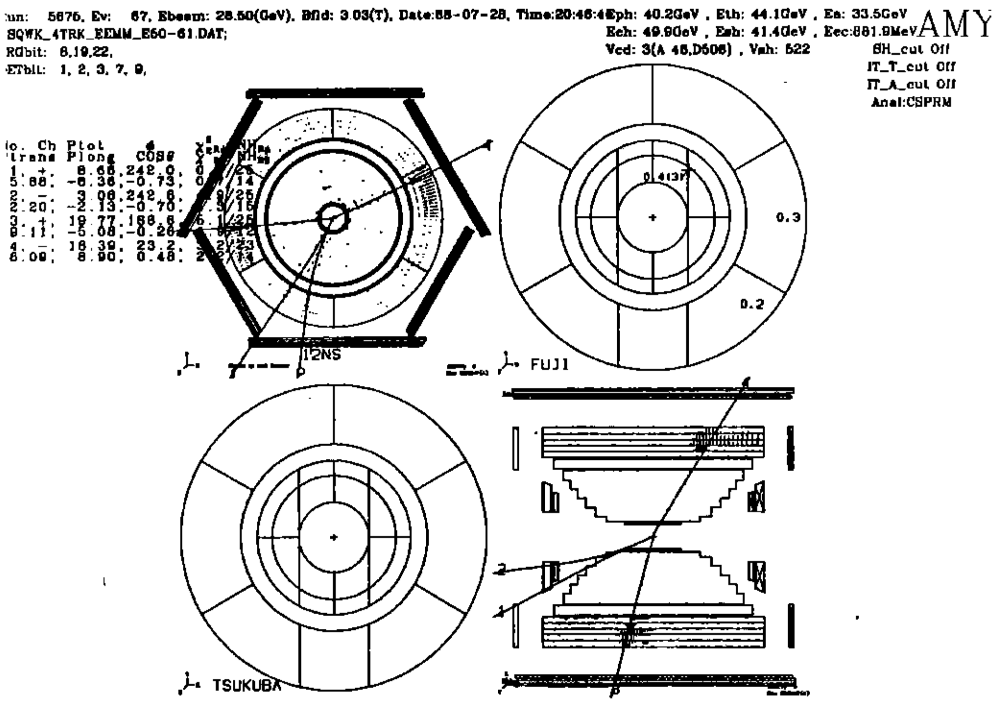

Figure A.8: Four-track $e^+e^-\mu^+\mu^-$ event.

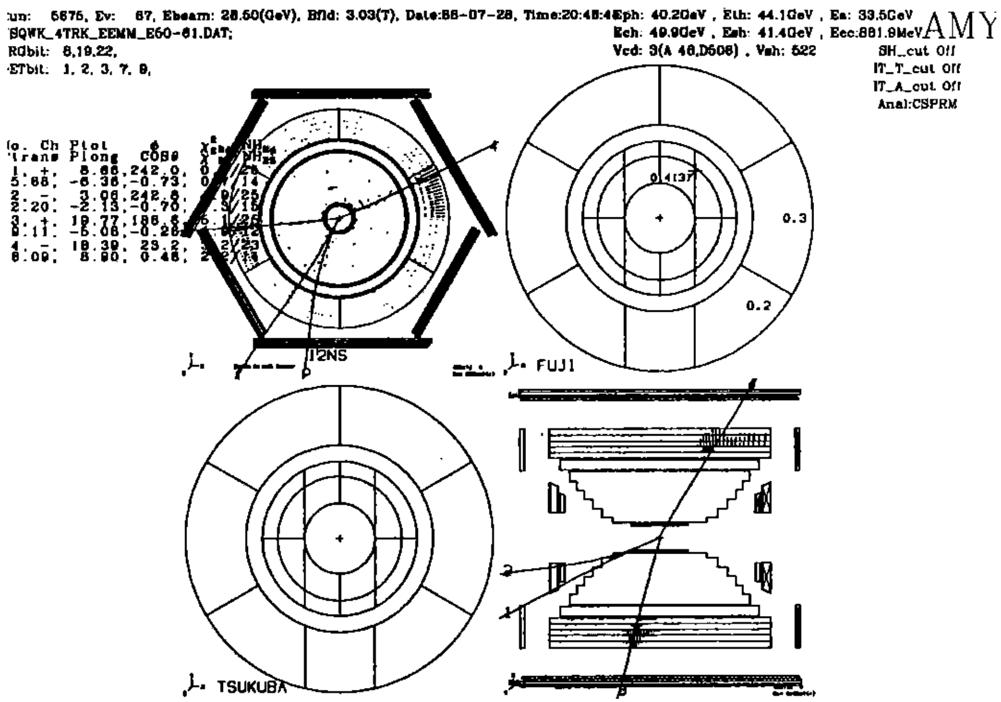

Figure A.9: Four-track $e^+e^-\mu^+\mu^-$ event.

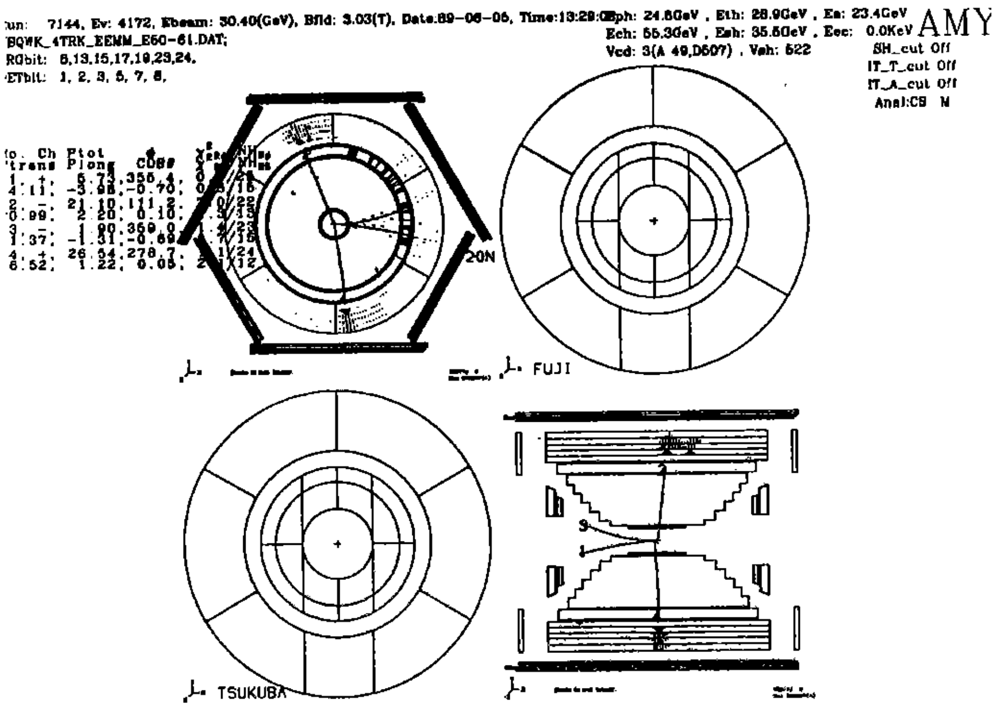

Figure A.10: Four-track $e^+e^-\mu^+\mu^-$ event.

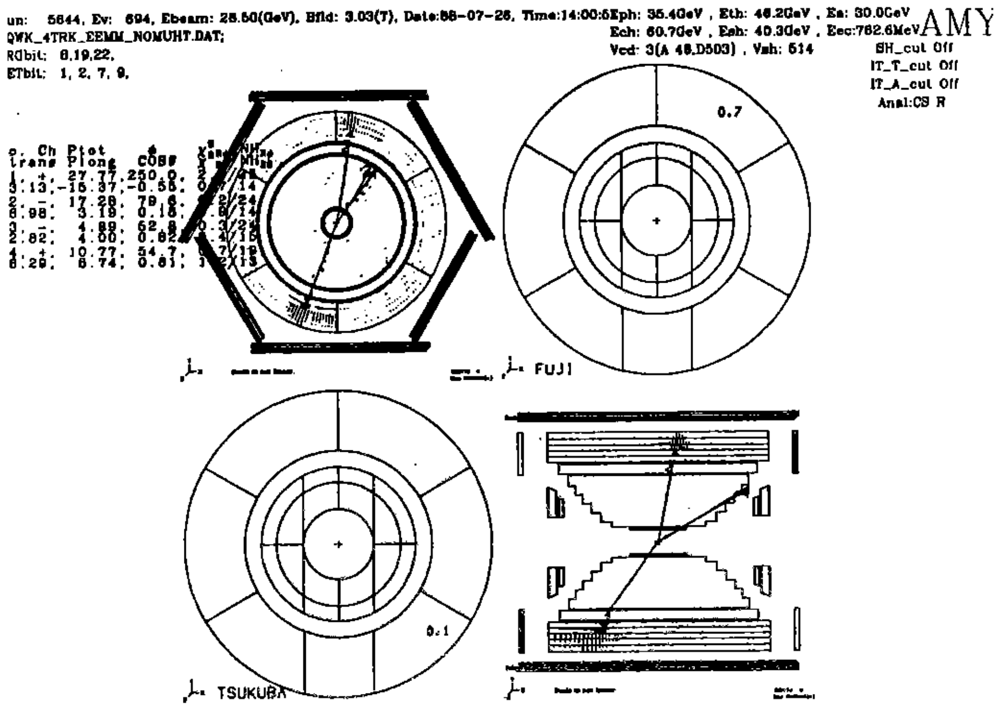

Figure A.11: Possible four-track $e^+e^-\mu^+\mu^-$ event. Energies on the RSC are compatible to those deposited by minimum ionizing particles.

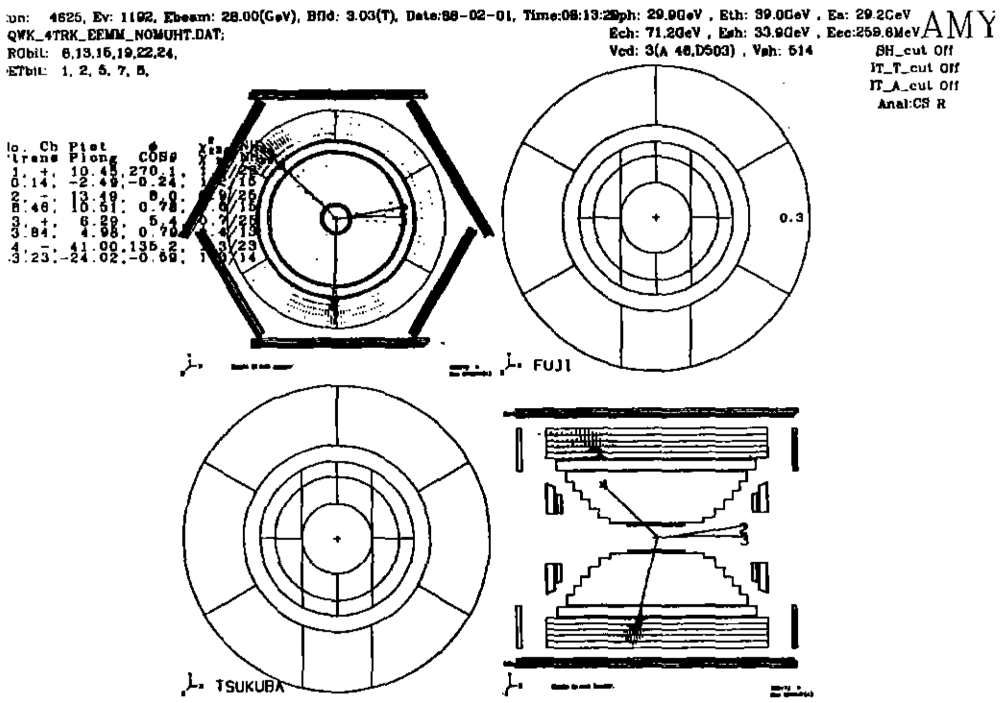

Figure A.12: Possible four-track $e^+e^-\mu^+\mu^-$ event. Energies on the RSC are compatible to those deposited by minimum ionizing particles.

Appendix B

Calibration of the AMY Central Drift Chamber

The calibration of the CDC system consists of two parts. The first part is the calibration of the electronic instruments to obtain an accurate measurement of electron drift time, i.e., the time-of-arrival of the ionization electrons relative to the beam crossing time. This involves adjusting the zero-time channel-by-channel to be coincident with the beam-crossing time and bringing the time scales of each channel into the same time interval units. The second part is the determination of the drift function, i.e. the relation between the measured drift time and the actual position of the track relative to the sense wire. In the following, we discuss these two parts separately.

B.1 CDC electronic calibration system

B.1.1 The Hardware

Signals from each sense wire in the CDC are processed by a chain of electronic circuits as illustrated in Fig. B.1. First in the chain is a current sensing hybrid preamplifier with a gain of 8 mV/μA and a rise time of 5 ns. The preamp produces a differentially driven signal which propagates through 6 m of unshielded twisted-pair woven cable to an amplifier-discriminator circuit located just outside the magnet yoke. Transformer coupling at the amplifier input suppresses common mode noise.

When a sense wire signal exceeds approximately 1 μA, the discriminator fires and sends a differential ECL signal over 25 m of unshielded twisted pair ribbon cable to a time-to-digital conversion system (TDC) located in an "electronics hut" immediately outside the radiation fence. The TDC is a single hit system composed of time-to-amplitude-converter (TAC, Repic DO112) and scan analog-to-digital-converter (ADC, Repic PPF-020) modules in seven FASTBUS crates. The arrival of a CDC signal in the TAC stops the discharge of a capacitor that was initiated by a computer generated START pulse. The voltage remaining in the capacitor is then read and digitized by the scan ADC.

The CDC time information is represented as a number of counts. The relation of number of counts to time is in the form:

$$Time = a_i \times N + b_i$$

where N = number of counts and a_i and b_i are calibration constants for the i^{th} channel. The quantities a_i are related to the discharge rate of the capacitor which is determined by the capacitance and the initial voltage, and is approximately constant over short periods of time. The quantities b_i, on the other hand, are related to the propagation delay of the signal. Because of variations in capacitances, applied voltages, and the electrical path lengths, the a's and b's are different for different channels. The purpose of the calibration is to find the a's and b's for each of the 9048 CDC channels.

Figure B.2 depicts the electronic system used for the determination of the calibration constants a_i and b_i for each channel. During the calibration procedure, the timing electronics, under computer control, sends signals to a pulser (BNC model BL-2) which will then generates a 50 ns wide pulse with a 5 ns risetime. This pulse is fanned out (LeCroy 428F) and sent to a CAMAC analog switch switching unit (Phillips 7145). The switches route the pulses to the axial bands and stereo bands under computer control, thus allowing for their independent calibration. The outputs of the switches are fanned out again and are coupled, via capacitors, to the High Voltage busses, which are constructed as 50 Ω transmission lines for transporting the signals to the different CDC bands.

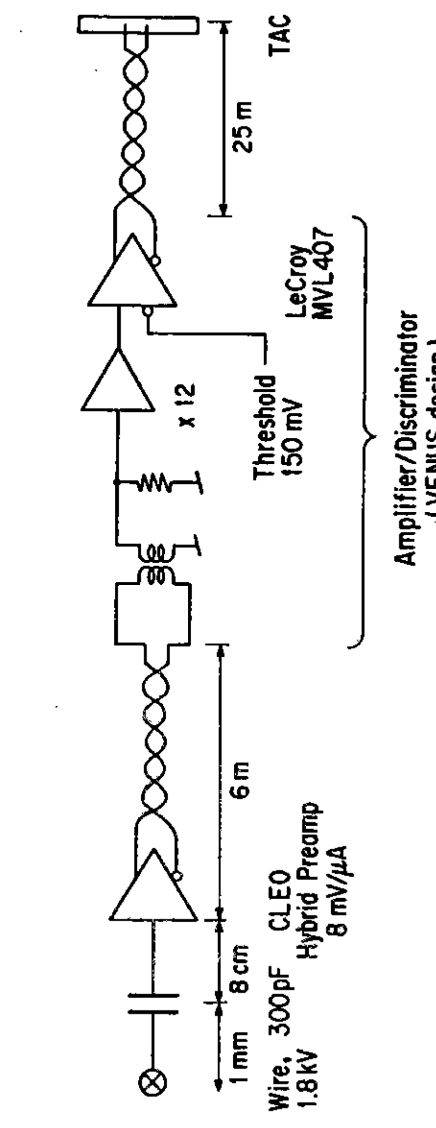

Figure B.1: Overview of CDC Signal Processing Electronics.

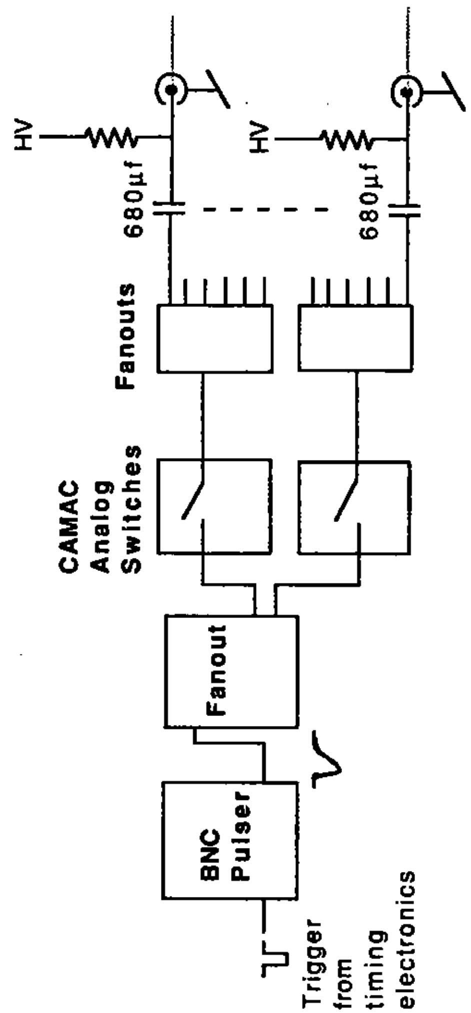

Figure B.2: Overview of CDC Electronics Calibration System.

In each CDC band, the pulses propagate along one of two transmission lines within high voltage distribution boards mounted at the ends of the sense wires of the CDC. Each transmission line is connected to alternating inputs, one line feeding even channels, the other feeding odd channels. This arrangement allows for the independent pulsing of even or odd channels for checking the proper electrical connections as well as testing the status of individual electronics components. (Fig. B.3). In order to prevent noise from getting on to the preamplifier inputs during the normal operation of the CDC, the calibration inputs are disconnected when the calibration system is not operating. This is accomplished by turning off the Calgate buffers circuit on each High Voltage Distribution Boards as shown in Fig. B.4. The buffer circuit, shown in Fig. B.5 has an input impedance of about 10 kΩ and drives 16 preamp inputs through 2 kΩ resistors (the preamp input impedance is 18 Ω). The power for the CAL-GATE buffer is supplied by gate circuitry in the down stream electronics, which, in turn, is controlled by the computer via an electronic switch (Fig. B.2). When the even(odd) CAL-GATE buffer is turned on, it distributes the calibration pulses to the set of even(odd) preamplifier inputs. Except for the traces between the sense wire bushings and the preamplifiers (a printed circuit board trace of length $\sim$ 10 cm), these pulses go through the same electronic path as do the real signals.

In total, the transit time of the calibration pulses consists of three components: i) the delay time of the pulse routing system up to the inputs of the HV busses mounted on the chamber proper; ii) propagation times around the HV busses on the ends of the CDC; and iii) the propagation time from the preamplifier input to the Fastbus TAC. In establishing the pulse routing system, care was taken to ensure that the timing pulses arrived at the different CDC HV busses at the same time (to within 0.1 ns). The propagation times around each HV buss were individually measured to a precision of 0.2 ns with a fast oscilloscope. Thus, by subtracting off the appropriate propagation time from each channel, the TAC/ADC response can be used to measure the relative zero-time of each channel (b_i). From the variation of the TAC/ADC response for different delay times for the calibration pulse, the time scale of channel (a_i) can be determined.

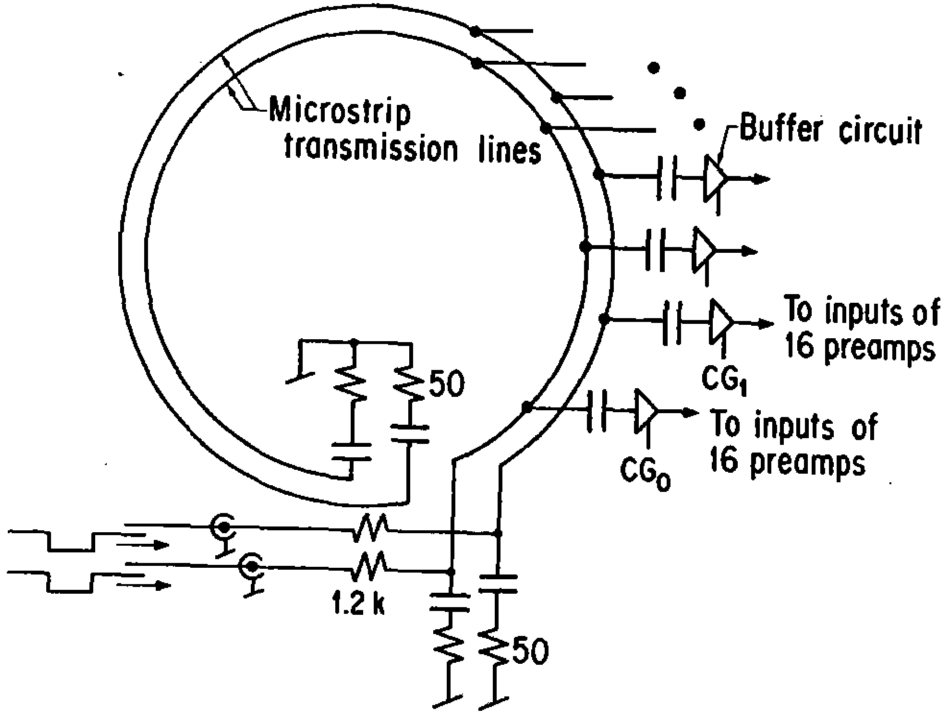

Figure B.3: Distribution system of the calibration pulses.

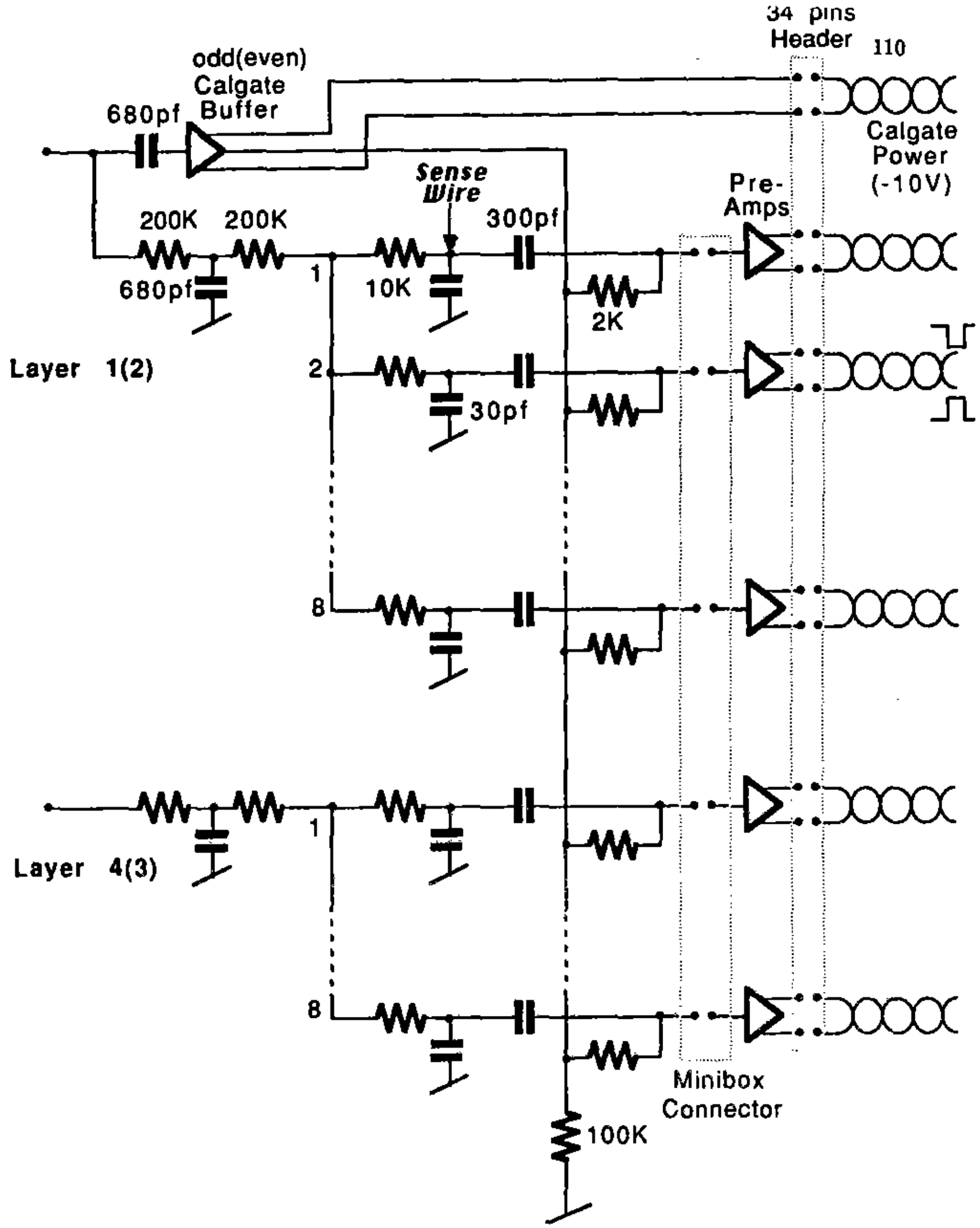

Figure B.4: Electrical circuitry of the CDC High Voltage Distribution Board for the axial layers.

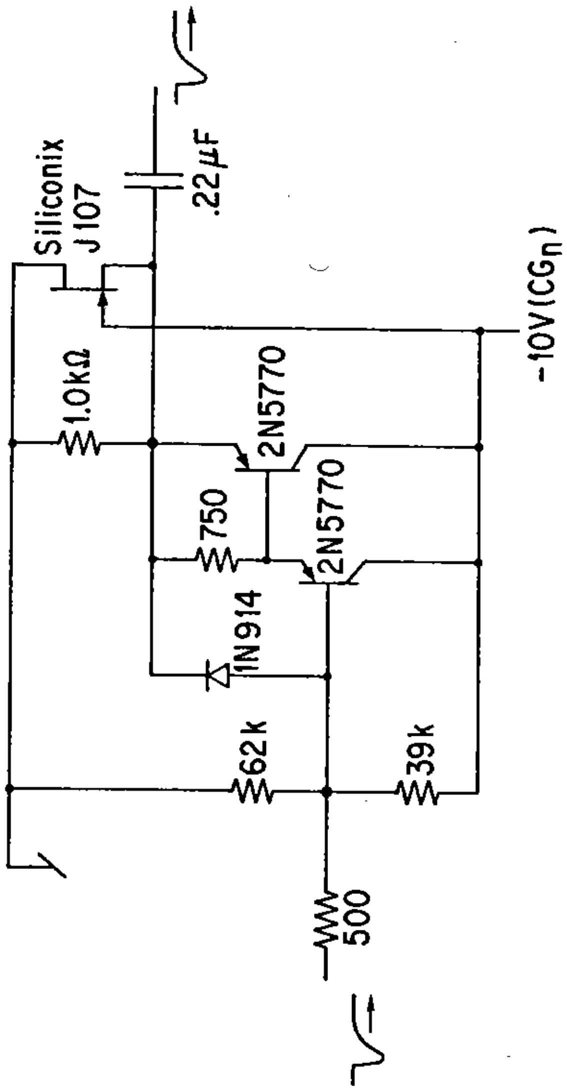

Figure B.5: Circuit diagram of the buffer circuit(Calgate) for calibration pulse.

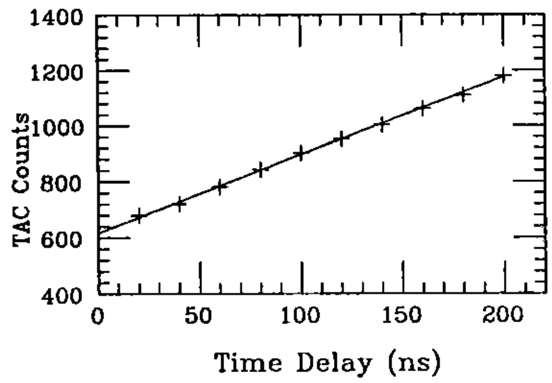

Figure B.6: Linear fitting of the TDC counts against pulsing time delays.

B.1.2 The Software

In practice, each channel is pulsed 20 times at 10 different time delays. A straight line is then fit through the average number of TAC counts at each of the different delays as in Fig. B.6. The slope (A_i) of the fitted line is equal to $1/a_i$. The offset (B) on the y-axis is to related to b by

$$b_i = -\frac{B_i}{A_i} + b_i' \times A_i$$

Here, the b_i' is the constant delay time mentioned in the last section.

Typical values of A_i correspond to 0.36 ns/TDC count. Although these values vary from channel-to-channel, they are quite stable with time ($\sim 0.1\%$ in variation over the period of 3 months). However, the values of B_i fluctuate with time due to variations in temperature and supply voltages. Figure B.7 displays this variation over a period of three months. Since the resolution of the CDC depends on the accuracy of the time measurement, it is crucial to keep track of such variations. An online program that does a brief timing check is used frequently to monitor variations of the A_i and B_i values. If the average values change more than 1.5%, a major calibration is done and the values of a_i and b_i are updated. This procedure keeps the precision of the time measurement at the one nanosecond level.

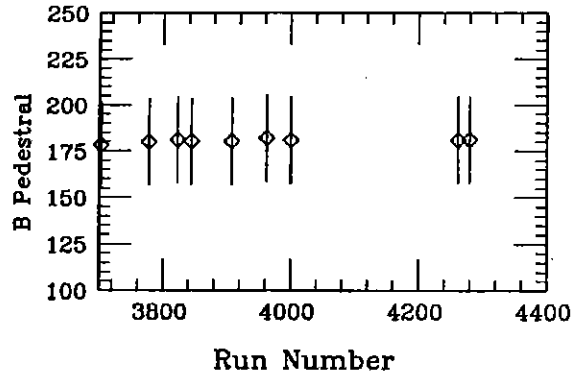

Figure B.7: Variation of B from experimental run 3703-4280 over a period of roughly 3 months.

B.2 Drift time-to-distance relation

B.2.1 Finding the T_0

During actual operation, the data from the CDC corresponds to the total time interval between the TAC "start" signal, derived from the beam crossing signal, and the "stop" caused by the first CDC signal to arrive (after the start pulse). To obtain the electron drift time, we have to subtract the measured time for the particle's time-of-flight, the propagation time along the sense wire in the chamber, and the time between the start gate and the actual beam crossing, commonly referred to as T_0. While the first two factors can readily be taken care of by the position of the hit wire (the z position is estimated by matching the corresponding axial and stereo wires) the T_0 has to be sorted out within the data itself. One can estimate the T_0 from the position in time of the edge of the distribution of drift times, a method that we used for a first-order estimate. We subsequently used an iteration process to improve our knowledge of T_0 and to determine the drift time-to-distance relation, the so called drift function. The accuracy of this method is limited to 1~2 *ns*. A more sensitive method can be applied after a reasonably

precise drift function is determined. Letting

$D_{predict}$ = the distance between the reconstructed track and the hit wire

V_0 = saturated velocity of the gas mixture used by CDC (=44 μm/ns for HRS gas)

ψ = the correct drift function t = measured time, δT_0 = error in T_0,

we then have

$$V_0(t - T_0) - D_{predict} = V_0(t - T_0) - \psi(t - (T_0 + \delta T_0)). \quad \text{(B.16)}$$

At distance close to the sense wire, $\psi \to V_0 t$,

$$V_0(t - T_0) - D_{predict} = V_0 \delta T_0. \quad \text{(B.17)}$$

Therefore, if the predicted distance are closed enough to the true value, a plot of ($V_0 t$ - $D_{predict}$) vs $D_{predict}$ will be very sensitive to small errors of T_0; the correction to T_0 will be equal to the gap between the stationary points and the y=0 line divided by V_0. Such plots (Fig. B.11) are made for the axial and stereo layers to obtain their T_0's, which are found to be -662.5 ns and -664.0 ns respectively. Note that we use the stationary points because this is where the $\psi = V_0$, and $\frac{V_0 \delta T_0}{D_{predict}} \to \infty$ as $D_{predict}$ approaches zero. Since the T_0 used here is the average T_0 of all axial or stereo layers, it is useful only if the CDC electronics are carefully calibrated so that channel-to-channel variations have been eliminated. If the CDC electronics were not constantly monitored and calibrated, we would need 9048 T_0's!

B.2.2 Calibration of CDC in Neon gas

The calibration of the CDC in HRS gas has been described in ref. [40]. Here we will describe the calibration result in Neon-Ethane mixture (Ne 50%, C_2H_8 50%). The CDC in the Neon-Ethane gas is calibrated using roughly 500 wide angle bhabha scattering events accumulated at $\sqrt{s}$ = 60.8 GeV. The drift functions are obtained using the same iteration procedures as used for HRS gas. The corrected measured time vs the predicted distance (i.e. distance between reconstructed tracks and hit wires) scatterplots are fit with the function:

$$x = \begin{cases} V_0 t & t \le t_c \\ V_0 t_c + (F(t) - F(t_c))(1 + a_4(B_o - B) & t > t_c \end{cases} \tag{B.18}$$

$$F(t) = \sqrt{a_1 t + a_2 t^2 + a_3 t^3} \tag{B.19}$$

where

t = corrected measured time, $t_c = 5.0$ ns

$B_o = 3.03$ Tesla

B = the magnetic field around x and is based on the empirical equation obtained from a field calculation.

V_0 = saturated velocity in Neon-Ethane gas = 42 μm/ns.

Because of the strong magnetic field (3 Tesla at the center) used by the AMY detector, the drift path of the electron are sensitive to variation in electric field. This results in a different time-to-distance scatterplot between the left and right hand side of a sense wire (Fig. B.8). When operating in HRS gas, it was found out that in each disk, the left side of outer layer have similar drift path as the inner layer and vice versa. We therefore assume the same effect in Neon gas and allow for four different sets of a_i's for the 6 axial disks:

- right side of layer 1 and left side of layer 4(5 for disk 1) : XIROL
- right side of layer 2 and left side of layer 3 : XMIROL
- left side of layer 1 and right side of layer 4(5 for disk 1) : XILOR
- left side of layer 2 and right side of layer 3 : XMILOR

(note : layer 3 of disk 1 used the average of XMIROL and XILOR);

and three sets for the 5 stereo disks:

- right side of layer 1 and left side of layer 3 : SIROL
- left side of layer 1 and right side of layer 3 : SILOR
- layer 2 : SMID

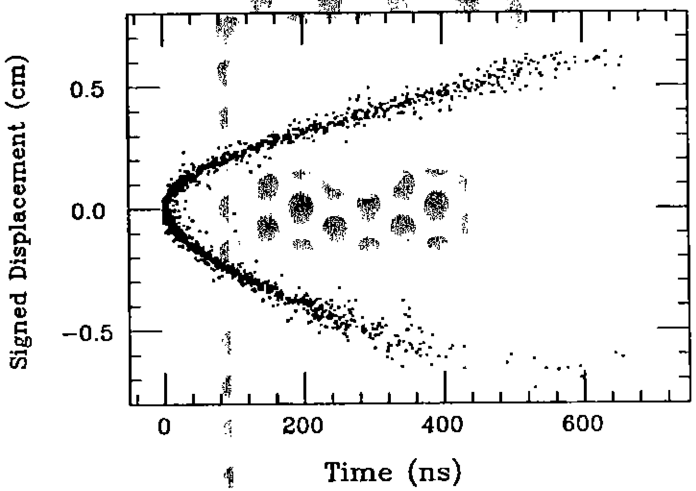

Figure B.8: Scatterplot of the measured time vs signed $D_{predict}$. The difference between the +/−(left/right)side is due to different path length.

where the layers are numbered in the order of increasing radii. (Fig. 2.6).

The overall resolution for the axial layers is about 230 μm and 250 μm for the stereo layers (Fig. B.9). And the resolution varies with measured time and predicted distance in a spoon-like fashion (Fig. B.10) as seen in the HRS gas.

The T_0 values, obtained using the method described above, were found to be -666.7 ns for the axial layers and -666.0 ns for the stereo layers. These should be compared with the corresponding T_0 of -662.5 ns and -664.0 ns in HRS gas from the 52 GeV Bhabha event sample. Since the value of T_0 depends only on the timing of beam crossing and the AB pedestals of CDC electronics, one or the other must have changed. Fig. B.11 shows that the stationary points of the curve is $\sim$ 50 μm different between the +/−(left/right) sides of $D_{predict}$, indicating either an inaccuracy of the drift function or a bias in the track reconstruction. The effect is more pronounced for the inner axial layers ($\approx$ 80 μm). Such a disagreement is not seen for the stereo layers within the available statistical precision. In HRS gas, such effects were zero within the statistical uncertainty of 10 μm.

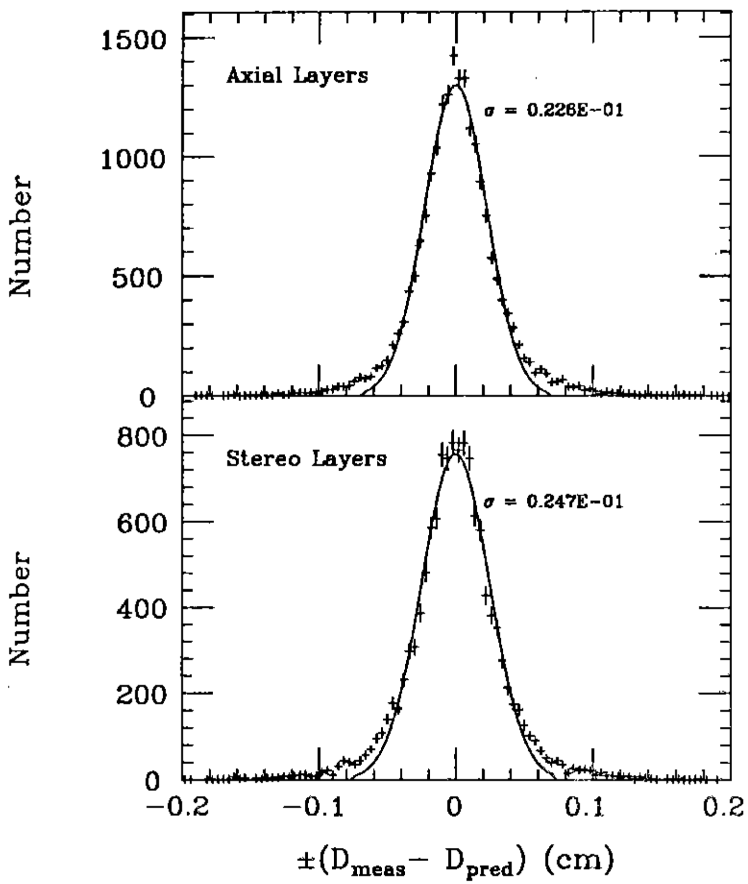

Figure B.9: The CDC spatial resolution in Neon-Ethane gas based on Bhabha events

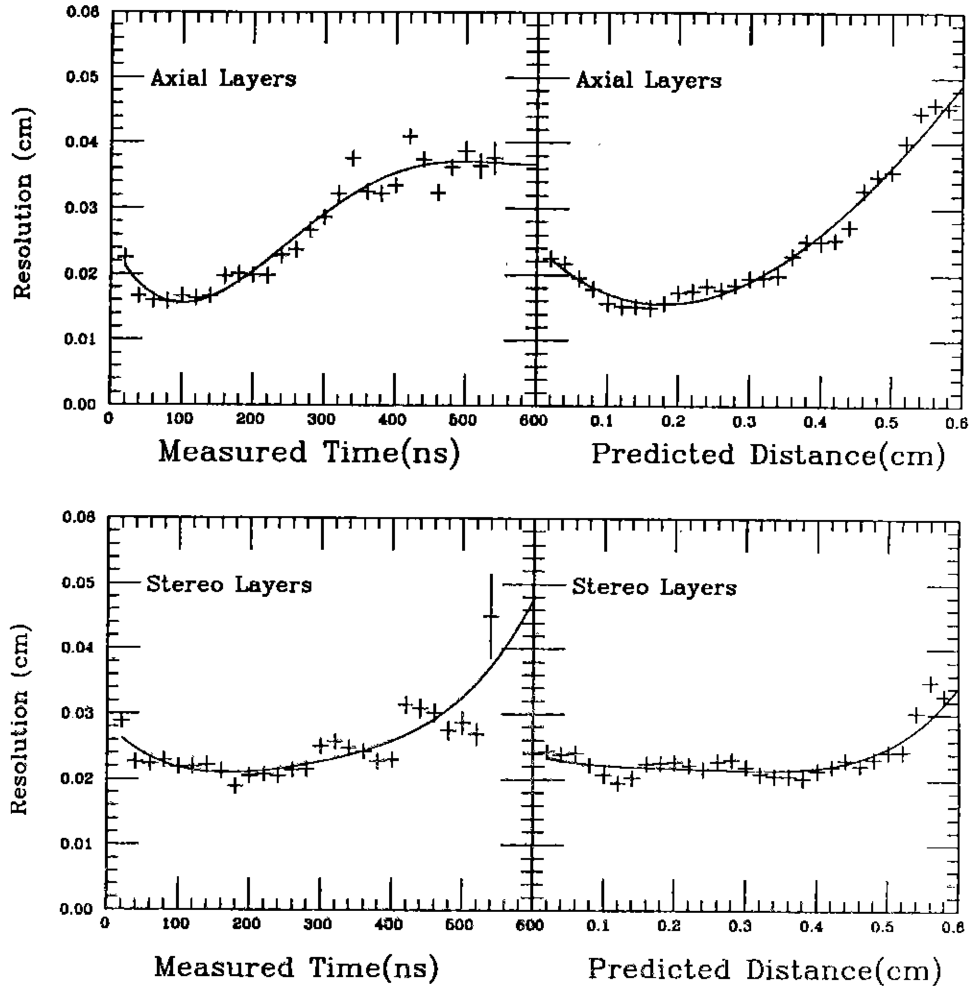

Figure B.10: The variation of spatial resolution with time and distance

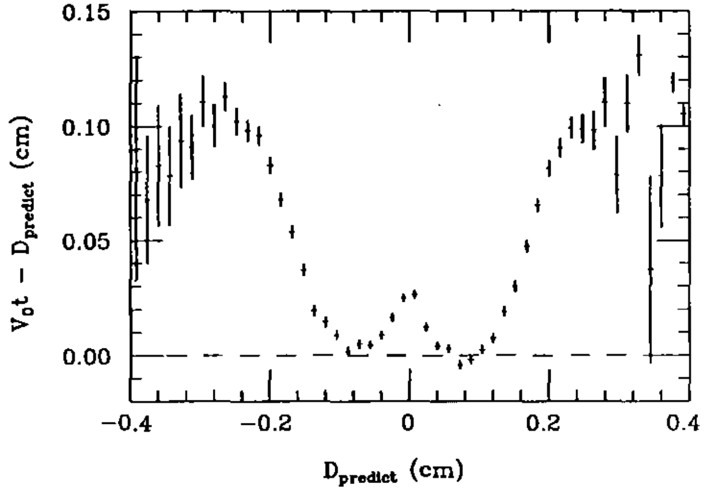

Figure B.11: $(V_0t - D_{predict})$ vs $D_{predict}$ plot for the Neon-Ethane gas

There is still considerable spread in the time-distance scatter plots for longer drift times, even after being separated according to the above schemes for drift function fitting. Fig. B.12 illustrates this for the layers 1 and 4 of the axial disks. Separate scatter plots for the different layers show that the left side of layer 1 and right side of layer 4 do not overlap as well as in the HRS gas. This indicates that the path length of slower drifting electrons are more sensitive to variation of magnetic field, probably due to multiple scattering and diffusion. Therefore, we may need separated a_i's for the left side and right side of individual layers in each disk (at least for layer 1 and 4), or better still, different functions for each of the 40 CDC layers.

B.2.3 Further Improvement

One can further improve the spatial resolution of CDC by making corrections to the drift function using the following method. Here we use the same variables as before and define

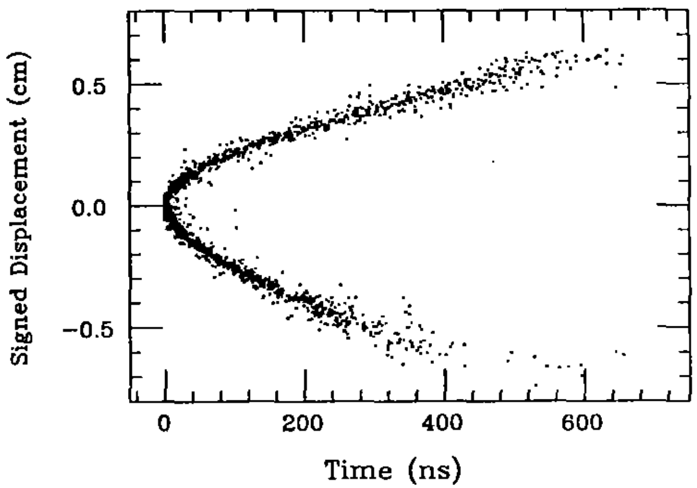

Figure B.8: Scatterplot of the measured time vs signed $D_{predict}$. The difference between the +/−(left/right)side is due to different path length.

where the layers are numbered in the order of increasing radii. (Fig. 2.6).

The overall resolution for the axial layers is about 230 μm and 250 μm for the stereo layers (Fig. B.9). And the resolution varies with measured time and predicted distance in a spoon-like fashion (Fig. B.10) as seen in the HRS gas.

The T_0 values, obtained using the method described above, were found to be -666.7 ns for the axial layers and -666.0 ns for the stereo layers. These should be compared with the corresponding T_0 of -662.5 ns and -664.0 ns in HRS gas from the 52 GeV Bhabha event sample. Since the value of T_0 depends only on the timing of beam crossing and the AB pedestals of CDC electronics, one or the other must have changed. Fig. B.11 shows that the stationary points of the curve is $\sim$ 50 μm different between the +/−(left/right) sides of $D_{predict}$, indicating either an inaccuracy of the drift function or a bias in the track reconstruction. The effect is more pronounced for the inner axial layers ($\sim$ 80 μm). Such a disagreement is not seen for the stereo layers within the available statistical precision. In HRS gas, such effects were zero within the statistical uncertainty of 10 μm.

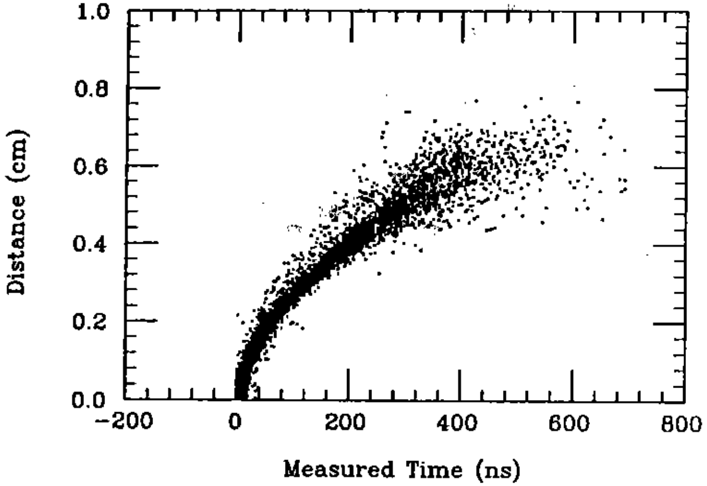

Figure B.12: Drift time vs drift distance for the Neon-Ethane gas

ψ' = drift function obtained by calibration

$\delta\psi'$ = error in drift function

δt = measured drift time after correction

$D_{measure}$ = the distance calculated by the drift function $= \psi'\delta t$

$D_{predict} = \psi\delta t = (\psi' - \delta\psi')\delta t$.

In the first order approximation,

$$\begin{aligned} D_{measure} - D_{predict} &= \psi'\delta t - (\psi' - \delta\psi')\delta t \\ &= \delta\psi'\delta t \\ &= f(\delta t) \qquad \text{(B.20)} \end{aligned}$$

Therefore, by fitting an appropriate function to the $(D_{measure} - D_{predict})$ vs δt plot(Fig. B.13), one can use the fitted result to make corrections to the drift functions. Applying such corrections to the Neon gas drift functions, the spatial resolution for the axial layers is improved to 215 μm, and is improved to 242 μm for the stereo layers. However, since it is obvious that the layer-to-layer variations are still a dominant component of the CDC spatial resolution, improvements using

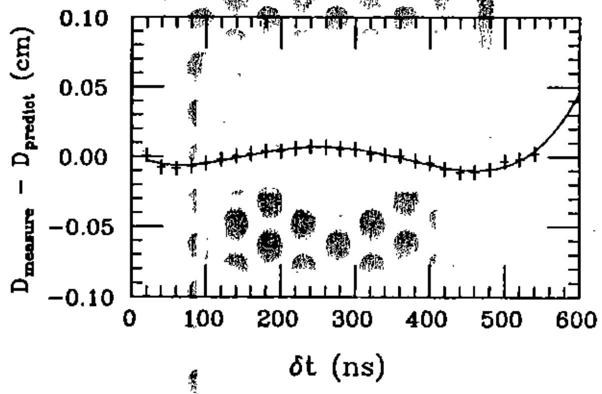

Figure B.13: $(D_{measure} - D_{predict})$ vs δt plot for the Neon-Ethane gas

techniques that do not allow for layer-to-layer variations of the parameters will only be marginal.

Appendix C

List of the AMY Collaborators

The AMY Collaboration

Y.H. Ho,[a] Y. Kurihara,[b] T. Omori,[b] P. Auchincloss,[a] D. Blanis,[a] A. Bodek,[a] H. Budd,[a] M. Dickson,[a] S. Eno,[a] C.A. Fry,[a,b] H. Harada,[a] B.J. Kim,[a] Y.K. Kim,[a] T. Kumita,[a] T. Mori,[a] S.L. Olsen,[a,i] N.M. Shaw,[a] A. Sill,[a] E.H. Thorndike,[a] K. Ueno,[a] C. Velissaris,[a] G. Watts,[a] H.W. Zheng,[a] K. Abe,[b] Y. Fujii,[b] Y. Higashi,[b] S.K. Kim,[b] A. Maki,[b] T. Nozaki,[b] H. Sagawa,[b] Y. Sakai,[b] Y. Sugimoto,[b] Y. Takaiwa,[b] S. Terada,[b] R. Walker,[b,a] R. Imlay,[c] P. Kirk,[c] J. Lim,[c] R.R. McNeil,[c] W. Metcalf,[c] S.S. Myung,[c] C.P. Cheng,[d] P. Gu,[d] J. Li,[d] Y.K. Li,[d,f] M.H. Ye,[d] Y.C. Zhu,[d] A. Abashian,[e] K. Gotow,[e] K.P. Hu,[e] E.H. Low,[e] M.E. Mattson,[e] L. Piilonen,[e] K.L. Sterner,[e] S. Lusin,[f] C. Rosenfeld,[f] A.T.M. Wang,[f] S. Wilson,[f] M. Frautschi,[g] H. Kagan,[g] R. Kass,[g] C.G. Trahern,[g] R.E. Breedon,[h,b] G.N. Kim,[h,b] Winston Ko,[h] R.L. Lander,[h] K. Maeshima,[h] R.L. Malchow,[h] J.R. Smith,[h] D. Stuart,[h] F. Kajino,[j] D. Perticone,[k] R. Poling,[k] T. Thomas,[k] Y. Ishi,[l] K. Miyano,[l] H. Miyata,[l] T. Sasaki,[l] Y. Yamashita,[m] A. Bacala,[n,o] J. Liu,[n] I.H. Park,[n] F. Sannes,[n] S. Schnetzer,[n] R. Stone,[n] J. Vinson,[n] H. Ichinose,[p] S. Kobayashi,[p] A. Murakami,[p] J.S. Kang,[q] H.J. Kim,[q] M.H. Lee,[q] D.H. Han,[r] E.J. Kim,[r] D. Son,[r] T. Kojima,[s] S. Matsumoto,[s] R. Tanaka,[s] Y. Yamagishi,[s] T. Yasuda,[s] T. Ishizuka,[u] and K. Ohta[u]

[a] *University of Rochester, Rochester, NY 14627*

[b] *KEK, National Laboratory for High Energy Physics, Ibaraki 305*

[c] *Louisiana State University, Baton Rouge, LA 70803*

[d] *Institute of High Energy Physics, Beijing 100039*

[e] *Virginia Polytechnic Institute and State University, Blacksburg, VA 24061*

[f] *University of South Carolina, Columbia, SC 29208*

[g] *Ohio State University, Columbus, OH 43210*

[h] *University of California, Davis, CA 95616*

[i] *Tsukuba University, Ibaraki 305,* [j] *Konan University, Kobe 658*

[k] *University of Minnesota, Minneapolis, MN 55455*

[l] *Niigata University, Niigata 950-21,* [m] *Nihon Dental College, Niigata 951*

[n] *Rutgers University, Piscataway, NJ 08854*

[o] *University of the Philippines, Quezon City, 3004*

[p] *Saga University, Saga 840,* [q] *Korea University, Seoul 136-701*

[r] *Kyungpook National University, Taegu 702-701*

[s] *Chuo University, Tokyo 112,* [u] *Saitama University, Urawa 338*

Bibliography

[1] P.A.M. Dirac, *Roy.Soc.Proc., A,* **Vol 114**, 243 (1927).

[2] S.L. Wu, *Phys. Report* **107**, 59 (1984).

[3] S.K. Kim, *Ph.D. thesis*, Korea University, (1988).

[4] Cello Collaboration, *DESY Report* 84-104 (1984);
Pluto Collaboration, *Z. Phys. C* **27**, 249 (1985);
Jade Collaboration, *Z. Phys. C* **30**, 545 (1986);
Cello Collaboration, *DESY Report* 88-086, **LAL 88-27** (1988);
Mark-J Collaboration, *Phys. Rev. D* **Vol 38, No.9**, 2665 (1988);
Cello Collaboration, *DESY Report* 88-192, (1988);
Cello Collaboration, *Z. Phys. C* **43**, 1-14, (1989).

[5] V.M. Budnev et al., *Physics Reports* **15**, 181-282, (1975);

[6] Ch. Berger and W. Wagner, *Physics Reports* **146**, 1-134, (1987);

[7] F. Low, *Phys. Rev* **120**, 582 (1960);

[8] C.N. Yang, *Phys. Rev* **77**, 242 (1950);

[9] F.A. Berends, P.H. Daverveldt and R. Kleiss, *Phys. Lett.* **Vol 148B No.6**, 489 (1984);

[10] TRISTAN Project Group, "*TRISTAN Electron-Positron Colliding Beam Project*", *KEK Report* 86-14, March 1987.

[11] AMY Collaboration, *Proposal* TRISTAN-EXP-003, November, 1984.

[12] T. Mori, *Ph.D. thesis*, Univ. of Rochester, Appendix A (1988).

[13] F. Kajino, A. Abashian, and K. Gotow, Nucl. Instrum. Methods **A245**, 507 (1986).

[14] S.S. Myung, *Ph.D. thesis*, Korea Univeristy, (1988).

[15] Y. Doi et al., KEK Preprint 88-22 (submitted to *Nucl. Instrum. Methods*).

[16] M. Gyr and C. Iselin, *POISSON*, CERN (1976).

[17] H. Asakura et al., *Reports of the Faculty of Science and Engineering, Saga Univ.* Vol.16, No.2 (1988)

[18] T. Mori, *Ph.D. thesis*, Univ. of Rochester, Appendix B (1988).

[19] D.G. Cassel and M. Ogg, *"DUET - a Track-Finding Program for Cylindrical Geometries"*, CLEO Internal Report, December 12, 1983.

[20] A. Bacala et al., *Phys. Lett.* **B218**, 112 (1989).

[21] T. Mori et al., *Phys. Lett.* **B218**, 499 (1989).

[22] O.I. Dahl et al., *SQUAW*, LBL Group A note P-126 (1968).

[23] T. Sjostrand et al., *Com. Phys. Comm.* **43**, 367 (1987).

[24] J.A.M. Vermaseren, *Proc. Intl. Workshop on Gamma Gamma Collision* , 35-46 (1980).

[25] G.P. Lepage, *J. Comp. Phys.* **27**, 192 (1978)

[26] J.A.M. Vermaseren, *Nucl. Phys.* **B229**, 347-371 (1983).

[27] F.A. Berends, P.H. Daverveldt and R. Kleiss, *Nucl. Phys.* **B253**, 441-463 (1985).

[28] M.Kuroda, Meji Gakuin Univ. *(Tokyo) Research Journal* **424**, 27 (1988); M. Kuroda, Meji Gakuin Univ. preprint MGU-DP 7 (1988), unpublished.

[29] S.Kawabata, *Computer Phys. Comm.* **41**, 127-153 (1986).

[30] F.A. Berends, P.H. Daverveldt and R. Kleiss, *Comp. Phys. Comm.* 40, 285-307 (1986).

[31] F.A. Berends, P.H. Daverveldt and R. Kleiss, *Comp. Phys. Comm.* 40, 309-326 (1986).

[32] R. Bhattacharya, J. Smith, and G. Grammer, *Phys. Rev.* **D15**, 3267 (1977).

[33] Y. Kurihara et al., AMY collaboration, *XIV Int. Sym. on Lepton and Photon Interactions*, (1989)

[34] S.L. Glashow, *Nucl. Phys.* **22**, 579 (1961); S. Weinberg, *Phys. Rev. Lett.* **19**, 1264 (1967).

[35] S.K.Kim et al., *Phys. Lett.* **B223**, 476, (1989).

[36] G.J. Gounaries and J.J. Sakurai, *Phys. Rev. Lett.* **41**, 244-247 (1968).

[37] H.-J. Behrend et al., *Z. Phys. C* **43**, 1-14, (1989).

[38] A. Petradza, *Ph.D. thesis*, Univ. of Michigan, (1989).

[39] W. Bartel et al., *Z. Phys. C* bf 30, 545-549, (1986).

[40] T. Mori, *Ph.D. thesis*, Univ. of Rochester, Appendix A (1988).

[41] S. Behrends, *Ph.D. thesis*, Univ. of Rochester, Appendix 1 (1987).